

**A Search for Free Proton Decay,
and Nucleon Decay in O^{16} ,
Using the Invariant Mass and Momentum
of Exclusive Final States**

Thesis by
Geoffrey Blewitt

In Partial Fulfillment of the Requirements
for the Degree of
Doctor of Philosophy

California Institute of Technology
Pasadena, California

1986

(Submitted October 21, 1985)

©1985
Geoffrey Blewitt
All Rights Reserved

Acknowledgements

In a way, this work represents 25 years of the love, encouragement, and intellectual nourishment of those around me, and for that reason, I am indebted to the many people in my life.

My thesis advisor and friend, John LoSecco, has the most acute sense of the need to move in uncharted directions, to find even more stones to turn over. His trusting attitude, of allowing me to dabble with various ideas, has given me a creative, intellectual freedom, which, in the context of innovation, provides the necessary compliment to the discipline of textbook knowledge. I thank him for that, and for the stones I have turned over myself.

My experience with the I.M.B. Collaboration provided valuable inspiration and competition, which has helped to develop my sense of “careful urgency.” The balance between teamwork and individual effort was struck well. The collaboration meeting struggles and tussles between the free-thinking intelligensia was testing, difficult, and most of all, fun. I thank all the members (Appendix A) for their support. In particular, I am grateful to Egbert Lehmann and Bruce Cortez for allowing me to share their offices here at Caltech, and for stimulating those gray cells over the last few years.

My wife, Debra, and our son Russell, have been invaluable companions to me in these last three years. Their unrelenting support, love, and encouragement has made an important contribution to this work. The biggest motivation of all came from the hopes we share for the future.

My warmest gratitude goes to my mother and father, Greta and Dennis Blewitt, who have always “been there.” Their continuing devotion and love is more than I could ever ask for. I thank them especially for allowing me to entertain my curiosity in all walks of life, including physics. I dedicate this thesis to you.

This work was supported in part by the U.S. Department of Energy.

Abstract

Existing Grand Unified Theories predict a free proton lifetime which would be experimentally accessible. If discovered, a study of the branching modes of the proton could provide indicators to the correct theory. The lifetime of a proton is probably longer in a nucleus, though by no more than an order of magnitude.

A search for nucleon decay was performed for 37 possible branching modes of nucleons in water, and 14 branching modes of free protons from the hydrogen in water. The data was taken from the I.M.B. water Cherenkov detector, which contains 3,300 metric tons in the fiducial volume. The only significant background to proton decay comes from atmospheric neutrino interactions. An initial search used the visible energy, anisotropy, and number of muon decays of events. A more sophisticated search automatically selected events with two clear tracks of opening angle $> 115^\circ$. The invariant mass and momentum of these events were calculated for 16 nucleon decay hypotheses.

In 417 livedays, 326 events were reconstructed in the fiducial volume at a rate, and with visible characteristics consistent with atmospheric neutrino interactions. No significant excess of events was found for any nucleon decay mode. For the visible energy and anisotropy analysis, partial lifetime limits at the 90% confidence level were set in the range 10^{31-32} years for nucleons, assuming that the free and bound lifetimes are similar. With the free proton decay analysis, limits were set in the range 10^{30-32} years. The number of clean two-prong events was found to be $4.0 \pm 1.1\%$. The background estimates gave a mean estimate of $4.1 \pm 0.3\%$. Partial lifetime limits at the 90% confidence level were set for both free protons, and bound plus free nucleons at 10^{32} years for $N \rightarrow \text{lepton} + \gamma/\pi$, and 10^{31} years for $N \rightarrow \text{lepton} + \eta/\rho/\omega$.

A framework for converting the results into model-dependent total lifetime limits is described, and limits for SU(5) are explicitly calculated. Our results imply an SU(5) model-dependent limit of 4×10^{31} years (90% C.L.) on the to-

tal proton lifetime, where effects of the nucleus on the decay rate have been accounted for. This is incompatible with theoretical predictions. The derived limits should also provide useful constraints on other Grand Unified Theories.

Contents

Acknowledgments	iii
Abstract	iv
List of Figures	x
List of Tables	xii
1. INTRODUCTION	1
(1.1) <i>Motivating the Search</i>	1
(1.2) <i>Theoretical Progress</i>	2
The Road to Unification	
Grand Unification and Proton Decay	
2. THEORETICAL CONSIDERATIONS	7
(2.1) <i>Distinguishing Models</i>	7
Lifetimes	
ΔL	
ΔS	
ΔI	
Lepton Type	
Polarization	
Lepton Momentum	
(2.2) <i>Direct Nuclear Effects</i>	9
The Two-Quark Overlap Amplitude	
Time Dilation, Available Energy, and Phase-Space	
Final State Interference	
Virtual Meson Absorption	
Three-Quark Fusion	
Conclusions	
3. EXPERIMENTAL CONSIDERATIONS	21
(3.1) <i>The First Principles of Design</i>	21
Sensitivity	
Exposure	
Mass	
Density and Size	
Decay Source	

Depth	
(3.2) <i>Using Cherenkov Radiation for Detection</i>	27
Introduction	
The Concept of Radiating Track Length, r	
The Concept of Visible Energy, E_c	
Absolute Energy Calibration	
Visible Track Structure	
Detector Pixels	
(3.3) <i>Cosmic Rays and Background Sources</i>	37
Introduction	
Atmospheric Interactions	
Direct Detection of Muons	
Indirect Detection of Muons	
Detection of Neutrinos	
4. THE DETECTOR	46
(4.1) <i>Perspective</i>	46
(4.2) <i>Overview of the Detector Systems</i>	46
The Water System	
The Data Acquisition System	
The On-Line Data Processing System	
The Calibration System	
(4.3) <i>Calibrations</i>	54
The Goals	
Positions, \vec{x}_i	
Orientations, $\hat{\theta}_i$	
The $T1$ Scale	
The $T2$ Scale	
The Q Scale	
Visible Energy	
5. THE DATA REDUCTION	61
(5.1) <i>Philosophy</i>	61
(5.2) <i>Obtaining the Data Sample</i>	61
History	
The "Official" Data Sample	
The Thesis Data Sample	
(5.3) <i>Checks for Contamination</i>	65
Introduction	

The Vertex Distribution	
The Energy Direction Distribution	
(5.4) <i>Conclusions</i>	68
6. SIMULATIONS	69
(6.1) <i>Introduction</i>	69
(6.2) <i>General Monte-Carlo Features</i>	70
Propagation and Interaction in Water	
Cherenkov Light and Propagation	
The Detector	
(6.3) <i>Signal Simulation</i>	74
Overview of Monte-Carlo Files	
Decay Parameters	
Rho Resonance Mass Distribution	
Propagation and Interaction in the Nucleus	
Simulated Data Reduction	
(6.4) <i>Background Simulation</i>	88
Overview of Monte-Carlo Files	
Neutrino Flux Estimates	
Neutrino Cross-Sections	
Bubble Chamber Data	
Neutrino Event Rates	
7. THE SEARCH FOR A SIGNAL	95
(7.1) <i>Nucleon Decay Exclusive Final States</i>	95
General Physical Characteristics	
General Visible Characteristics	
(7.2) <i>Visible Energy, Anisotropy Analysis</i>	99
Visible Energy	
Anisotropy	
Muon Decays	
Background/Data Comparison	
Expected Signal/Background Comparison	
Results	
Conclusions	
(7.3) <i>Two-Prong Analysis</i>	114
Decays with Two-Prongs	
Selection of Two-Prongs	
Background/Data Comparison	

(7.4) <i>Invariant Mass, Momentum Analysis</i>	117
Momentum Reconstruction	
Invariant Mass Reconstruction	
Expected Signal/Background Comparison	
Background/Data Comparison	
Background Subtraction	
Results	
Conclusions	
8. THE IMPLICATIONS	143
(8.1) <i>Summary of Results</i>	143
(8.2) <i>Theoretical Implications</i>	144
The SU(5) Theory	
Other Theories	
(8.3) <i>Experimental Implications</i>	146
APPENDIX A: The IMB Collaboration	148
APPENDIX B: Derivation of $\pi^0 \rightarrow \gamma\gamma$ Theorems	150
APPENDIX C: Summary of IMB Theses	152
References	155

List of Figures

2-1	Suppression of the proton decay rate in O^{16}	12
2-2	Proton momentum distribution in O^{16}	12
2-3	Effective mass distribution for protons in O^{16}	14
2-4	Final state interference in $NN \rightarrow Ne\pi$	14
2-5	Virtual pion absorption in $NN \rightarrow Ne$	17
2-6	Three-quark fusion in the nucleus	17
3-1	Radiating track length vs. energy for particles in H_2O	29
3-2	Visible energy vs. visible particle range	31
3-3	dE_c/dx vs. visible particle range	31
3-4	Cherenkov angle vs. distance along visible track	33
3-5	Intensity normal to light vs. distance along track	33
3-6	(Intensity) \times (distance) vs. Cherenkov angle (π^\pm)	35
3-7	(Intensity) \times (distance) vs. Cherenkov angle (p^+)	35
3-8	Flux of cosmic ray muons	39
3-9	Distribution of interactions from entering neutrons	43
4-1	Schematic view of the I.M.B. detector	47
4-2	Measured attenuation in water vs. wavelength	49
4-3	Typical timing distribution of a P.M.T.	51
4-4	Photocathode quantum efficiency vs. wavelength	52
5-1	Vertex distribution of 326 events	64
5-2	Direction cosine distribution of 326 events	66
5-3	Z-direction cosine vs. vertex position for 326 events	67
6-1	Cross-sections for πO^{16}	71
6-2	Density distribution of nucleons in O^{16}	77
6-3	Phase-space considerations for ρ decay	79
6-4	The shape of the ρ resonance in proton decay	81
6-5	Mean cross-sections per nucleon for πN in O^{16}	83
6-6	The fate of π 's in the O^{16} nucleus	85

6-7	The fate of η 's in the O^{16} nucleus	86
6-8	Various flux estimates of neutrinos	89
6-9	Inclusive cross-section coefficients for νN and $\bar{\nu}N$	91
7-1	Event distributions in anisotropy.....	102
7-2	Event distributions in visible energy	103
7-3	Multi-prong event distributions in visible energy	104
7-4	Event distributions in the $E_c-A_c-n_\mu$ plane	105
7-5	Simulated event distributions in the $E_c-A_c-n_\mu$ plane.....	109
7-6	Fraction of two-prong events for data and background.....	118
7-7	Event distributions in the $M-P$ plane (M.C. signal)	124
7-8	Event distributions in the $M-P$ plane (M.C. background)	126
7-9	Event distributions in the $M-P$ plane (data)	128

List of Tables

6-10	Reconstruction efficiency for nucleon decay modes.....	87
7-1	Fraction of all events containing μ decays	107
7-2	Fraction of low-energy events containing μ decays	107
7-3	Fraction of multi-prong events containing μ decays	107
7-4	Partial lifetime limits for 37 decay modes	111
7-5	Candidate events for nucleon decay	113
7-6	Particle hypotheses for two-body nucleon decays	122
7-7	Invariant mass, momentum requirements	131
7-8	Detection efficiencies.....	133
7-9	Two-prong candidates	134
7-10	Background estimates for total number of candidates.....	135
7-11	Background estimates for decay modes.....	136
7-12	Measured Signal for two-prong nucleon decay	139
7-13	Partial Lifetime limits for two-prong nucleon decay.....	141
8-1	Branching ratios for nucleon decay in SU(5).....	144

1. Introduction

1.1 MOTIVATING THE SEARCH

“Of course, it has been recognised for a long time that the final justification of symmetry principles, as of all other physical laws, is the experimental evidence for them”

—G. Feinberg and M. Goldhaber¹ (1959)

There is an interesting irony concerning the history of proton decay. Feinberg and Goldhaber¹ were making the correct observation that conservation laws, such as baryon conservation, should never simply be assumed “because they are implicitly used in many experiments without leading to difficulties,” but that they must be “explicitly tested to a considerable degree.”

It was empirical observation which led to Wigner’s hypothesis,^{2,3} in 1949, of a “conservation law for heavy particles.” This was later supported by the observations of Reines, Cowan, and Goldhaber⁴ in 1954, whose results indicated a nucleon lifetime limit in excess of 10^{22} yr.

In the 1950’s, the search for proton decay became interesting due to unanswered questions concerning the symmetry responsible for baryon conservation. As Lee and Yang⁵ pointed out in 1955, conservation laws correspond to symmetries in nature, and symmetries come in two classes: those concerning space-time transformations (e.g., conservation of energy, momentum, and angular momentum), and those concerning gauge transformations (e.g., conservation of electric charge). Presumably, conservation of baryon number would arise from a local gauge symmetry in much the same way as for conservation of charge. That would imply the existence of a force between baryons, which, by analogy with the photon of the electric field, would have to be mediated by a neutral, massless, vector boson (which has never been observed). Lee and Yang reasoned, on empirical

grounds, that such a force, if it existed, would have to be much weaker than gravity.

In the 1970's, however, the search for proton decay became motivated by predictions of theories concerning the symmetry responsible for all the known forces in nature, apart from gravity. Such "Grand Unified Theories" had within their frameworks, very natural mechanisms which could lead to baryon *non*-conservation. These predictions caused the recent interest in the search for proton decay, culminating in the building, operating and analysis of the large, dedicated proton decay detectors of the 1980's.

Thus the irony: the initial motivation for acquiring experimental evidence was to shed light on a possible symmetry responsible for proton *stability*—all in the spirit put forth by Feinberg and Goldhaber¹. The present motivation is to shed light on a possible symmetry responsible for unifying the strong, weak, and electromagnetic forces, and ultimately responsible for proton *decay*. The spirit, of course, is still the same; the testing, as this thesis claims, has been "explicit," and "to a considerable degree."

1.2 THEORETICAL PROGRESS

The Road to Unification

Proton decay was one of the many predictions which surfaced from recent attempts to unify the known forces.

A unification of the electromagnetic and weak forces was achieved independently by Weinberg⁶ (1967) and Salam⁷ (1968). They improved Glashow's⁸ (1961) model, which was based on the $SU(2) \otimes U(1)$ gauge group, by introducing spontaneous symmetry breaking through the Higg's mechanism. Hence, the masses of the three hypothetical gauge bosons were explained (and predicted, given the experimental value of $\sin^2 \theta_W$, a parameter not fixed by the theory).

The Weinberg-Salam model was outstandingly successful. Not only did it

encompass QED and the presently known weak interaction phenomenology— its predictions of the existence of weak neutral currents were experimentally found⁹ (1973), and the new vector bosons were recently discovered at the predicted masses¹⁰ (1983).

Despite its successes, the Weinberg-Salam model was incomplete. Apart from the obvious fact that strong interactions were not included, the model was not truly unified, in the sense that it did not have a unique coupling constant set by the theory. It did, however, predict that the U(1) and SU(2) coupling constants, g_1 and g_2 , were related by a free parameter θ_W (the “mixing angle”): $\tan \theta_W = g_1/g_2$.

Strong interactions, on the other hand, seemed adequately described by QCD, which was based on the SU(3) gauge group (often written $SU_c(3)$ to denote “color”). Originally introduced by Han and Nambu¹¹ in 1965, QCD was difficult to use in calculations, and difficult to test experimentally. However, the concept of color came to provide elegant explanations of quark confinement,¹² asymptotic freedom,¹³ and the hadron-muon ratio of e^+e^- annihilations.¹⁴

Thus, by the early 1970’s, most phenomenology could be explained in terms of the “standard model” of the gauge symmetry $G_S \equiv SU_c(3) \otimes SU(2) \otimes U(1)$, which was simply QCD and Weinberg-Salam combined. In this picture, leptons and quarks were in separate multiplets¹⁵—thus the number of leptons and quarks in a system were separately conserved, and no mechanism existed for proton decay. Both the successful predictions of Weinberg-Salam, and the failures of the standard model to explain the relations between the three coupling constants, the lepton and quark charges, the lepton and quark masses, etc., provided the inspiration to proceed toward “Grand Unified Theories” (GUT’s).

Grand Unification and Proton Decay

The earliest GUT’s were proposed by Pati and Salam¹⁶ (1973, 1974), who used the gauge symmetry $SU(4) \otimes SU(4)$, and by Georgi and Glashow¹⁷ (1974),

whose “minimal” SU(5) model was the simplest theory consistent with the standard model, G_S . The theories had in common the existence of new “X bosons”, which could transform quarks into leptons, thus violating conservation of baryon number.

In the Pati-Salam model, proton decay could be achieved by the simultaneous decay of three quarks: $p \rightarrow \ell\bar{\ell}q\bar{q}$, and the extraordinary lifetime could be explained in terms of phase space suppression. The mass of the X bosons were predicted¹⁶ at $M_X > 3 \times 10^4$ GeV, and other new phenomena were envisioned to be on the experimental horizon, e.g., right handed vector bosons, and massive neutrinos.

In the Georgi-Glashow model, proton decay could come about by the fusion of two quarks into a (virtual) X boson, and its subsequent decay into an antilepton-antiquark pair: $p(qqq) \rightarrow Xq \rightarrow \bar{\ell}q\bar{q}$. The long proton lifetime could be explained if the X had an extremely large mass,¹⁷ $M_X \geq 10^{15}$ GeV. Of course, this new force was not “superweak” because of a small coupling constant, but because the proton decay rate was suppressed by a factor $(m_p/M_X)^4$. A major success of minimal SU(5) was its prediction of $\sin^2 \theta_W = \frac{3}{8}$, which, when renormalized to present energies,¹⁸ yielded substantial agreement with experiment.

Further candidates for a unifying symmetry were subsequently studied,¹⁹ most of which predicted proton decay (although some models could accommodate proton stability). However, no theory had the combined simplicity and predictive power of minimal SU(5).

The idea of using a “full gauge group,”¹⁹ G (which contained the standard model, $G \supseteq G_S$), to explain the known forces, would have been futile if no explanation could be made as to the different strengths of the coupling constants, g_1, g_2, g_3 . If G existed, it must be broken at present energies, and the coupling constants must all approach the same value, g , at some grand unification mass scale $M \sim M_X$ (above which G becomes a good symmetry).

In 1974, Georgi, Quinn and Weinberg²⁰ used the scaling laws of the renormalization group to extrapolate the coupling constants out to the point where they converged. Under the SU(5) assumption, they estimated $M_X \sim 10^{15}$ GeV, and they reasoned on dimensional grounds that the proton lifetime $\tau_p \sim M_X^4/m_p^5 \sim 10^{31}$ years.

A much more sophisticated calculation was carried out by Buras *et al.*²¹ (1977), and later this was improved by Goldman and Ross²² (1979), who, by assuming the value for the QCD mass scale, $\Lambda^2 = 0.1 \text{ GeV}^2$, predicted $M_X = 2.7 \times 10^{14}$ GeV, and $\tau_p \sim 4 \times 10^{30}$ years.

Further work by various authors (including Machacek²³ (1979), Donoghue²⁴ (1980), Golowich²⁵ (1980), Kane and Karl²⁶ (1980)), led to *exclusive* calculations of the proton lifetime of the order 10^{30} years (see Chapter 2). Their predictions of SU(5) branching ratios (see section 8.2) tended to favor the dominance of $e^+\pi^0$ and $e^+\omega^0$ modes, and generally, the dominance of modes containing e^+ and $\bar{\nu}$ over μ^+ . For the case of Higg's dominated decay,²³ the modes containing e^+ would be suppressed relative to μ^+ modes by a factor $(m_e/m_\mu)^2$.

The error associated with lifetime predictions derived from many sources,²⁷ the major ones being due to the estimates of the hadronic matrix elements (derived from bag model or SU(6) wavefunction calculations), and from the poorly determined QCD scale,²⁸ $\Lambda = 160_{-80}^{+100}$ MeV, which came into the calculation to the fourth power. Of lesser importance were the effects of renormalization uncertainties, the number of families, the number of superheavy Higgs, etc.

Langacker²⁹ (1982) gives the following prediction for SU(5) based on the work of various authors:

$$\tau_p(\text{years}) = 3.2 \times 10^{29 \pm 1.3} \left(\frac{\Lambda}{0.16 \text{ GeV}} \right)^4. \quad (1.1)$$

Substituting the value for Λ gives:

$$\tau_p(\text{years}) = 3.2 \times 10^{29_{-2.5}^{+2.1}}. \quad (1.2)$$

Lifetime predictions from theories other than minimal SU(5) were difficult on account of various undetermined parameters; however, as pointed out by Weinberg³⁰ (1979), and Wilczek and Zee³¹ (1979), the dominance of particular branching modes, relations between partial rates, selection rules, and other decay properties could often be determined by the symmetries of a theory. Supersymmetric GUT's³² predicted³³ the dominance of $\bar{\nu}K$ modes for the SU(5) model; Dimopoulos, Raby, and Wilczek³⁴ (1982) predicted a lifetime $\tau_p \sim 10^{30}$ years, with uncertainties depending on the unknown masses of the new supersymmetric particles.

In Chapter 2, we shall further discuss the possibility of distinguishing between Grand Unified Theories through observation of proton decays.

2. Theoretical Considerations

2.1 DISTINGUISHING MODELS

“The very fact of proton decay would be poetic: detailed studies of its decay modes might be our only open window on grand unified interactions.”

—J. Ellis *et al.*²⁷ (1982)

We must first stress that, given the various predictions of the many models of proton decay, it would behoove the experimenter to take the attitude that any decay mode is possible (given conservation of charge, and that, presumably, conservation of energy, momentum and angular momentum hold²⁷ on the length scale $\sim 10^{-28}$ m). Indeed, the primary concern of the experimenter is to first determine whether, in fact, the proton *does* decay. Of course, proof that it does not decay can never be established; but even so, both positive *or* null results would provide valuable information in rejecting inappropriate theories. In this section, we will discuss the various predictions in the context of experimentally distinguishing theoretical models.

Lifetimes. A precise lifetime measurement alone would have limited success in distinguishing models, on account of the rather imprecise predictions. However, a lifetime measurement would be a useful input in any theory, since it would impose a constraint on free parameters. The only exception to this seems to be minimal SU(5), for which a null result giving a lifetime limit in excess of $\tau_p > 10^{31}$ years would cause serious trouble.

ΔL . Proton decay obviously implies lepton number non-conservation, on account of conservation of angular momentum. For the large class of theories, in which no mass scale exists between M_W and the mass of the bosons violating baryon number conservation, M_X , (so called “desert” theories, e.g., minimal SU(5)), it has been shown^{30,31} that $(B - L)$ is conserved up to powers of

$M_W/M_X \sim 10^{-12}$. Pati-Salam type models,¹⁶ and certain classes of decays²⁹ (with dimension-7 operators) involving Higgs bosons conserve $(B + L)$. Experimentally, it would be necessary to be able to determine the lepton charge, which presently is not done. Even so, there could be problems if neutrinos tended to be in the final state.

ΔS . Wilzcek and Zee³¹ (1979) formulated the “kinship hypothesis,” which basically stated that cross-family couplings are small (of the order of the Cabibbo angle), i.e., decays with an e^+ are usually $\Delta S = 0$, and those with a μ^+ are usually $\Delta S = 1$. In some models, proton decay is Higgs mediated, and so decays with a μ dominate. If the kinship hypothesis is assumed, this implies³⁵ the dominance of $p \rightarrow \mu^+ K^0$. For desert theories in general, $\Delta S = 0$ or 1, and so decays to \bar{K}^0 and K^- are forbidden. For supersymmetric theories, νK modes are expected to dominate.^{33,34}

ΔI . In desert theories, $\Delta S = 0$ decays imply relations between the partial rates of branching modes which are related through isospin, e.g.,

$$\Gamma(p \rightarrow e^+ \pi^0) = \frac{1}{2} \Gamma(n \rightarrow e^+ \pi^-). \quad (2.1)$$

Lepton Type. As mentioned above, the ratio of $\mu : e$ decays depends upon the dominance of Higgs mediation. The ratio of $\nu : e$ throws light on spontaneous symmetry breaking of the model and could be used, for example, to distinguish minimal SU(5) from something more complicated, like

$$\text{SO}(10) \rightarrow \text{SU}_c(3) \otimes \text{SU}(2)_L \otimes \text{SU}(2)_R \otimes \text{U}(1). \quad (2.2)$$

For minimal SU(5),

$$\Gamma(p \rightarrow e^+ + \text{any}) = 5\Gamma(n \rightarrow \bar{\nu} + \text{any}) \quad (2.3)$$

whereas for $SO(10)$ with the above decomposition,³¹

$$\Gamma'(p \rightarrow e^+ + \text{any}) = 2\Gamma'(n \rightarrow \bar{\nu} + \text{any}). \quad (2.4)$$

Polarization. For gauge mediated (as opposed to Higgs mediated) decays, it has been shown³⁰ that the leptons have “universal polarizations,” dependent only on ΔS . For example $P_\mu(\Delta S = 0) = -1$, whereas $P_\mu(\mu^+ K^0) = 0.05$. In principle, such a measurement could be made by looking at the direction of the muon decay electron; but in practise, this would require large statistics ($\sim 10^2$ decays).

Lepton Momentum. As we will discuss later, the lepton in two body decays would not be monochromatic if the proton were to decay in a nucleus through diagrams not accessible to free protons. In particular, it has been suggested³⁶ that “three-quark fusion” may dominate in nuclei, giving a single lepton of continuous momentum spectrum, $0 < p_l < m_p$.

2.2 DIRECT NUCLEAR EFFECTS

It is of particular importance to understand the effects of the nuclear medium on proton decay, since, as we shall make clear, great care must be taken in drawing conclusions from the results of experiments which use nuclear protons (and neutrons) as a source. In this section, we shall be concerned with “direct nuclear effects,” i.e., mechanisms in the nucleus which may affect the total decay rate, and the partial decay rates (branching ratios), and we must also consider the possibility of new baryon number violating diagrams. We shall *not*, however, discuss the interactions of (real) mesons as they propagate from a decay through the nucleus; this will be discussed in section 6.3, “Signal Simulation.” As was pointed out by Dover *et al.*,³⁷ these “indirect nuclear effects” only affect experimental efficiencies—not the actual decay rates.

The Two-Quark Overlap Amplitude. In many models of proton decay,^{21,37} the dominant process involves a two-quark interaction at effectively zero range (due

to the high mass of the mediating boson), and so the decay rate has been assumed to be inversely proportional to the effective proton “bag” volume. It is not yet understood if this volume changes significantly in the presence of nuclear matter,³⁸ but we can set a bound on the worst case scenario: if we assume the free proton radius to be²⁷ $R_{\text{free}} \simeq 0.75$ fm, and the bound proton radius to approach the packing limit $R_{\text{bound}} \leq 1.2$ fm, then we find:

$$0.2\Gamma_{\text{free}} \leq \Gamma_{\text{bound}} \leq \Gamma_{\text{free}}. \quad (2.5)$$

So in the worst case for a water Cherenkov detector, for example, the number of proton decays from O^{16} would be comparable to the number from hydrogen (free protons).

For later convenience, let us define a parameter which is the ratio of bound proton to free proton partial decay rates (which is, in general, a function of the nucleus type, and of the decay mode under consideration):

$$\rho = \frac{\Gamma_{\text{bound}}}{\Gamma_{\text{free}}}. \quad (2.6)$$

In general, ρ is due to a combination of effects:

$$\rho = \rho_a \rho_b \rho_c \dots \quad (2.7)$$

where the subscripts “a,b,c,...” stand for a particular mechanism affecting the rates. So, from equation (2.5) we can write:

$$0.2 \leq \rho_{\text{bag}}(p \rightarrow \text{any}) \leq 1. \quad (2.8)$$

We will implicitly assume that any “distortion” of the proton in nuclear matter does not affect any of the following arguments.

Time Dilation, Available Energy, and Phase-Space. In studying the decay rate of the bound muon, R. W. Huff³⁹ assumed that two major factors affecting the decay rate were:

- (a) time dilation caused by the motion of the bound muon relative to the nucleus (i.e., the lab. frame). For any particle decaying with a momentum, k , the rate of decay in the lab. is decreased by a factor

$$\rho_r = \left\{ 1 - \left(\frac{k}{E} \right)^2 \right\}^{\frac{1}{2}}, \quad (2.9)$$

where E is the particle's energy eigenvalue.

- (b) the reduction of phase space available to the decay products due to the lower effective mass of the muon. Any bound particle must have an energy eigenvalue, E , smaller than its vacuum energy (i.e. its rest mass); therefore, any particle momentum, k , reduces the available decay energy in the center of mass frame, Q . Specifically:

$$Q = (E^2 - k^2)^{\frac{1}{2}}. \quad (2.10)$$

In the case of proton decay, time dilation is only a 3% effect, and is independent of decay mode. Phase-space suppression, however, turns out to be much more important, particularly when the phase-space is small to start with. As an example, we use a decay mode of special importance in desert theories. The rate of the quasi-free decay in the nucleus of a proton to an electron plus a meson of mass, m_{meson} , goes as:^{36,40}

$$\Gamma(p \rightarrow e + \text{meson}) \propto Q \left\{ 1 - \left(\frac{m_{\text{meson}}}{Q} \right)^2 \right\}^2, \quad (2.11)$$

with Q given in equation (2.10).

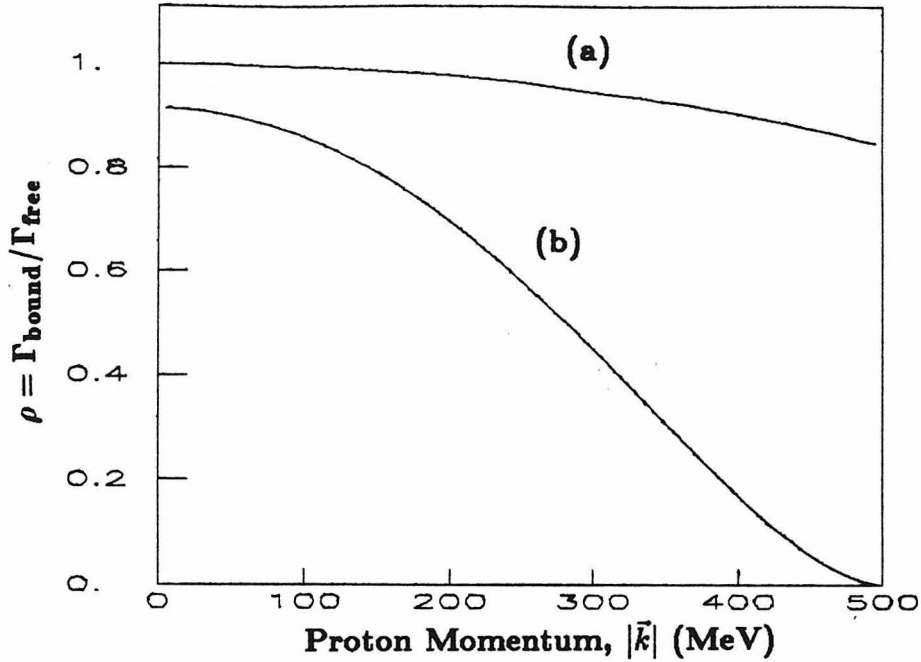


Figure 2-1. Suppression of the proton decay rate in O^{16} , (a) due to time dilation, and (b) due to the available phase-space for $p \rightarrow e^+\omega^0$.

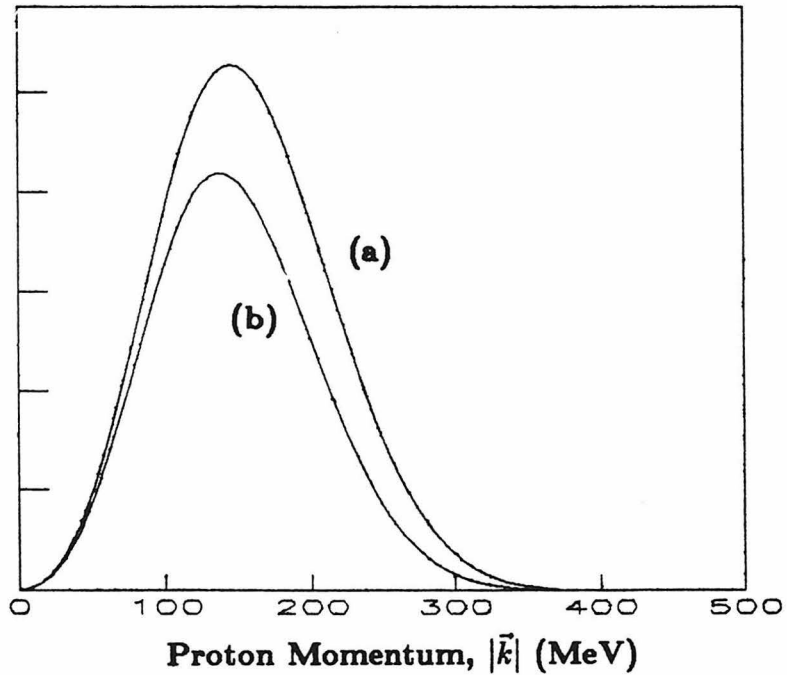


Figure 2-2. Proton momentum distribution in O^{16} (a) for all protons, and (b) for $p \rightarrow e^+\omega^0$. The decrease in the integral reflects the effects in Figure 2-1.

For a preliminary estimate, let us use the ω mass, $m_\omega = 783$ MeV, the mean momentum in O^{16} , $k \simeq 200$ MeV, and energy $E = m_p - E_{\text{binding}} \simeq 931$ MeV. This gives a phase-space reduction relative to free decay by:

$$\rho_{\text{ps}}(p \rightarrow e^+\omega) \simeq 0.7. \quad (2.12)$$

In more detailed calculation, we folded the fermi momentum distribution, $F(k)$, for O^{16} as parameterized by M. Sandel *et al.*,⁴¹ with the time dilation, $\rho_\tau(k)$, and the ratio of bound to free decay phase-space, $\rho_{\text{ps}}(k, m_{\text{meson}})$:

$$\rho_{\text{fermi}}(p \rightarrow e + \text{meson}) = \frac{\int_{k \leq E} F(k) \rho_\tau(k) \rho_{\text{ps}}(k, m_{\text{meson}}) dk}{\int_{k \leq E} F(k) dk}, \quad (2.13)$$

where ρ_{fermi} includes the effects of both time dilation and phase-space. Figure (2-1) shows, as an example, $\rho_\tau(k)$ and $\rho_{\text{ps}}(k)$ for $p \rightarrow e^+\omega$; figure (2-2) shows $F(k)$, the fermi distribution of protons in O^{16} , with the distribution of protons in O^{16} which decay to $e^+\omega$. The decrease in the integral reflects a decrease in the partial proton lifetime in the nucleus. As expected, it is the high momentum tail which is most affected by the lower available energy in the center of mass frame. Figure (2-3) is similar to figure (2-2), showing the available energy to protons in O^{16} , and to those protons in O^{16} decay to $e^+\omega$. Some of our results of the above calculations, are given below:

$$\begin{aligned} \rho_{\text{fermi}}(p \rightarrow e^+\pi^0) &= 0.957, \\ \rho_{\text{fermi}}(p \rightarrow e^+\eta^0) &= 0.909, \\ \rho_{\text{fermi}}(p \rightarrow e^+\omega^0) &= 0.751. \end{aligned} \quad (2.14)$$

The situation of having the resonances ρ and K^* is more complicated; in particular, the shape of the resonance (see section 6.3), is now a function of Q . The phase space available to proton decay is, in turn, a function of both the shape, and the normalization of the resonance curve.⁴² Obviously the K^* of mass 892 MeV, and full width 51 MeV, would be seriously affected (and similarly for decays to $\mu\rho$).

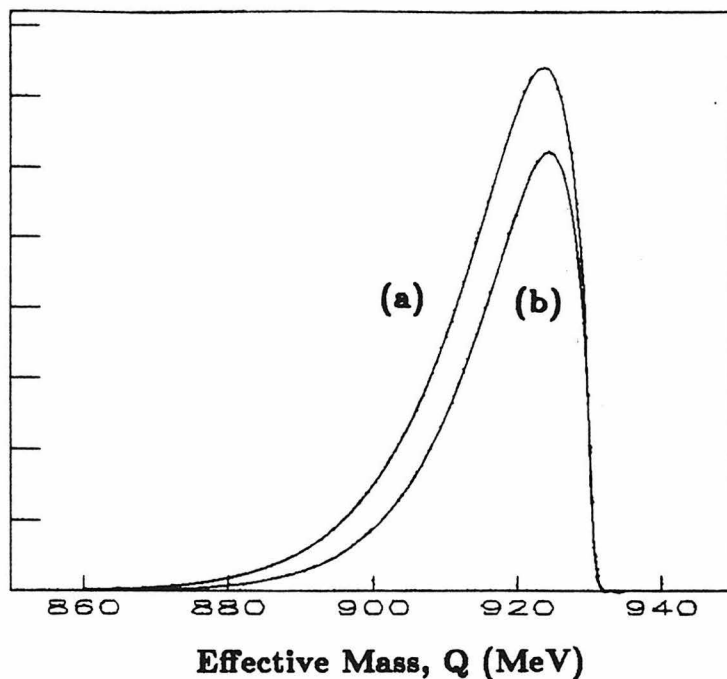


Figure 2-3. Effective mass distribution for protons in O^{16} (a) for all protons, and (b) for $p \rightarrow e^+\omega^0$.

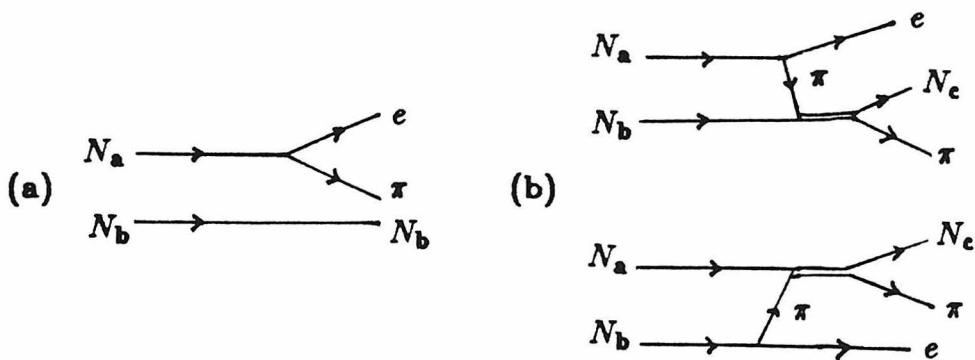


Figure 2-4. Final state interference in $NN \rightarrow Ne\pi$. (a) Quasi-free nucleon decay of N_a , with a spectator nucleon, N_b . (b) Nucleon decay with pion rescattering. The two diagrams could lead to identical final states. Interference may occur between (a) and (b).

Final State Interference. Dover et al.³⁶ first considered the possibility that quasi-free proton decay in the nucleus, figure (2-4a), may interfere with the rescattering process, $NN \rightarrow Ne\pi$, figure (2-4b), where the exchanged pion may be virtual or real. Whether the interference is constructive or destructive depends critically upon the distance between the nucleons. Murthy and Sarma⁴⁰ calculated the effect in O^{16} , making necessary assumptions about the hard core radius of the proton, $R_c \simeq 0.5$ fm, and the range of the exchanged pion, $R_\pi \simeq 2.3$ fm (twice the proton radius). They concluded that the rate enhancement, due to the extra diagrams, figure (2-4b), is more than compensated by destructive interference terms, leaving a net *decrease* in the proton lifetime; e.g., they give the following partial rates pertinent to $p \rightarrow e^+\pi^0$:

scattering rates,

$$\begin{aligned}\Gamma_s(pp \rightarrow e^+\pi^0 p) &= 0.092\Gamma_{\text{fermi}}, \\ \Gamma_s(np \rightarrow e^+\pi^0 n) &= 0.131\Gamma_{\text{fermi}},\end{aligned}\tag{2.15}$$

interference rates,

$$\begin{aligned}\Gamma_i(pp \rightarrow e^+\pi^0 p) &= -0.308\Gamma_{\text{fermi}}, \\ \Gamma_i(np \rightarrow e^+\pi^0 n) &= -0.408\Gamma_{\text{fermi}},\end{aligned}$$

where Γ_{fermi} is just the quasi-free rate. Hence, using equations (2.15), we can write:

$$\begin{aligned}\rho_{s\oplus i}(p \rightarrow e^+\pi^0) &= \frac{\Gamma_i + \Gamma_s + \Gamma_{\text{fermi}}}{\Gamma_{\text{fermi}}}, \\ &= 0.223 - 0.716 + 1, \\ &= 0.51,\end{aligned}\tag{2.16}$$

where $\rho_{s\oplus i}$ is the combined effect of scattering and interference. Comparable results are obtained for $n \rightarrow e^+\pi^-$.

If we also consider that the indirect effects (section 6.3) of pion interactions lead to about a 50% reduction in detection efficiency, then we see that the number

of expected $p \rightarrow e^+\pi^0$ for O^{16} , which would be observed in a water Cherenkov detector, would be reduced to the level expected from the hydrogen (since the ratio of free to bound protons is 0.2).

Although rescattering processes give a lepton with a non-unique energy and opening angle with respect to the meson, the resulting distributions in ref. 40 do not appear to be significantly more detrimental to the detection efficiencies as those due to fermi motion alone.

Interference between different branching modes of proton decay through diagrams in figure (2-4b), where the exchanged pion is replaced by some other meson which rescatters and produces a pion, are considered to give much smaller effects due to the suppression of the nucleon-nucleon correlation at the hard core radius.⁴⁰

Virtual Meson Absorption. The process of proton decay to a lepton plus a *virtual* pion figure (2-5), was again first considered by Dover *et al.*³⁶ for the case of He^4 , who found an enhancement in the decay rate by 12%, and predicted that this effect would be higher for O^{16} . A calculation by Murthy and Sarma⁴⁰ indicated that $NN \rightarrow Ne$ may increase the rate O^{16} by:

$$\frac{\Gamma_{\text{abs}}(NN \rightarrow Ne)}{\Gamma_{\text{fermi}}(N \rightarrow e\pi)} \geq 0.3. \quad (2.17)$$

This result was later confirmed by Kisslinger's work⁴⁴ with the "Hybrid Model." These events have electrons with energies in the range 480-790 MeV, with a peak at around 650 MeV; the accompanying nucleon is emitted at an opening angle greater than 140° with a kinetic energy upto 400 MeV (below Cherenkov threshold). Therefore, this enhancement in decay rate is not of much help experimentally, since it is likely that such decays look like the background atmospheric neutrino interactions (section 3.4).

Three-Quark Fusion. To conserve momentum, three-quark fusion, figure (2-6) would only occur in the presence of a field, such as the strong field of other

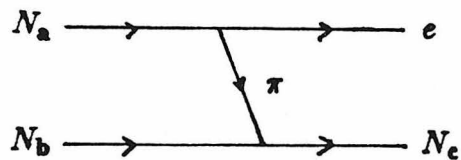


Figure 2-5. Virtual pion absorption in $NN \rightarrow Ne$.

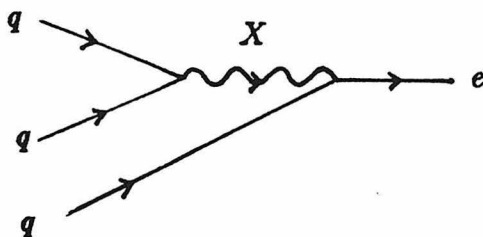


Figure 2-6. Three-quark fusion in the nucleus, giving an electron with a continuous spectrum, and recoiling nuclear fragments.

nucleons. When calculating SU(5) branching ratios, Jarlskog and Yndurain³⁷ estimated that this process would contribute less than 30% to the total rate of decay in the nucleus. Although it is phase space favored by a factor of 2π , the probability of coherent interaction is small, and of the order $(m_\pi/m_N)^2$.

However, three-quark fusion was later studied by Fernandez de Labastida and Yndurain,⁴⁴ who did an inclusive calculation. They found that three-quark fusion would dominate over the standard two-quark process by a factor of (3 ± 1) . The signature would be an electron with a broad spectrum peaking at 600 MeV, plus nuclear fragments which are probably $\Delta_{33} \rightarrow N\pi$ dominated, giving a pion of energy around 350 MeV which would have little direction correlation with the electron. Again, this is not optimized for experimental detection, and would be more background limited than the standard two-quark modes of decay—even if they did dominate by a factor of 3—due to the lack of constraint on the observables.

Conclusions. We have discussed various mechanisms which may change the nature of proton decay in the nucleus, including changes in the total lifetime, the partial lifetimes, the lepton spectrum, the invariant mass and momentum of decays (and how these distributions are branching mode dependent), and the possibility of decay modes which are unavailable to the free proton. The calculations involving the two-quark overlap amplitude, final state interference, virtual meson absorption, and three-quark fusion, are characterized by their sensitivity to the various assumptions made; and consequently, their degree of importance is uncertain. The effects of time dilation and phase space, however, are more intuitively obvious: there will certainly be a decrease in the decay rate, particularly for branching modes with heavy mesons in the final state.

For the theoretically interesting nucleon decay modes, $N \rightarrow e\pi$, we conservatively estimate $\rho = 0.3 \pm 0.2$ in O^{16} . This is based on equations (2.8) and (2.16), and the error is assumed to be dominated by the calculation of the two-quark overlap amplitude. We shall explicitly use this estimate in section 8.2, where the

SU(5) model will be considered.

Interestingly, there does not appear to be a mechanism which *increases* the rate of decays which appear as the standard quasi-free type. In fact, there is the possibility that the rate of identifiable decays per proton from the nucleus may be substantially reduced relative to free protons (though, by not more than an order of magnitude). This raises the following points for consideration:

- (a) Many results by present experiments are not quoted in the most conservative way. They include estimates of the effects of meson transport through the nucleus, but they assume no difference between the free and bound decay rates, i.e., $\rho = 1$; nor do they assume any difference in detection efficiency due to any of the effects discussed.
- (b) It is incorrect to consider such published results as “model independent,” due to the implicit assumption, $\rho = 1$.

In order to overcome these difficulties, we will consider the following solutions, which will help to clarify the interpretation of results:

- (a) The most conservative approach is to assume the worst case: $\rho = 0$. This is equivalent to assuming that any observed proton decay candidate comes from a free proton, e.g., from hydrogen in the water of a Cherenkov detector. In fact, this approach has been taken by Blewitt *et al.*,⁴⁶ with resulting lifetime limits which were comparable to a previous analysis that assumed direct nuclear effects to be negligible.⁴⁷ The disadvantage with this method is that nothing can be said about neutron decay (although this is not a serious problem in the context of GUT's). Also, this proton source must contain hydrogen, so iron calorimeters would be useless in this respect.
- (b) Partial lifetime limits could be given with ρ explicitly, by using the formula:

$$\tau/B = \frac{t_d N_n}{N_c} (\epsilon_f f_f + \rho \epsilon_b f_b), \quad (2.18)$$

where t_a is the detection livetime, N_n is the number of nucleons, and N_c is the number of candidates (if a lifetime measurement is being made), or a confidence level number (if a lifetime limit is being set). The efficiency term, in parenthesis, consists of the following terms: ϵ_f , and ϵ_b are the detection efficiencies for free, and bound decays, respectively; f_f , and f_b are the fraction of free, and bound protons, respectively. The detection efficiency for bound decays can be calculated, e.g., with a Monte-Carlo simulation of meson transport, and fermi motion in the nucleus (see section 6.3). The most uncertain parameter here, is clearly ρ .

For results quoted as in equation (2.18), no distinction is made as to whether a particular candidate is a free or bound proton decay; of course, a good “free” candidate must also be a good “bound” candidate. This means that identical analyses must be used in deriving the efficiencies for free and bound proton decay (in contrast with method (a) above). We note that this equation also applies to neutron decay, and to results from iron calorimeters, by simply setting $f_f = 0$, $f_b = 1$.

(c) Expanding on the above suggestion, results could be given for both the limiting cases of $\rho = 0$ and $\rho = 1$, with the understanding that the “true” answer lies somewhere between the two. This approach was taken in a later “two-prong analysis” by Blewitt *et al.*,⁴⁸ and is the approach taken in this thesis (Chapter 7). In Chapter 8, we will

- (i) use the $\rho = 0$ and $\rho = 1$ results,
- (ii) assume a linear relationship between the lifetime limit and ρ (as in equation (2.18)), and
- (iii) assume a range of possible values for ρ .

This, together with SU(5) branching ratio predictions, will allow us to calculate model-dependent limits on the total lifetime of the proton and neutron, in a way which accounts for possible direct nuclear effects.

3. Experimental Considerations

3.1 THE FIRST PRINCIPLES OF DESIGN

As is true of any experiment, the design parameters (e.g., mass, materials, site, etc.), are often interrelated, and decisions must be made on the basis of certain trade-offs. In this section, we will discuss, quite generally, the factors which constrain the design parameters, and the kinds of advantages and disadvantages which result from final choices. We begin with the most fundamental constraints relevant to the experimentalist: that of previous limits, and theoretical expectations.

Sensitivity. Before the advent of the “dedicated detectors” of the 1980’s, the biggest experimental constraint on proton decay was the Reines and Crouch result in 1974.⁴⁹ Their observations of a 20 ton modular liquid scintillator detector led them to conclude that the proton partial lifetime limit to final states yielding a μ or π^+ was:

$$\tau/B \geq 2 \times 10^{30} \text{ years.} \quad (3.1)$$

The constraint on the final states turns out to be relatively unimportant in the context of GUT’s, since all families of mesons below the proton mass can yield a π^+ (and hence a μ^+). It is also important to note that Reines and Crouch did not make a background subtraction, and that their number of observed events was not inconsistent with the expected background. The theoretical predictions,²⁹ in the range 10^{27-32} years (see equation (1.1)), combined with the above result, provided the incentive to make dedicated searches on a grand scale. So we can conclude that for theoretical and experimental reasons, it would be desirable to design an experiment to be sensitive to lifetimes:

$$\tau/B > 10^{32} \text{ years,} \quad (3.2)$$

for GUT-favored branching modes.

Exposure. We define the exposure:

$$T_d \equiv \epsilon N_n t_d, \quad (3.3)$$

using the notation of equation (2.18). If, after background subtraction, we detect a statistically significant number of candidates, N_c , for a particular proton decay mode with branching ratio, B , then we would be able to obtain a partial lifetime measurement:

$$\tau/B = \frac{T_d}{N_c}. \quad (3.4)$$

The exposure required to achieve a desired sensitivity is actually a function of the background rate. To see this, consider if the expected number of background events was very small, $N_b \ll 1$. The number of candidates constituting a significant signal would be $N_c \geq 1$, and the sensitivity would then be equal to the exposure, rising linearly with time. Now, if the number of expected background events had risen above unity, $N_b \geq 1$, the number of candidates constituting a significant signal is, say,

$$\begin{aligned} N_c &> 3\sigma_b, \\ &= 3\sqrt{N_b}, \\ &= 3\sqrt{\frac{T_d}{\epsilon\tau_b}}, \end{aligned} \quad (3.5)$$

where τ_b is the mean time per nucleon between background events. Hence we now have the sensitivity rising with the *square root* of the exposure, and is inversely proportional to the square root of the background rate. Let us formally write down this important result:

$$\tau/B < \begin{cases} T_d, & \text{for } N_b \ll 1; \\ \frac{1}{3}\sqrt{T_d\epsilon\tau_b}, & \text{for } N_b \geq 1. \end{cases} \quad (3.6)$$

As we shall show in our analysis in Chapter 7, typical ranges for the efficiency and background are $\epsilon = 0.1-1$, and $\tau_b = 10^{32-33}$ years/nucleon. If we substitute

these values into equation (3.6) and use the desired sensitivity, equation (3.2), we find the required range of exposure:

$$T_d \sim 10^{32-34} \text{ nucleon-years.} \quad (3.7)$$

A very important conclusion can be drawn from equation (3.6): the neutrino background makes it almost impossible for a terrestrial experiment of this type to probe a proton lifetime in excess of $\tau > 10^{34}$ years, because of the square root dependence of the sensitivity on the exposure. This also implies that now, since detector sizes of $\sim 10^{33}$ nucleons have been built, factors of four in size (or livetime) provide only factors of two in sensitivity. Another conclusion which can be used as a guide to an effective analysis is that, if $N_b \geq 1$, the sensitivity would go linearly with the efficiency, but with the inverse square root of the expected number of background events. Therefore, to maximize the sensitivity, we should maximize $\epsilon/\sqrt{N_b}$, and *not* ϵ/N_b , as one may naïvely expect.

We note in passing, that full use of the exposure requires a reliable estimate of the background (see sections 3.3 and 6.4) in order to enable a background subtraction (Chapter 7), and the expected background rate depends upon the branching mode under investigation (and the ingenuity of the analysis!).

Mass. So, given the additional constraint that the experiment itself has a livetime $t_d < 10$ years, we see that we need an efficient detector containing:

$$N_n = \frac{T_d}{\epsilon t_d} \sim 10^{33} \text{ nucleons.} \quad (3.8)$$

This constitutes an active mass of the order of $M_d \sim 1$ kilotonne. As reasoned above, having a fiducial mass greater than this is of limited benefit.

Density and Size. The dimensions of the detector will be of the order

$$L_d \sim \frac{10 \text{ meters}}{\rho^{\frac{1}{3}}}, \quad (3.9)$$

where $\rho \equiv 1$ for water. It is important that a large fraction of possible decays would be fully contained within the detector in order to be able to measure the energy of an event. Since the decay products have a typical range of $\lambda \sim 2/\rho$ meters, and that we require $\lambda \ll L_d$, we find the constraint:

$$\rho \gg 0.1 \tag{3.10}$$

Fortunately, this is can be easily met, provided our source is liquid or solid. An interesting example of a material not fulfilling this criteria is liquid hydrogen. In addition to this, liquid hydrogen has the problem that the radiation length is more than 8 meters. To further increase the percentage of fully contained events, and to help reject (either physically, or in software) any entering particles, it is beneficial to define a “fiducial volume” within the total volume of the detector. This leads to an increase in the required detector size. If the distance between the fiducial volume and the sides of the detector are $\sim \lambda$, then the exluded mass constitutes

$$\frac{\Delta M}{M} \sim \rho^{-\frac{1}{3}} \tag{3.11}$$

of the total (e.g., a water Cherenkov detector’s mass must be doubled). So, the more dense the detector is, the less ‘wasted’ mass we have (and even less wasted volume).

Decay Source. This question of cost raises its head here, and for other reasons we shall discuss, it is fortunate that simple water turns out to be an excellent candidate for use as a proton decay source *and* as a detection medium. The basic principle behind water Cherenkov detectors, is that charged particles travelling faster than the speed of light in water, $\beta > 1/n \sim 0.75$, emit Cherenkov radiation at a characteristic angle to the track (see section 3.2). This light can then propagate through the water and be detected by photomultiplier tubes, which can give information on the time development, topology, and energy of an event.

To this end, the water must be purified to have an attenuation length

$$\lambda_{\text{atten}} > 10 \text{ meters}, \quad (3.12)$$

given the detector size in equation (3.9).

Here are some of the advantages of a water Cherenkov detector:

- Water is certainly the cheapest medium available.
- The detector fiducial volume can be made homogeneous, and totally active.
- The detector response can, in principle, be made isotropic.
- The sense of track direction is totally unambiguous, thus the question never arises as to whether a track entered or exited the detector.
- 20% of the protons in water are free. Section 2.2 explains why this is extremely attractive.
- The nuclear interactions of decay products in water are less than those in, say, iron.
- It optimised for detecting $p \rightarrow e^+\pi^0$, and other two-prong modes favored by the SU(5) model.
- The efficiency for detecting the presence of a muon in an event, through $\mu \rightarrow e\nu_e\nu_\mu$ can be made very high (*in principle*, $\sim 100\%$ for μ^+ , and $\sim 80\%$ for μ^-). Apart from being useful in rejecting background, this is of particular importance if emphasis is made in searching for Pati-Salam type modes with more than 2 muons in the final state (e.g., see More's thesis⁵⁰).

The disadvantages are as follows:

- Primarily, the ability to resolve tracks with opening angles $\theta < 90^\circ$ is poor. This causes considerable problems in counting precisely how many tracks an event has.

- The Cherenkov threshold for charged particles corresponds to $E > 1.52 m$, where E is the total particle energy, and m is the rest mass; so particles below or slightly above this threshold are not detected.
- Particle identification is poor, though this is not a big problem if the detection efficiency is high for proton decay, and the estimated background is very low.
- As argued above, the density of water requires not only a large fiducial volume, but also an approximately equal volume of water outside of this. Hence a “good” water Cherenkov detector is going to have dimensions 10–20 meters (see equations (3.9) and (3.11)). This is basically a logistical problem which can easily be coped with. However, it also makes it very difficult to test a full size Cherenkov detector in a neutrino beam. The fact that the detector presents a large effective area to cosmic ray muons is solved simply by placing the detector deep enough.

Another viable option is the use of iron as a source, interspersed with other materials to provide detection capability. This type of detector has the complementary advantages and disadvantages outlined above. A nice feature of these detectors is their ability to resolve multi-track events, and to see the tracks of particles which would have been below Cherenkov threshold—this makes them optimised for many body decays. However, the limited resolution of its sense of track direction can confuse a single scattering track for a two-body event. A major disadvantage is their lack of free protons, making a thorough understanding of nuclear effects crucial to any conclusions.

Depth. In order to keep the background as low as possible, and to limit the amount of irrelevant data acquired, it is necessary to situate the detector at least $\sim 10^3$ m.w.e. (meters water-equivalent) below the Earth’s surface. The background due to atmospheric neutrinos is, of course, essentially depth independent. It is not desirable to reduce the flux of cosmic ray muons too much,

since they provide excellent calibration tracks (section 4.3), and enable continuous checks on the detector performance. Apart from the question of proton decay, these muons are interesting to study in their own right for signs of new physics (e.g., see Svoboda's thesis⁵¹). We will discuss the background further in section 3.3.

3.2 USING CHERENKOV RADIATION FOR DETECTION

Introduction. Cherenkov radiation is caused by the polarization of dipoles as a charged particle propagates in the water faster than the local speed of light:

$$\beta > \frac{1}{n} = 0.75, \quad (3.13)$$

where n is the refractive index of water.

It can be easily verified by Huygen's construction, that the photons are emitted at a characteristic angle to the track, which is only a function of the particle speed, and the local speed of light:

$$\theta_c = \cos^{-1} \left(\frac{1}{\beta n} \right) \leq 42^\circ, \quad (3.14)$$

where θ_c , is called the "Cherenkov angle."

The number of photons emitted per cm of track per unit frequency is flat, and is proportional to $\sin^2 \theta_c$: ⁵²

$$\begin{aligned} \frac{dN}{d\lambda} &= \frac{2\pi}{137\lambda^2} \left(1 - \frac{1}{\beta^2 n^2} \right); \\ N(\lambda_1 \text{ to } \lambda_2) &= \frac{2\pi}{137} \left(\frac{1}{\lambda_1} - \frac{1}{\lambda_2} \right) \left(1 - \frac{1}{\beta^2 n^2} \right), \end{aligned} \quad (3.15)$$

where, in the last equation, we have assumed $n(\lambda) \simeq \text{constant}$ in the wavelength range of interest. To get a feel for the numbers involved, typical photomultiplier tubes (P.M.T.'s) detect photons in the range $\lambda_1 = 300 \text{ nm}$ to $\lambda_2 = 600 \text{ nm}$, for

which $n = 1.34$, hence $N \sim 300 \text{ cm}^{-1}$ for $\beta = 1$. As we shall see later, this is more than adequate as a means for reconstructing the typical energies and topologies of proton decay events.

From the above discussion, we see that Cherenkov photons could provide various pieces of information for the purpose of event reconstruction:

- (a) Relativistic charged tracks are characterized by cones of light. The time of arrival of photons and the detected “hit pattern” topology can be used to determine the direction, and vertex of a track. The sense of direction of a track is never ambiguous.
- (b) Given a particle hypothesis for a given track, tables of dE/dx in water can be used to infer the initial particle energy from the total amount of light associated with the track.

We will now go into more detail on the “visible” structure of tracks at the energies relevant to proton decay. An understanding of this is necessary for event reconstruction. We will also generally discuss the detection of photons in water Cherenkov detectors, and how proton decay may be observed. First of all, we shall introduce some useful concepts relating light yield to track energy.

The Concept of Radiating Track Length, r_c . From equation (3.15), the number of photons produced by a segment of charged track is only a function of the particle speed. The total amount of light emitted by a particle along its track depends on its initial energy, and its dE/dx curve. We define a very convenient parameter, $r_c(E)$, the “radiating track length,” which is the length of a $\beta = 1$ track segment that would yield the same number of photons as a track produced by particle of initial energy E (note that this is a function of particle type):

$$\begin{aligned}
 r_c &= \int_{\beta > \frac{1}{n}} \frac{1 - 1/(\beta(x)^2 n^2)}{1 - 1/n^2} dx, \\
 &= \int_E^{1.52m} \frac{n^2 - 1/(1 - m^2/E^2)}{(n^2 - 1) dE/dx} dE.
 \end{aligned}
 \tag{3.16}$$

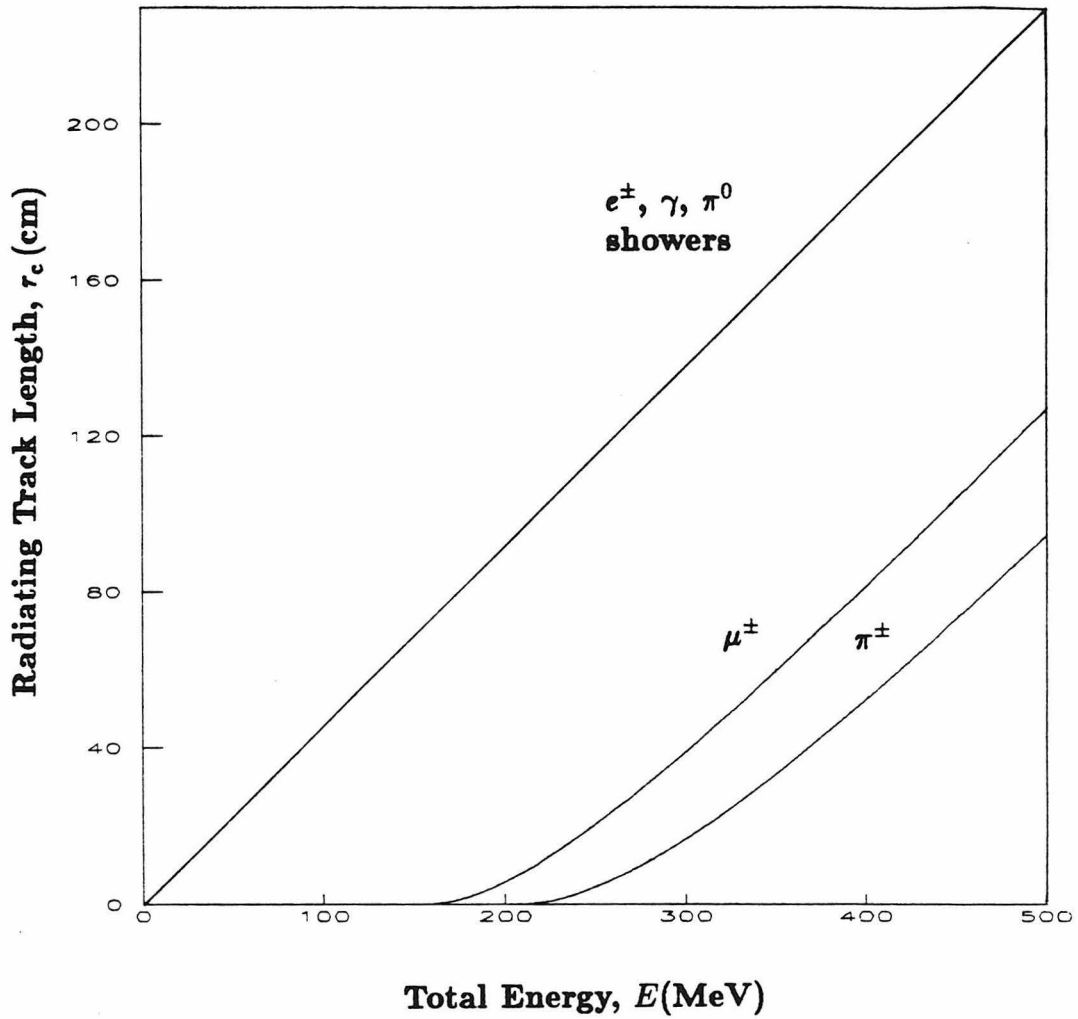


Figure 3-1. Radiating track length vs. energy for particles in H_2O . The “visible energy,” E_c , of each particle can be found by finding the shower energy of equal radiating track length. The EGS Monte-Carlo gives $E_c(\text{MeV}) = 2.18 r_c(\text{cm})$ for showers.

We carried out the above calculation for various particles using published dE/dx curves,⁵³ and some of the results have been plotted in figure (3-1) for the energy range appropriate to proton decay products. For electrons and gammas, we used the EGS Monte-Carlo program,⁵⁴ and followed each particle in the shower to deduce the total radiating track length. We found the ratio of the initial shower energy to the mean radiating track length,

$$E_{\text{shower}}/r_c = 2.18 \text{ MeV cm}^{-1} \quad (3.17)$$

to be constant to better than 1% in the energy range $E = 50\text{--}1000$ MeV. The light yield fluctuations for showers in this range fit well to the law:

$$\frac{\sigma_r(E)}{E} = \frac{1.5\%}{\sqrt{E(\text{GeV})}}. \quad (3.18)$$

The Concept of Visible Energy, E_c . It would be useful, conceptually, to define the light yield in units of energy of a "standard track." Since, as we showed above, the light yield from showers is very linear with energy, then we choose to define the "visible energy", E_c , of a track (or, of an entire event) as the energy of a shower which would produce the equivalent light yield:

$$E_c \equiv 2.18 r_c(E). \quad (3.19)$$

Absolute Energy Calibration. In principle, one can set the calibration scale of a detector by:

- (a) Initiating showers of a known energy into the detector,
- (b) Firing tracks through the detector such that, essentially $\beta = 1$ for the entire track length. The scale can then be set by using equation (3.19) and, by definition, $r_c \equiv \text{tracklength}$.

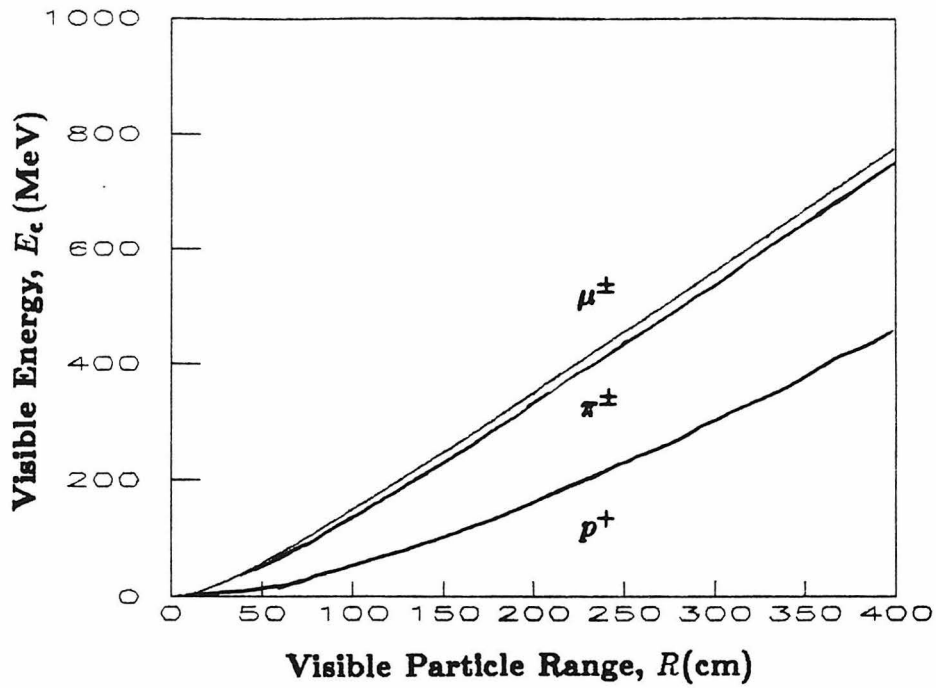


Figure 3-2. Visible energy vs. visible particle range for μ^\pm , π^\pm , and p^+ . The Cherenkov threshold corresponds to $R = 0$.

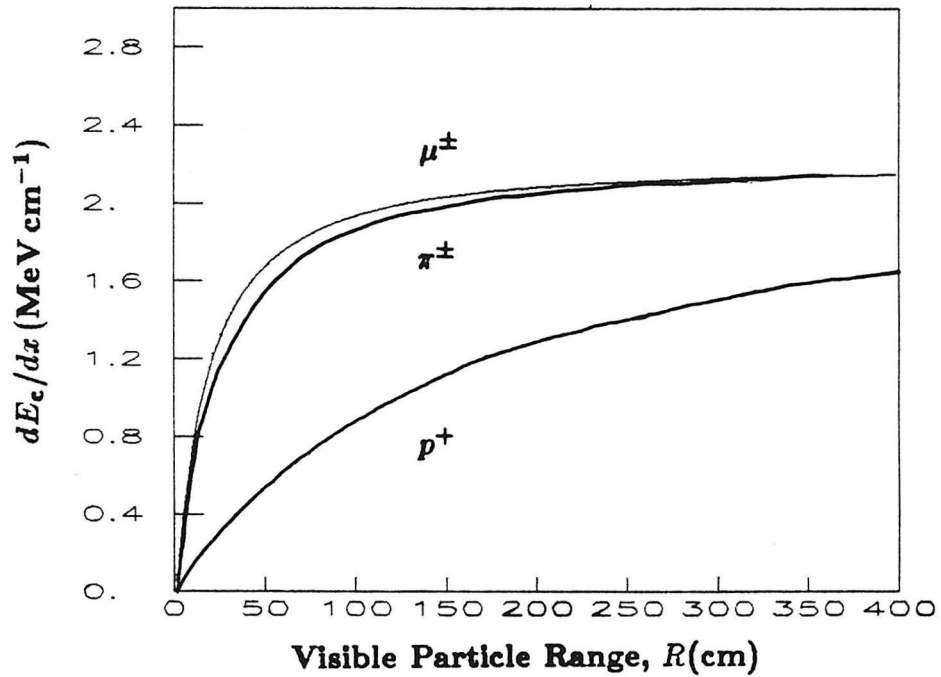


Figure 3-3. dE_c/dx vs. visible particle range for μ^\pm , π^\pm , and p^+ .

In practice, however, (a) is difficult to arrange; so (b) is used by observing cosmic ray muons passing through the detector. However, as we shall discuss in section 4.3, some modifications are required due to electromagnetic processes caused by muon interactions in the water.

Visible Track Structure. Using the above formulas for this section, we generated the plots in figures (3-2), (3-3), and (3-4) showing how E_c , dE_c/dx , and θ_c various quantities vary as a function of the true visible track range, R , as measured from the point at which Cherenkov radiation ceases. The rapid collapse of the Cherenkov angle, and the decrease in dE_c/dx at the end of a track, combine to produce the characteristic Cherenkov ring pattern, with light intensity dropping of as $1/r$ —the constant line source approximation—for the portion of the track where $d\theta_c/dx \simeq 0$, and approaching $1/r^2$ —the point source approximation—toward the Cherenkov threshold at the end of the track. We note that the dropoff in light intensity towards the center of the ring is *not* a consequence of the particle's lower β —actually the intensity normal to the light is *independent* of β —but is a consequence of a finite $d\theta_c/dx$ causing a finite angular spread of light for a given track segment. Formally, the area, dA , into which the light falls from a track segment, dx , at a distance, r , is:

$$dA = 2\pi r \sin \theta_c (\sin \theta_c dx + r d\theta_c), \quad (3.20)$$

where $d\theta_c$ is the change in Cherenkov angle across the segment. Hence we can write the intensity normal to the light,

$$\begin{aligned} I_c &= \frac{dE_c}{dA} \\ &= \frac{1}{2\pi r \sin^2 \theta_c + 2\pi r^2 \sin \theta_c d\theta_c/dx} \frac{dE_c}{dx}. \end{aligned} \quad (3.21)$$

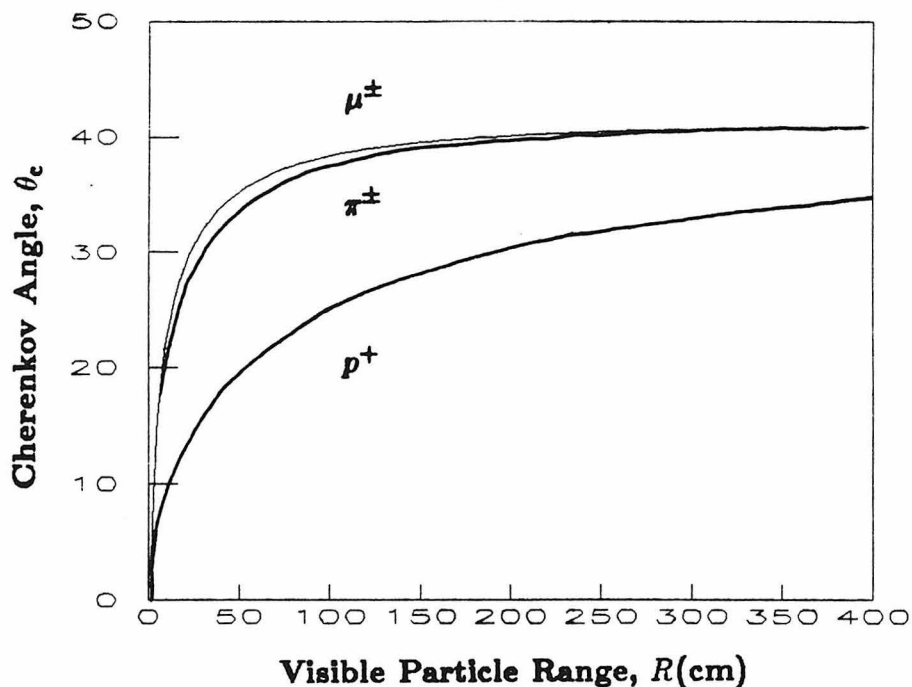


Figure 3-4. Cherenkov angle vs. distance along visible track for μ^\pm , π^\pm , and p^+ .

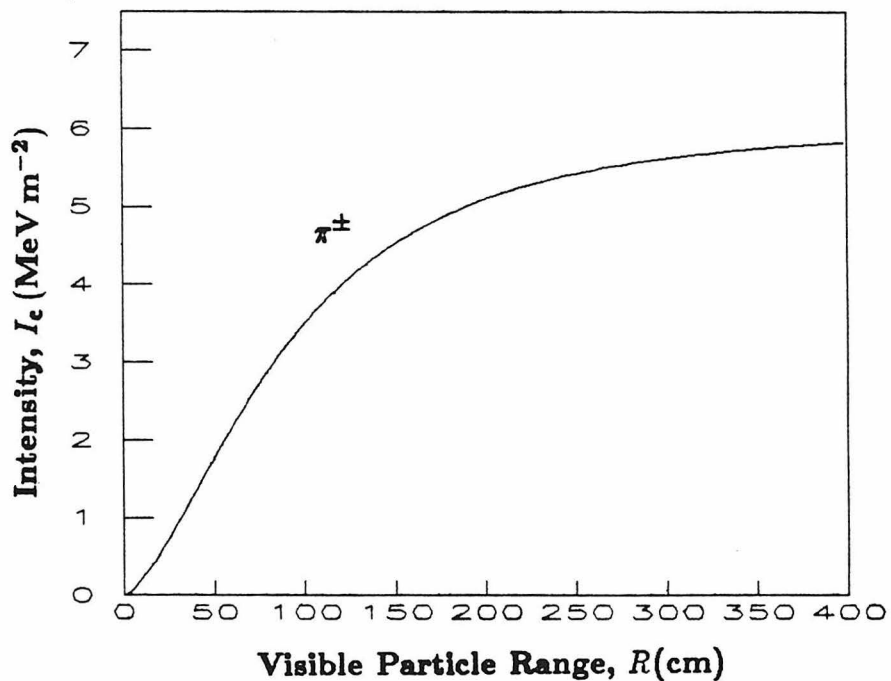


Figure 3-5. Intensity normal to the light vs. distance along visible π^\pm track as seen at 6 meters away. Since the P.M.T.'s are on a 1 meter lattice, the intensity is approximately the visible energy per P.M.T., which is at the ~ 1 p.e. level for our detector.

Now, from equations (3.14), (3.16) and (3.19) we find:

$$\begin{aligned}\frac{dE_c}{dx} &= 2.18 \frac{\sin^2 \theta_c}{1 - 1/n^2} \text{ MeV cm}^{-1} \\ &= 2.30 \sin^2 \theta_c \text{ MeV cm}^{-1},\end{aligned}\tag{3.22}$$

and substituting this into (3.21) gives:

$$I_c = \frac{36.3}{r + (r^2/\sin \theta_c) d\theta_c/dx} \text{ MeV m}^{-2},\tag{3.23}$$

where r is measured in meters. This equation is conceptually useful, because the P.M.T.'s in our detector are spaced on a 1 meter lattice, hence I_c expressed in MeV m^{-2} is, theoretically, the visible energy seen per P.M.T. at a distance r , and at the Cherenkov angle, θ_c .

We carried out the above calculation, and plotted the π^\pm results for intensity, both as a function of position along the track, figure (3-5), and as a function of Cherenkov angle (3-6). For the latter, we have actually plotted ($r \times I$) with values of $r = 3$ and 9 meters, in order to show the transition from $1/r$ to $1/r^2$ dependence. This transition causes the patterns to appear more ring-like at longer distances, and more disk-like at shorter distances. Due to a similar mass, the μ^\pm give very similar plots.

Figure (3-7) shows the intensity as a function of Cherenkov angle for the proton. This is of special interest, since it may be possible to have protons above Cherenkov threshold from atmospheric neutrino interactions in the detector, and thus creating visible multi-track events. We note that protons with 100 MeV visible energy have $\theta_c < 30^\circ$, and produce rings about three times more intense at these small angles than π^\pm or μ^\pm . Thus we have found a way to, in principle, identify energetic protons.

Showery tracks, for the most part, do not give discernable rings, but instead produce a more filled in hit pattern. However, most of the visible energy is still deposited within $\theta_c = 42^\circ$.

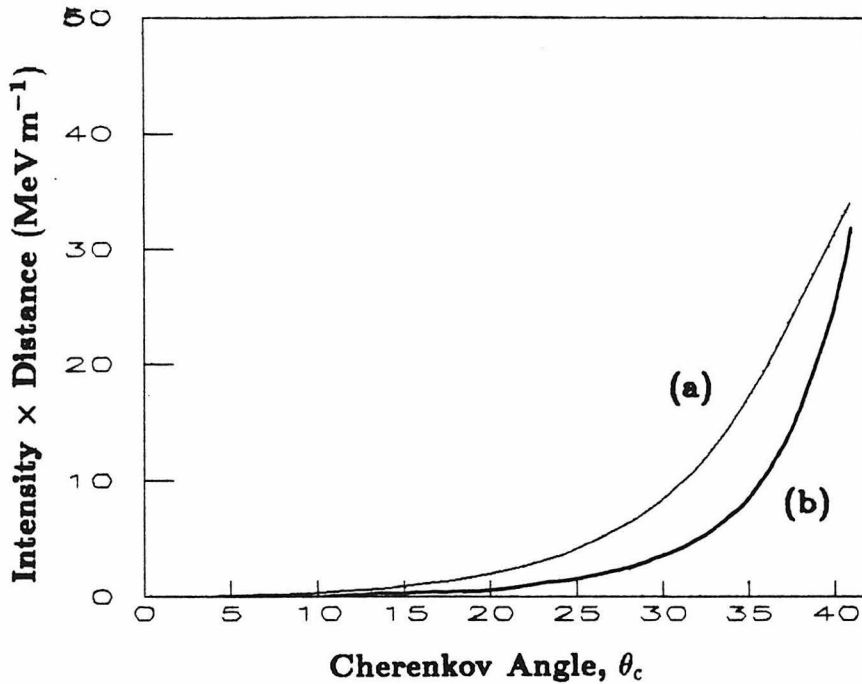


Figure 3-6. (Intensity) \times (distance) from a π^\pm vs. Cherenkov angle, viewed at (a) $r = 3$ meters, and (b) $r = 9$ meters. Note the sharp ring structure, and the transition from $1/r$ to $1/r^2$ dependence at smaller angles.

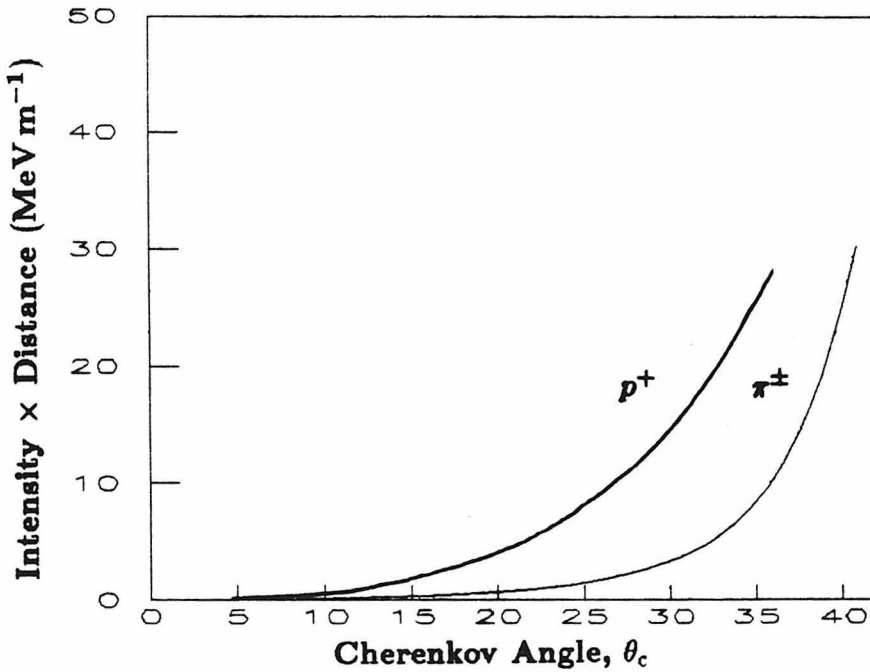


Figure 3-7. (Intensity) \times (distance) from a p^+ vs. Cherenkov angle viewed at 9 meters. Note the more disk-like structure as compared with the π^\pm .

The most important feature of the visible track structure is the presence of the peak intensity at the edge of the Cherenkov ring (see figure (3-6)), and the hard edge produced at the beginning of the track (though, in practice, this is slightly smeared due to light scattering in the water, and Poisson statistics associated with photon collection). This is of particular use in reconstructing the starting point of a track (section 5.2), and hence the “vertex” of an event.

Detector Pixels. A crucial question for the design of a water Cherenkov detector is, “How many data points per event are required to efficiently detect the signal?” We shall perform here some order of magnitude calculations to illustrate how we may go about answering this question.

A fully showering proton decay, e.g., $p \rightarrow e^+ \pi^0$, will deposit a visible energy of $E_c \simeq 940 \text{ MeV}$ just by definition (see above subsection, “The Concept of Visible Energy”). Proton decays with non-showering products will in general deposit lower visible energies due to Cherenkov threshold effects (see figure(3-1)). If, for example, we wish to observe a decay of $E_c \sim 500 \text{ MeV}$ with an energy resolution $\sim 10\text{--}20\%$, then we would require ~ 100 “lit” P.M.T.’s based on counting statistics alone; i.e., we require $\sim 5 \text{ MeV}$ per P.M.T. Now let us consider the P.M.T.’s to be positioned on the walls of the detector in a lattice of some spacing, λ_{lat} . The advantages of a surface array over a volume array were demonstrated in Cortez’s thesis⁵⁵. By equation (3.23), and using the distance between the tubes and the track, $r \sim 10$ meters, we find the intensity, $I_c \sim 4 \text{ MeV m}^{-2}$; therefore we require at least one P.M.T. firing at the single photoelectron (p.e.) level per square meter, so $\lambda_{\text{lat}} \sim 1$ meter. To calculate how big the P.M.T.’s need be, we go back to equations (3.15) and (3.17), and use a typical P.M.T. (quantum \times collection) efficiency $\sim 10\%$ to deduce that 30 p.e.’s per cm, or ~ 15 p.e.’s per MeV would be collected for 100% surface coverage. Since the one p.e. level would correspond to about 5 MeV per P.M.T. on a one meter lattice, only $\sim 1\%$ coverage is required. This corresponds to a P.M.T. diameter of $\sim 10 \text{ cm}$.

This is an estimate of the minimum size P.M.T required, but increasing the

size beyond this is particularly advantageous for resolving events of low visible energy. However, little benefit is gained by increasing the coverage for visible energies greater than about 500 MeV.

The number of “hit” P.M.T.’s is also of importance for the spatial reconstruction of events, and determining the presence of tracks. The timing resolution of the tubes should be of the order of the lattice spacing for adequate spatial reconstruction. This corresponds to $\sigma_t \simeq 4$ ns, which can be easily achieved with the right choice of P.M.T.

3.3 COSMIC RAYS AND BACKGROUND SOURCES

Introduction. It is important to understand the different types of interactions we expect to see in our detector, in order that we may estimate the rate of events which imitate proton decay, and also so we can check to see if the detector is responding as expected. Under typical detector operation, with a visible energy threshold of $\simeq 50$ MeV, the only events which can be caused by known physics come as a result of various cosmic ray interactions—other phenomena, e.g., radioactive decay, are too low in energy.

In this section, we will briefly discuss the production of cosmic ray secondaries, how they may be observed either directly, or indirectly, and to what degree their interactions constitute a background to proton decay.

Atmospheric Interactions. The primary protons interact with the Earth’s atmosphere, producing pions and kaons, whose subsequent decays can yield muons and neutrinos, which are the only particles able to penetrate the experimental overburden. The most important decays are as follows,⁵⁶

$$\begin{aligned}
 \pi^\pm / K^\pm &\rightarrow \mu^\pm + \nu_\mu (\bar{\nu}_\mu), \\
 K_L^0 &\rightarrow \pi^\pm + e^\pm + \nu_e (\bar{\nu}_e), \\
 K_L^0 &\rightarrow \pi^\pm + \mu^\pm + \nu_\mu (\bar{\nu}_\mu), \\
 \mu^\pm &\rightarrow e^\pm + \nu_e (\bar{\nu}_e) + \bar{\nu}_\mu (\nu_\mu).
 \end{aligned}
 \tag{3.24}$$

The ratio of $\mu^+ : \mu^-$ is 1.25—basically following the ratio of $\pi^+ : \pi^-$ production by the primary interactions. The ratio of the various neutrino types, however, is a little more complicated, and is a function of zenith angle due to the varying atmospheric slant depth and the finite lifetime of the muon. Electron neutrinos come predominantly from muon decay for energies < 10 GeV, so the ratio of $\nu_e : \bar{\nu}_e \simeq 1.25$. The contribution of muon decay to muon neutrinos, however, becomes strongly affected by zenith angle for energies around 10 GeV due to the increased muon pathlength in the atmosphere at 90° , and the higher fraction of energy given to the neutrino as compared with that from pion decay. This effect is also responsible for a slight enhancement in the neutrino flux from horizontal directions.

Direct Detection of Muons. The penetrating, vertical, cosmic ray muon intensity as a function of depth can be approximated by a power law for shallow depths when ionization losses dominate, and by an exponential law for depths > 2000 m.w.e., when bremsstrahlung and nuclear collision losses become important.⁵⁷ At our intermediate depth of $h = 1600$ m.w.e., the following empirical fit is a good approximation,^{58,59}

$$I(h, 0^\circ) = \frac{164}{h + 400} h^{-1.53} e^{-0.00065h}, \quad (3.25)$$

where $I(h, 0^\circ)$ is the intensity in units of $\text{cm}^{-2} \text{s}^{-1} \text{sterad}^{-1}$. The zenith angle dependence out to 40° can be expressed for a flat overburden as

$$I(h, \theta) = I(h, 0^\circ) \cos^{n(h)} \theta, \quad (3.26)$$

where n increases with depth; for our depth, $n \simeq 3.0$. It has been shown by Murthy⁵⁹ that the muon rate is actually only a weak function of n in the range 3.0 ± 0.4 . For $\theta > 40^\circ$, equation (3.26) becomes an increasingly worse approximation due to the longer pathlength for atmospheric pions to decay into muons, and for $\theta > 85^\circ$, muons from neutrino interactions in the neighboring rock begin

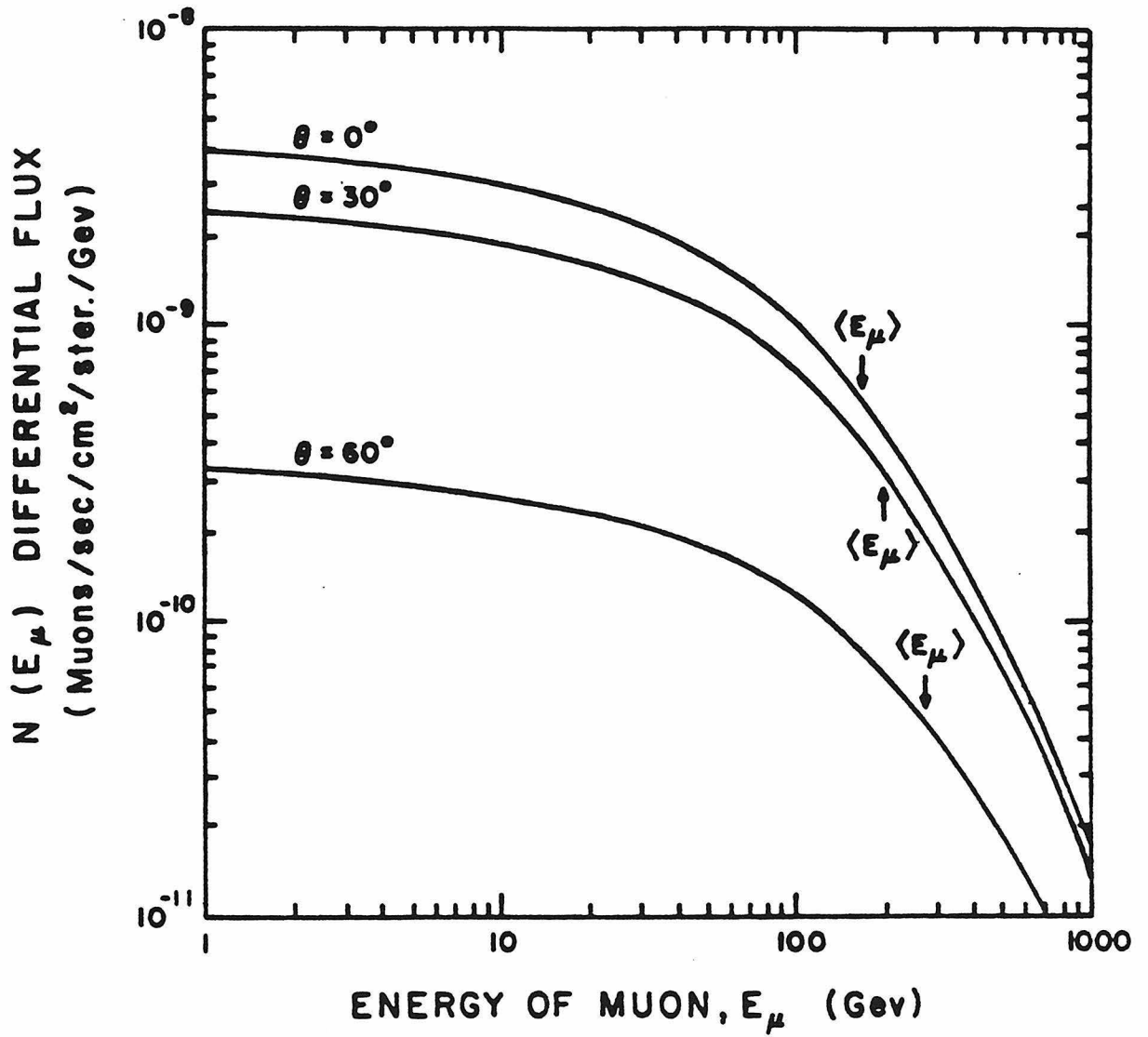


Figure 3-8. Flux of cosmic ray muons as a function of energy and angle. The mean energy of 200 MeV is approximately independent of angle.

to become significant. Murthy calculates a muon rate of 3 s^{-1} at 1600 m.w.e. for a detector of size $20\text{ m} \times 20\text{ m} \times 20\text{ m}$. When scaled to our actual dimensions of $22.5\text{ m} \times 18\text{ m} \times 17\text{ m}$, we expect 2.7 s^{-1} . We note that equation (3.25) shows that the muon intensity drops rapidly in depth, and the muon rate can be reduced by three orders of magnitude by going four times deeper. To answer the question of whether this is necessary, we need to understand at what level direct muons constitute a background.

Figure (3-8) shows the flux of muons as a function of energy. The spectrum is approximately flat out to 100 GeV, with a mean at around 200 GeV. Since muons with energies greater than 4 GeV pass straight through the detector, we expect about 2% to enter and stop. Even though a sizeable fraction of direct muons deposit energies in the "dangerous" region below 1 GeV, the probability that they will imitate proton decay is entirely negligible compared to the neutrino background discussed below. The reasons are as follows:

- (a) Direct muons have an "entry signature" in which the first P.M.T.'s that fire in the event are on the wall directly opposite to the main Cherenkov pattern. The entry signature is caused by Cherenkov radiation from water up to about 50 cm outside of the P.M.T. planes. Since we use hemispherical P.M.T.'s, they are sensitive to incident angles greater than 90° from their symmetry axis.
- (b) Even in the absence of an entry signature, timing and geometrical data from each P.M.T. allows us to reconstruct the point at which the track began radiating, which is at the wall of the detector. We impose an additional constraint that the reconstructed vertex be at least 2 meters from the nearest P.M.T. plane. This defines our "fiducial volume," within which events are called "contained." The probability that a muon does not create any p.e.'s in less than 2.5 meters of track is $\simeq e^{-75}$. Since we only retain events we find to be contained, the muons should pose no problems with respect to background.

- (c) Since proton decays (and neutrino events) would occur homogeneously and (almost) isotropically in the detector, a systematic check on the reconstructed vertex distribution, would provide a very accurate estimate of any possible entering contamination. Also, entering muons are very strongly peaked in the downward direction, making any contamination even more obvious.

Indirect Detection of Muons. We define “indirect detection” to mean that we detect the products of a muon interaction in the neighboring rock without actually seeing the muon itself. We note first that if a muon interaction was preceded or succeeded by its entering the detector, it may be rejected for the same reasons given above.

Interactions in the neighboring rock are potentially dangerous if an energetic neutral (thus, non-radiating) particle enters the detector, interacts with the water, and imitates a proton decay. The probability of this occurring is severely limited by the following four factors:

- (a) Only very specific geometries can give rise to indirect detection, e.g., a near vertical muon passing close enough to a wall such that its interaction products reach the detector through the rock.
- (b) The interaction products entering the detector must not be accompanied by charged, radiating particles; otherwise, the event may easily be rejected as entering.
- (c) The neutral particle must traverse *at least* 2.5 meters between the rock and the fiducial volume before interacting. Actually, the distance to the fiducial volume would more typically be of the order 10 meters due to the interaction products being thrown forward and, therefore, downward.
- (d) Even if the above criteria were met, the neutral particle must then interact to give similar visible topologies to proton decay in order for it to become “dangerous.” This requires the production of at least two wide-angled,

visible tracks, each with visible energies in the approximate range $50 \leq E_c \leq 600 \text{ MeV}$.

Indirect observation of muons results from two main types of interactions: electromagnetic shower production, and hadronic shower production.

- (1) Electromagnetic showers could potentially introduce an energetic gamma into the detector. However, the radiation length in water of 35 cm is too short for any significant contamination of contained events (reason (c)). Besides, a gamma would only give a showering track which has none of the topological characteristics of a proton decay event.
- (2) Hadronic showers can yield neutral particles—particularly neutrons—which have typical interaction lengths of around 80 cm in water. Now the work by Khalchukov *et al.* concludes that the neutron flux at a depth of 1500 m.w.e., with energies $> 0.7 \text{ GeV}$, and with no associated muon or charged products is $\sim 10^3 \text{ years}^{-1}$ for a detector of dimensions $10 \text{ m} \times 10 \text{ m}$ in the horizontal plane.⁶⁰ This number also agrees with the work of Grant when scaled to the appropriate depth.⁶¹ He finds the mean angle between the neutron and the muon to be only 5° . This angle would have to be much greater in order for the neutron to reach the fiducial volume—even the few neutrons entering at 30° to the vertical would be attenuated by a factor of $e^{-2.5/(0.8 \sin 30^\circ)} \sim 10^{-3}$. As an estimate of the effect of our veto region, we consider Grant's plot of the neutron distribution in a $10 \text{ m} \times 10 \text{ m}$ detector of twice our density (see figure (3-9)). If we make the scaled veto region 1.25 m wide, we find a total attenuation of the order 10^{-3} . Next, we scale the detector dimensions by a factor of two to deduce that our rate of contamination is $< 10 \text{ events years}^{-1}$ (this number does not even require the events to look like proton decay). Since this rate is only a few percent of the expected neutrino rate, we shall assume this background to be negligible.

Detection of Neutrinos. In terrestrial experiments, the background from neu-

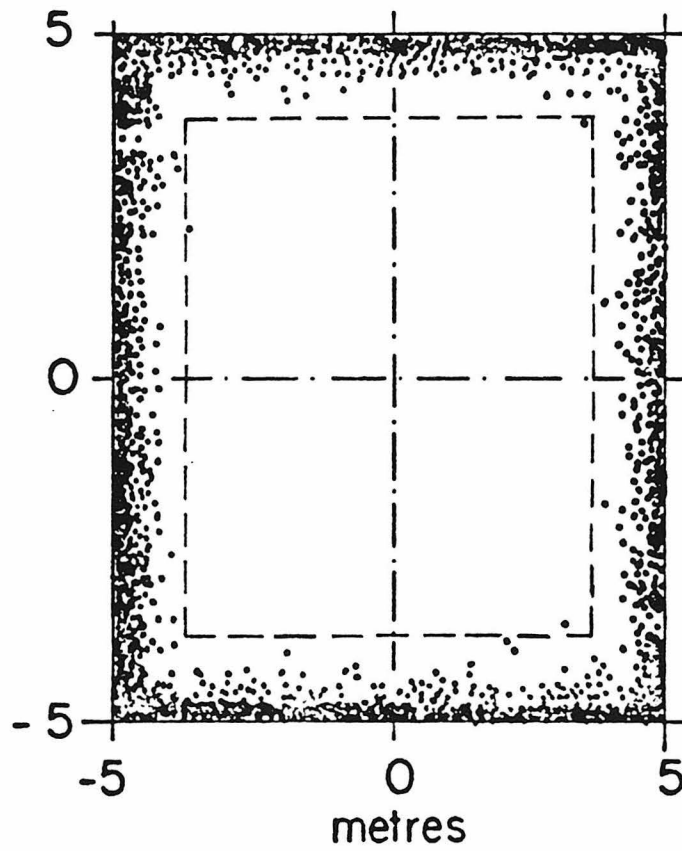


Figure 3-9. Distribution of interactions from entering neutrons in a $10\text{ m} \times 10\text{ m}$ detector of twice our density, taken from Grant.⁶¹ The dashed line denotes the equivalent to our fiducial volume cut.

trino interactions is essentially depth independent, and inescapable. In fact the criterion determining the minimum depth of a viable experiment, is that all other backgrounds be negligible in comparison to those caused by atmospheric neutrinos. In this subsection, we will discuss some of the qualitative features of neutrino interactions.

The total neutrino interaction rate, with visible energies $> 50 \text{ MeV}$, is estimated to be approximately 1 day^{-1} for our detector at its latitude of 52° . The flux varies slightly with latitude because of geomagnetic effects on the cosmic ray primaries. If we were to take *every* contained event to be a candidate for proton decay, then we would only be sensitive to proton lifetimes $\tau < 3 \times 10^{30}$ years, which is only slightly better than the Reines and Crouch limit (equation (3.1)). Also, since the fluxes are only believed to be known to 20% (section 6.4), a slight excess in the number of contained events could hardly be used as evidence for proton decay. By using the visible information from each event, as outlined below, we can reduce the background level for some decay modes by more than two orders of magnitude.

The neutrino spectrum basically follows the power law of the primaries, falling as $E^{-2.7}$ in the energy range appropriate to proton decay. Since the total neutrino cross-section rises linearly with energy, this implies a $E^{-1.7}$ dependence in the neutrino event rate. As a consequence of this, proton decays with higher visible energies, e.g., $p \rightarrow e^+ \pi^0$, have lower background rates. For the highest visible energy modes, the background can be reduced by an order of magnitude by imposing energy requirements.

Fortunately for us, the vast majority of neutrino interactions appear as single visible prongs, and so do not look remotely like proton decays. This class of events is dominated by quasi-elastic scattering which gives a single charged lepton track. Also, neutral current events with single pions, or charged current events with pions below Cherenkov threshold ($E_\pi < 212 \text{ MeV}$), appear as single tracks. Any nuclear fragments, with the possible exception of energetic protons ($E_p >$

1.43 GeV), would be invisible in a water Cherenkov detector.

It is the multi-prong events which may simulate proton decay. These may arise from charged current single- or multi-pion production, or neutral current multi-pion production. However, in order for an event to be considered as background, the net momentum of an event should be low, i.e., around the Fermi momentum in O^{16} , $p \sim 200 \text{ MeV}$ (see figure (2-2)). Since the neutrino interactions tend to have visible products thrown forwards in the lab frame, this constraint can reduce backgrounds by up to an order of magnitude (depending on the proton decay mode).

In order to estimate the background rate for each decay mode, it is necessary to simulate events in a Monte-Carlo program and apply the same selection criteria as is applied to the real data. The details and results of this procedure will be described in section 6.4 and Chapter 7.

4. The Detector

4.1 PERSPECTIVE

By August 1982, the IMB Collaboration (Appendix A) had completed the construction of an underground laboratory, and had started acquiring data in the search for proton decay using the world's largest detector. The detector was turned off in August 1984, having taken 417 livedays of data, so that it could be upgraded to increase light collection, and is scheduled to be in operation as the fully upgraded "IMB II" by 1986. For this thesis, we have analyzed the data from the detector before the upgrade.

The rationale for the design of our detector, and the basic principles of using it to search for proton decay, have been described in the preceding chapter. In this chapter, we will describe some of the details of the detector site, hardware, calibration, and operation—tracing the data acquisition chain from event to magnetic tape. In the following chapter, we will describe the converse: going from raw data to the reconstructed event.

The details of the detector have been described in great depth by previous thesis writers, in particular, by Cortez⁵⁵, Foster⁶², and Wuest⁶³ (1983), by Shumard⁶⁴ (1984), and by Park⁶⁵ (1985). Our description here is basically for the purpose of completeness.

4.2 OVERVIEW OF THE DETECTOR SYSTEMS

The detector, figure (4-1), is situated at the Morton-Thiokol salt mine, Fairport, Ohio, at a depth of 2000 ft, or 1570 m.w.e. There are four major systems operating at the detector site:

The Water System. The water serves both as a source of protons and as a radiating medium. The pool is of a rectangular volume with dimensions of 24 m ×

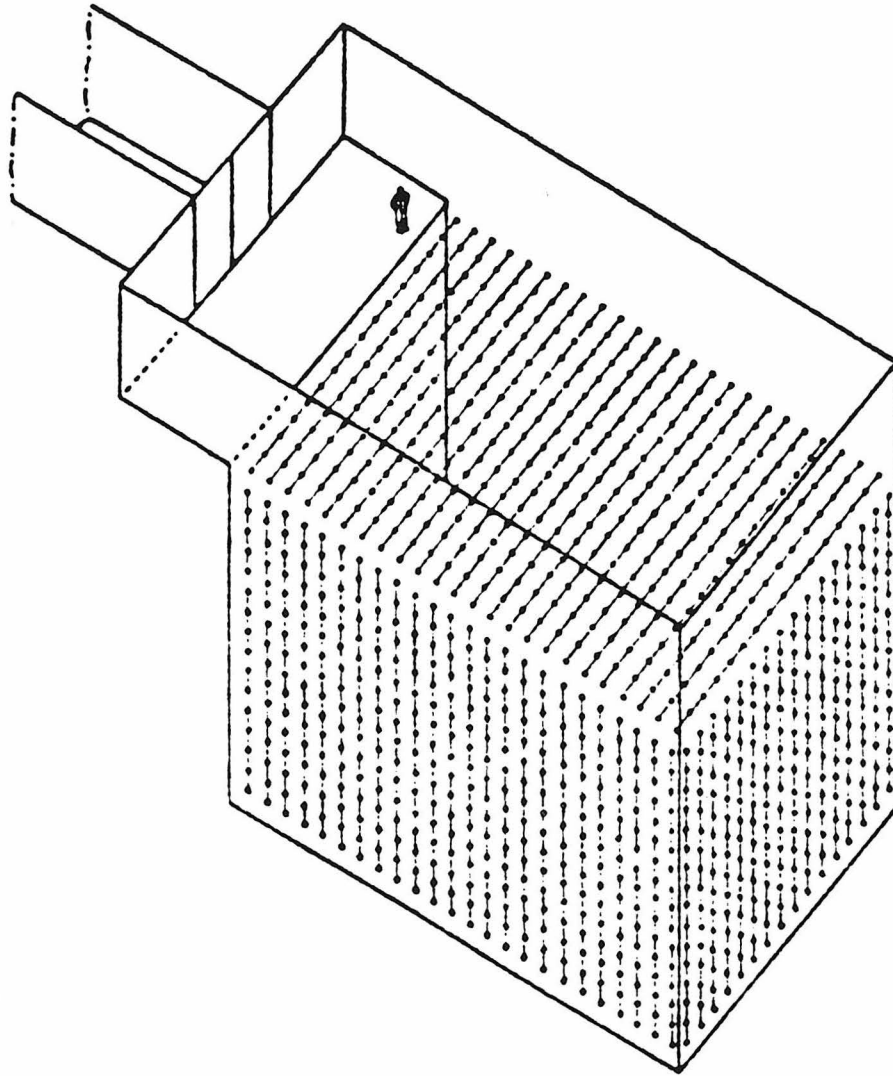


Figure 4-1. Schematic view of the I.M.B. detector, showing the P.M.T. surface array of ~ 1 meter lattice spacing.

18 m × 19 m in the East, North, and vertical directions, respectively. Its mass is approximately 8000 metric tons. The fiducial volume is situated about 2.5 meters in from the pool surface, and has software-defined dimensions of 18.8 m × 13.0 m × 13.5 m, and therefore contains 3300 metric tons of water, or 2.0×10^{33} nucleons. Of this water, 370 metric tons is in the form of hydrogen, giving us a source of 2.2×10^{32} free protons. The water is continuously purified by reverse osmosis techniques in order to keep the water as transparent as possible. The attenuation length has been measured in the pool, using the detector itself, and was found to be $\lambda_{\text{atten}} = 40 \pm 15$ m for 337 nm light.⁵⁵ This value was consistent with measurements using a spectrophotometer on samples of pool water, which are shown in figure (4-2).

Two black polyethylene liners provide the necessary seal between the pool and the surrounding rock. Their low reflectivity prevents the degrading of timing information from events.

The Data Acquisition System. The fiducial volume is viewed externally by 2048 P.M.T.'s, which are arranged on a rectangular surface array of $\simeq 1$ meter lattice spacing, at a distance of 2 meters from the fiducial volume, and about 50 cm from the pool surface. The typical light intensity of an event is at the single p.e. level.

We use 5 inch, hemispherical P.M.T.'s made by E.M.I. which have a timing resolution of $\sigma_t \simeq 5$ ns; this is roughly the size of the lattice spacing. The timing distribution, figure (4-3), is characterized by a long, non-Gaussian tail at later times, which requires attention during reconstruction. The angular response of the hemispherical P.M.T.'s has been measured *in situ*, using the calibration system,⁵⁵ and fits well to

$$A(\theta) = 1 + 0.75 \cos \theta. \quad (4.1)$$

The photocathode quantum efficiency as a function of wavelength, figure (4-4), was provided by the manufacturer,⁶⁶ the cut-off at 300 nm being due to the glass

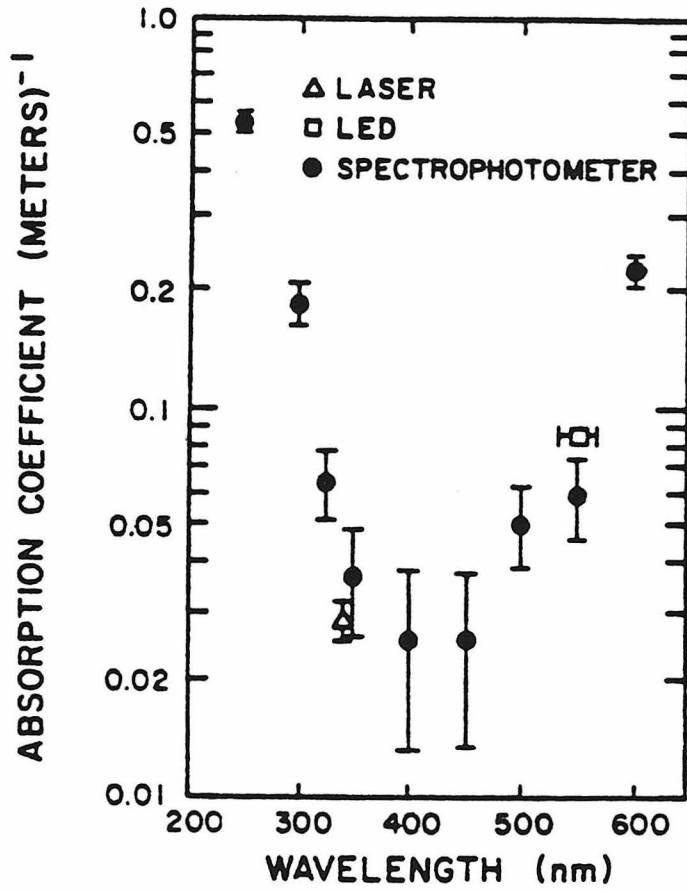


Figure 4-2. Measured attenuation in water vs. wavelength. The measurements shown were made with a spectrophotometer on a sample from the pool. Two of the measurements were made *in situ* using laser light (337 nm) and L.E.D. light (550 nm).

over the photocathode. It is nicely matched to the transmissivity of the water between 300–600 nm, figure (4-2).

The pulses from the P.M.T.'s are fed by cables to the electronics situated outside the pool, where the information from them is stored in analogue should the P.M.T. discriminator fire. The discriminator is set at a pulse height of 30 mV, which corresponds to a $\frac{1}{3}$ p.e. light level. The pulse information is digitized if the trigger conditions are met.

The trigger corresponds roughly to a 50 MeV visible energy threshold. Two types of concurrent triggers exist: the first requires 10 P.M.T.'s to fire in a 50 ns coincidence; the second is more complicated and involves the definition of a "patch." There are 32 patches in the detector, each consisting of an 8×8 array of P.M.T.'s. A patch discriminator is set to fire when three P.M.T.'s in the patch have fired within 50 ns. The second trigger saves an event if two patch discriminators have fired within a 150 ns coincidence. The noise rates are typically of the order of a few kHz per P.M.T., which results in an accidental trigger rate of $\simeq 1 \text{ min}^{-1}$. Both triggers are set at a level much lower than the analysis requirement that 40 P.M.T.'s fire in order for the event to be reconstructed.

The electronics digitize three 9-bit data points per tube:

- (a) The pulse height, otherwise known as "the uncalibrated Q ," allows for reconstruction of visible energy. Also, the on/off status of a tube provides, in correlation with other tubes, valuable topological information for event reconstruction and identification.
- (b) The time of arrival of the pulse, otherwise known as "the uncalibrated $T1$," allows for spatial reconstruction of events. The digitized time corresponds to about a 1 ns least count, which is much smaller than the P.M.T. resolution.
- (c) The time of arrival of a second pulse which arrives between 0.3–7.8 μs beyond the main trigger, otherwise known as "the uncalibrated $T2$," is dig-

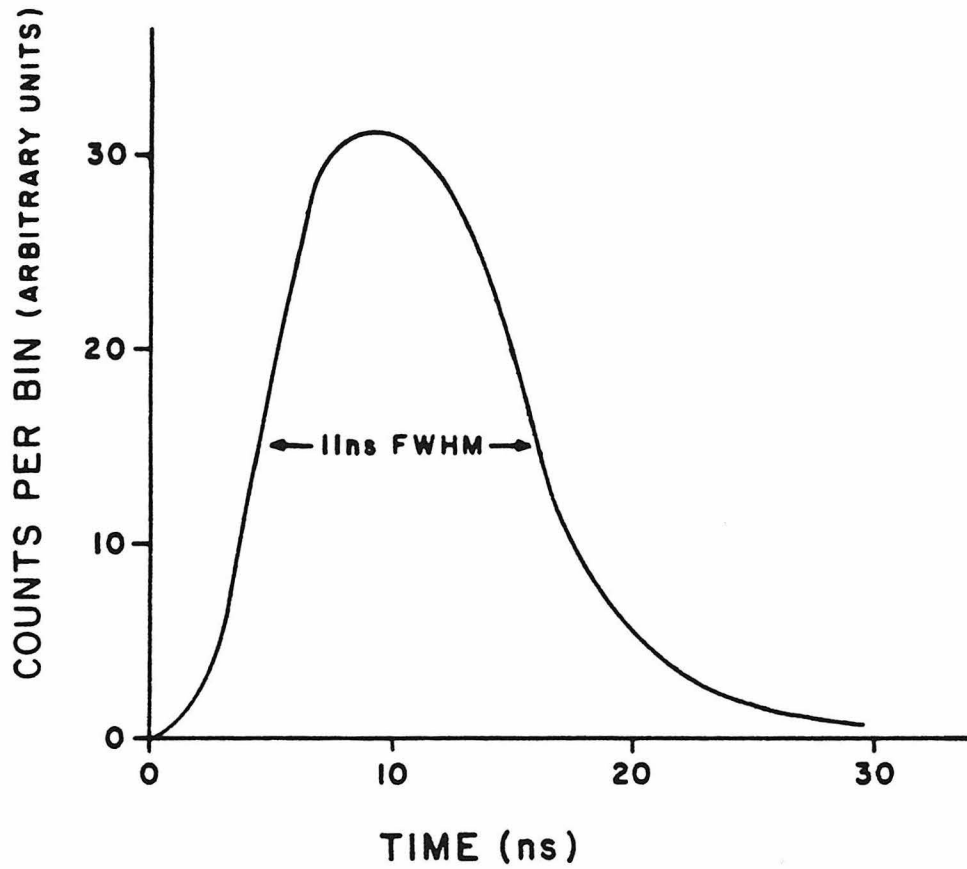


Figure 4-3. Typical timing distribution of a P.M.T. at the single p.e. level. The non-Gaussian nature at late times must be accounted for during event reconstructions.

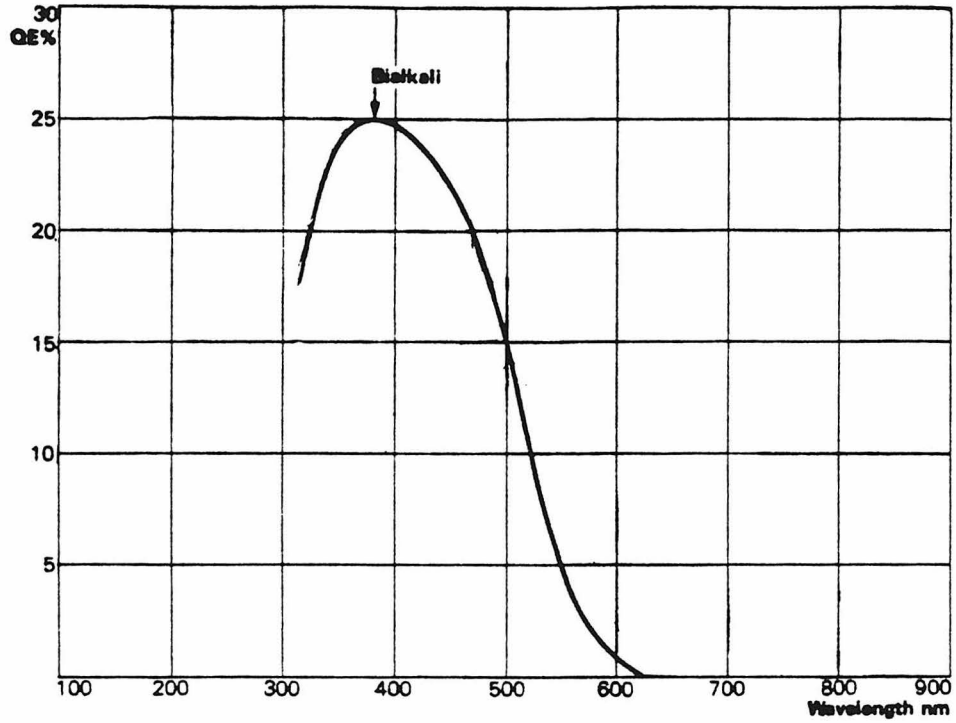


Figure 4-4. Photocathode quantum efficiency vs. wavelength. Note that this is well matched to the attenuation curve in Figure 4-2.

itized to a 15 ns least count. This allows for the detection of muon decay electrons after the main event.

The digitization and transfer of data to the data processing system takes 3 ms, and is the prime source of on-line dead time, which amounts to only 1%.⁶⁴

The On-Line Data Processing System. Following digitization, the data from an event are stored in one of 6 buffer memories to await processing. The processing takes 150 ms, so with a mean trigger rate of 2.7 s^{-1} , the dead time due to a buffer overflow is negligible ($< 0.2\%$ ⁶⁴). During processing, several very simple on-line algorithms are performed before the data and the algorithm results are stored on magnetic tape for off-line analysis. These algorithms include various uncalibrated statistics which are used for on-line monitoring purposes, and, in some cases, as input to fast off-line analysis algorithms.

The detector usually has two modes of recording data on tape. In the first mode, every trigger is recorded on an "uncut tape." In the more usual mode, only events with less than 300 firing P.M.T.'s (as calculated by one of the on-line algorithms) are recorded. The purpose of this is to save both the off-line analysis time, and more than a factor of three in magnetic tape. A cut tape fills up in 17 hours, as compared to 5 hours for an uncut tape. Since we have three tape drives, this means we can run the detector for 51 hours entirely unattended. Since even the most energetic proton decays would fire 180 P.M.T.'s, the inefficiency of this cut is entirely negligible. This cut corresponds to a visible energy at around 1600 MeV.

The Calibration System. The detector response is calibrated using nanosecond pulses of light of known relative intensities, and at known relative times. This is achieved by using the following hardware:

- (a) A nitrogen laser provides pulses of light at a 337 nm wavelength.⁶⁵
- (b) An ultraviolet photo-diode in the laser is used to monitor the laser firing time and variations in pulse intensity.

- (c) The pulse is passed through neutral density filters of known attenuation, ranging from 1.5 to 10^5 .
- (d) The light is then transmitted to the pool through an optical fiber.
- (e) At the end of the optical fiber is a 50 ml glass flask filled with a diffusing liquid (the “diffusing ball”). The liquid, DuPont’s “Ludox,” is a colloidal solution containing particles of size 20 nm, which scatters the light before it radiates from the diffusing ball. The intensity distribution, $I(\theta_{\text{ball}})$, has been measured, and is nearly isotropic.⁵⁵ The ball is placed in a known position in the tank, so that the relative time of arrival, and relative intensity of the light at the tubes can be calculated.

Setting the absolute energy scale is provided by studying samples of through-going muons. In section 4.3, we will discuss how calibration data is actually taken and used.

4.3 CALIBRATIONS

The Goals. The following quantities require calibration for each tube, i , before an analysis of the data can be performed (lower case symbols denote calibrated quantities):

- (a) the P.M.T. position, \vec{x}_i ;
- (b) the P.M.T. orientation, $\hat{\theta}_i$;
- (c) the P.M.T. light level, $q_i(Q_i)$;
- (d) the two P.M.T. firing times, $t_{1i}(T1_i, Q_i)$, and $t_{2i}(T2_i)$.

We note that all the above quantities are event independent, which is to say that they are independent of data from other tubes.

For a given calibrated event (defined as the set of the above calibrated data, from all tubes, for the same trigger), we use reconstruction methods to convert these data into the following event dependent quantities (denoted by primes),

which relate to the radiating tracks, j , and are, in principle, functions of *all* the data:

- (a) the track vertices, $(t'_0, \vec{x}'_0)_j$;
- (b) the track directions, \hat{x}'_j ;
- (c) the track visible energy, q'_j ;
- (d) the track particle type.

The reconstruction methods will be discussed in chapters 5 and 7. We will now discuss the calibration procedures.

Positions, \vec{x}_i . The tubes have been surveyed and their positions are believed to be known to within much better than a lattice spacing. There has been no evidence—either from photographs of the pool, or from response to real data—to suggest any significant systematic effects due to tubes deviating from their expected positions. The positions are recorded in a Cartesian coordinates, with the origin defined to be at the center of the fiducial volume. The tube planes are believed to be known to within a tube radius (< 6 cm). The measured values of the tube planes are: $x = \pm 940$ cm, $y = \pm 648$ cm, $z = \pm 676$ cm.

Orientations, $\hat{\theta}_i$. The tubes are orientated in the detector so that they point inwards, and normal to the tube planes. Since the tube response is only a slowly varying function of incident angle (equation (4.1)), the orientations are taken to be in the $\pm x$, $\pm y$, $\pm z$ directions of the respective planes.

The $T1$ scale. The $T1$ data are 9-bit numbers of roughly 1 ns least count, and thus cover a window of approximately 511 ns. In real data taking, the trigger is delayed such that the event occurs around the center of the scale. The scale is calibrated by placing the diffusing ball at a known position in the pool, and firing the laser at known times. Two modes of operation are used when taking calibration data:

- (a) “Ramped trigger mode.” During calibration data taking, the trigger is not set by the algorithm used for real data (section 4.1), but is set to fire at predefined times relative to the laser firing time. In the ramped trigger mode, the trigger is successively delayed by 40 ns so that the complete $T1$ scale is mapped out. We determined the scale to be non-linear to 3 counts $(100 \text{ ns})^{-1}$, which corresponds to a systematic error of $\simeq \pm 1 \text{ ns}$ across an event. Since this was negligible, a linear fit of counts to real time was performed for every tube:

$$T1_i = A_i t_{1i} + B_i(Q_i). \quad (4.2)$$

The slope, A , was found to be independent of light level, but the offset, B , needed calibrating as a function of pulse height, Q . This light level dependence arises from two main factors:

- (1) The P.M.T. pulse has a rise time of $\sim 10 \text{ ns}$, which is pulse height dependent, and consequently, the discriminator firing time is a function of pulse height.
- (2) The first photon to arrive at the photocathode is most likely to initiate the P.M.T. pulse (with a probability $\sim 10\%$). Therefore, the mean firing time becomes earlier as the number of incident photons (and, therefore, p.e.’s) increases.

Both these effects tend to make a tube fire earlier for higher light levels. Prepulsing effects are irrelevant at the 1 p.e. light levels of proton decays in our detector, and only become important at the 200 p.e. level.⁶³

- (b) “Fixed trigger mode.” During fixed trigger mode, the trigger is set to fire at a constant time from the laser firing, so that the count distributions lay around the center of the scale, thus imitating a real data trigger. Attenuating neutral density filters were used to vary the light level, and the offset was calibrated as a function of the pulse height by using a simple cubic fit.

The $T2$ scale. The $T2$ data are 9-bit numbers of roughly 15 ns least count, and thus cover a $7.5\mu\text{s}$ window, which commences immediately after the $T1$ scale. Since the scale is so coarse, a calibration of $T2$ as a function of light level is not necessary. Only ramped triggers are used for the calibration of $T2$ with time, and, similarly to the $T1$ scale, a linear fit is made to the calibration data, and the slope and offset are found for individual tubes. The $T2$ is used for the detection of muon decays after the main event. A muon decay signal is defined to be 5 firing P.M.T.'s in a 60 ns coincidence. The detection efficiency for μ^- and μ^+ have been measured at 55% and 65%, respectively. The details of the muon decay detection efficiency may be found in ref. 64.

The Q scale. The Q data are 9-bit numbers, and the scale is approximately linear at low light levels (< 5 p.e.'s), with a least count of about 0.1 p.e. The scale becomes increasingly non-linear with higher light levels.

Due to the Poisson statistics associated with the production of p.e.'s, the collection efficiency, and the production of secondary electrons at the first dynode, we have the situation where the Q distribution at a set light level has a width of the same order as the mean. A single p.e. has a mean pulse height of 70 mV, and a tube is defined to have "fired" if the pulse height exceeds the discriminator threshold of 30 mV.

The purpose of the calibration is to convert a given pulse height, Q , into a quantity proportional to the light level, q . In the next subsection, we will explain how q is converted to visible energy. Calibration data is taken at different light levels, using filters of known transmissivity. Using the transmissivity, T , the intensity distribution of the diffusing ball, $I(\theta_{\text{ball}})$, the distance, r , from the ball to the P.M.T., the attenuation length of the water, $\lambda_{\text{atten}}(300\text{ nm}) = 40\text{ m}$, and the P.M.T. angular response, $A(\theta_{\text{ball}})$, the relative light level was calculated at each P.M.T.,⁵⁵

$$q = T I(\theta_{\text{ball}}) \frac{e^{-r/\lambda_{\text{atten}}}}{r^2} A(\theta). \quad (4.3)$$

We then fit this to the mean digitized pulse height above threshold,

$$q = f(\bar{Q} - Q_{\min}), \quad (4.4)$$

where, in calculating \bar{Q} , values of $Q = Q_{\min}$ are used when the tube does not fire. The function, f , is chosen as follows:

$$q_i = \begin{cases} C_i(\bar{Q}_i - Q_{\min i}), & \text{if } (\bar{Q}_i - Q_{\min i}) \leq 65; \\ C_i(\bar{Q}_i - Q_{\min i}) + D_i(\bar{Q}_i - Q_{\min i} - 65)^2 & \text{if } (\bar{Q}_i - Q_{\min i}) > 65. \end{cases} \quad (4.5)$$

Fitting for C_i , and D_i , we can now convert the pulse heights, Q , into relative light levels, q_i , for real data events. Using the above procedure, we can find the relative light level at all the tubes that fired for a real data event. The absolute light level, of course, is still not known, and must be calibrated with a standard light source of a known visible energy. This is the topic of the next subsection.

Visible Energy. For a definition of visible energy, see equation (3.19). We calculate the visible energy of an event using the the approximation that all the light radiates from a vertex (which is assumed to be common to all visible tracks in the event). This is a exact approximation in the limit of low visible energies due to the short tracks, and is valid to within the systematic errors associated with the visible energy calibration for the visible energies appropriate to proton decay, $E_c < 1 \text{ GeV}$.

To put this approximation in perspective, we shall see in chapter 6 that the vertex resolution of our reconstruction programs is of the same order as the visible track lengths at low energy, $\sigma_r = 1.0 \pm 0.5 \text{ m}$, so correcting for the track lengths becomes almost meaningless.

The visible energy of an event can be expressed as the sum of individual

contributions from the tubes,

$$\begin{aligned}
 E_c &= \sum_{i=1}^{2048} e_i \\
 &= k \sum_{i=1}^{2048} \left(\frac{\alpha_i(\theta_i)}{\Lambda(r_i) A(\theta_i)} \right) q_i,
 \end{aligned} \tag{4.6}$$

where the "tube energy," e_i , contains the following factors:

- (a) q_i , the calibrated light intensity at the tube;
- (b) $\Lambda(r_i)$, a function describing the attenuation of light with distance;
- (c) $\alpha_i(\theta_i)$, the effective lattice area of the tube normal to the light, taken to be $\alpha_i = \cos \theta / \rho_{\text{wall}}$, where θ is angle of incidence, and ρ_{wall} is the number of tubes per unit area for the wall containing the tube;
- (d) $A(\theta)$, the angular response of the tube (equation (4.1));
- (e) k , a global constant to convert the units into MeV of visible energy.

To find k , we use the above formula find the visible energy (up to the constant k) of through-going muons which pass vertically near the center of the detector. For the attenuation function, $\Lambda(r_i)$, the dependence of light level, q_i , versus distance to the radiating point, r_i , was measured using the same muon sample, using the fact that light from the vertical muons strikes all the P.M.T.'s on the bottom of the pool at the same angle of incidence.⁵⁵ A plot, using all the bottom tubes, of q/r versus r then gives the appropriate function for Cherenkov light, and takes into account the subtle effects of light scattering both into and out of a Cherenkov cone. The resulting curve is consistent with an attenuation length of 32 m.

The absolute value of the visible energy which should be seen by these selected muons can be determined using a Monte-Carlo simulation of the detector, and using this value we solve for the calibration constant, k . The muons themselves have a well defined radiating track length (because $\beta = 1$) of 18.5 m above the

bottom tube plane, but since they have a mean energy of about 200 GeV, it is necessary to “dress” the muon with its electromagnetic interactions in the water and in the rock immediately above the pool, including delta-ray electrons, bremsstrahlung, and pair production. These processes increase the most probable radiating track length by 22%.⁶² From our studies of the relationship between visible energy (defined for *showers*) and radiating track length, equation (3.19), we conclude that the muons most probably deposit a visible energy of $E_c = (1.22 \times 18.5) \times 218 \text{ MeV} = 4.9 \text{ GeV}$. A comparison of this with the real data gives us the calibration constant, k .

5. The Data Reduction

5.1 PHILOSOPHY.

The purpose of the data reduction process is twofold:

- (a) to save any "contained" events, which originated inside the fiducial volume;
- (b) to reject any tracks which entered the fiducial volume. The key to a successful data reduction is to maximize the efficiency for (a), with the constraint that the contamination from (b) must be negligible.

In the context of a search for proton decay, the reason for saving *all* the contained events is to enable us to check the performance of the detector with interactions which can be understood. The proton decay signal would then present itself in deviations from the expected characteristics of the contained sample.

In section 3.3, we discussed in detail the kind of events expected to occur in our detector, and concluded that events (a) are predominantly atmospheric neutrino interactions at a rate of about 1 day^{-1} , plus possible proton decays at an unknown rate. Events (b) are predominantly entering muons at a rate of 2.7 s^{-1} , which, as we have pointed out, have distinct signatures, and should be easy to reject if we use the concept of the fiducial volume. We define the fiducial volume as being bounded by the rectangular surfaces at 2 meters inside the P.M.T. planes.

5.2 OBTAINING THE DATA SAMPLE.

History. The I.M.B. Collaboration had, at the time of this analysis, two independent analysis chains dedicated to rejecting entering tracks, and saving contained events:

- (a) The "West Coast Analysis" was developed at Caltech and U.C. Irvine. The analysis, consisting of three main sections, are briefly described as follows,

- 1) A upper cut at 300 P.M.T.'s rejects most through-going muons, and a lower cut of 35 P.M.T.'s rejects low energy noise, and events which cannot be adequately reconstructed. Geometrical cuts are made to quickly reject obvious entering muons.
 - 2) The event vertices are then fit under the point source approximation using only the timing information from the P.M.T.'s (a "point-fit") and are saved if reconstructed in the fiducial volume.
 - 3) Remaining events are then fit to a track source hypothesis, using both timing and topological information (a "track-fit"), and are rejected if the starting point of the track is reconstructed outside the fiducial volume.
- (b) The "Michigan Analysis" was developed at the University of Michigan and, briefly, it consists of the following sections:
- 1) A requirement of 40-300 P.M.T.'s is imposed for the same reasons as given for the West Coast Analysis.
 - 2) The best point-fit is found by searching over a discrete 1 meter lattice within the detector (a "lattice point-fit"). Events are rejected if the best lattice point is outside the fiducial volume.
 - 3) The wall of the detector is scanned by the program, and if a point is found which is a good hypothesis for an entry point of a track, the event is rejected.
 - 4) A track-fit removes events with the vertex of the track reconstructed outside the fiducial volume.

In both analyses, the vertex of the event is finally decided by either the track-fit for events with a single track geometry, or a point-fit for events with a multi-track topology, or an interpolation between these two vertices. This vertex is termed the "decide-vertex."

The vertex resolution is actually a function of the event topology. Two methods which have been used for estimating the resolution are as follows:

- (a) The use of Monte-Carlo simulations of neutrino interactions and proton decays in the detector (chapter 6). This tests the ability of the programs to analyze (simulated) Cherenkov light from tracks.
- (b) The use of the diffusing ball (section 4.2) at a known position in the pool, either as an isotropic point source, or with a shadowing structure to create short, Cherenkov-type rings. This method is a compliment to (a), since it measures the ability of the programs to analyze data directly from the detector electronics, though with no track sources.

The two methods agree very well, giving mean vertex errors of the order 0.5 m for isotropic, or two-body, back-to-back events, and 1 m for single track events. Of course, both methods have their own drawbacks. Perhaps the best indicator of our resolution is the fact that the independent vertices from the West Coast and Michigan Analysis have a mean difference of 1.3 m. This sample consists 84% of single tracks—see section 7.2.

For those who are interested, the details of the data reduction programs have already been extensively documented by previous thesis writers.^{55,62–65}

The “Official” Data Sample. The “official” data sample for publications by the collaboration consists of a combination of the sample of contained events found by either analysis chain. The official vertex is simply the vector mean of the two found vertices. Other attributes, e.g., A_c , of each event are also taken in the mean, as measured from the mean vertex.

This sample also includes a few higher energy, contained events, which were saved by another analysis chain, and used to investigate $n-\bar{n}$ oscillations.⁶⁶

In total, the official data sample from “IMB I” consists of 401 events collected in 417 days of livetime.

The Thesis Data Sample. The data sample we chose to analyze for this thesis is the subset of the official data sample whose decide-vertex, as found by analysis

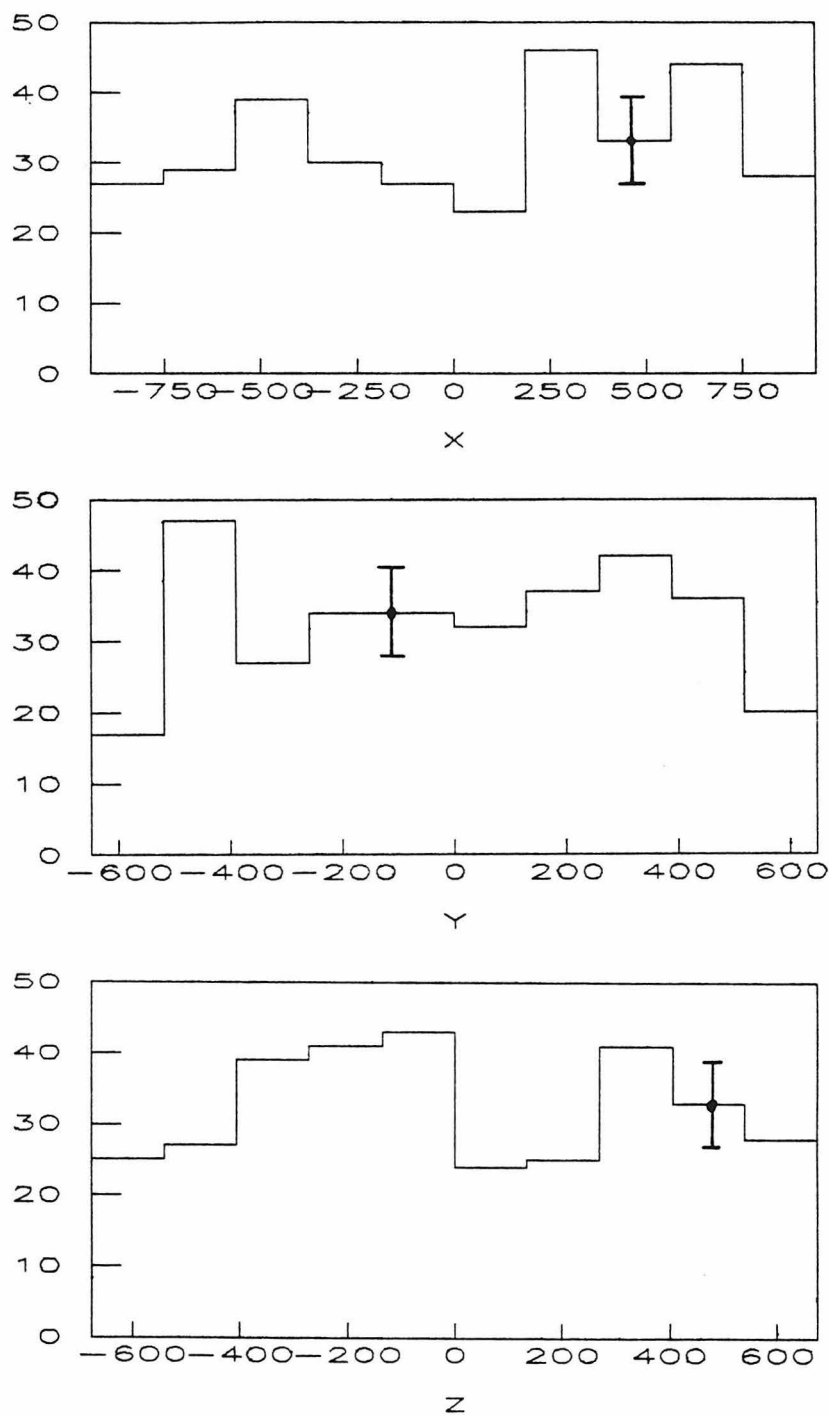


Figure 5-1. Vertex distribution of 326 events in the X, Y, and Z directions. There is no excess of events near the fiducial boundary.

chain (b), fits inside the fiducial volume. One analysis chain was chosen for reasons of simplicity and consistency. The data, the background simulations, and the proton decay simulations, were all passed in the same way through the data reduction chain.

The thesis data sample, which will be analyzed for the proton decay search in chapter 7, consists of 326 events taken in 417 days of livetime.

5.3 CHECKS FOR CONTAMINATION.

Introduction In section 3.3, we argued that the only kind events we should see in our final data sample are (i) atmospheric neutrino interactions, and (ii) events originating in the detector from “new physics,” e.g., proton decay. Before we search for a proton decay signal, it is necessary to make some preliminary checks on the data sample in order to establish whether any entering contamination is negligible. We suggested the following systematic checks on the data sample:

- (a) The homogeneity of the vertex distribution in the detector. Entering contamination would show up as an enhancement of vertices near the boundary of the fiducial volume, particularly near the top or sides of the detector.
- (b) The isotropy of the energy direction distribution. In particular, an excess of downward going events with vertices near the boundary of the fiducial volume at the top and the sides of the detector, would be evidence for entering contamination.

The Vertex Distribution. In figure (5–1), we show histograms of the reconstructed vertices of the sample in the X, Y, and Z directions. The distributions are consistent with being homogeneous. The number of events per unit volume within one meter of the fiducial volume is consistent with the rest of the sample.

The Energy Direction Distribution. We define the “energy direction” of an event as the direction of the vector sum of the energy-weighted directions from

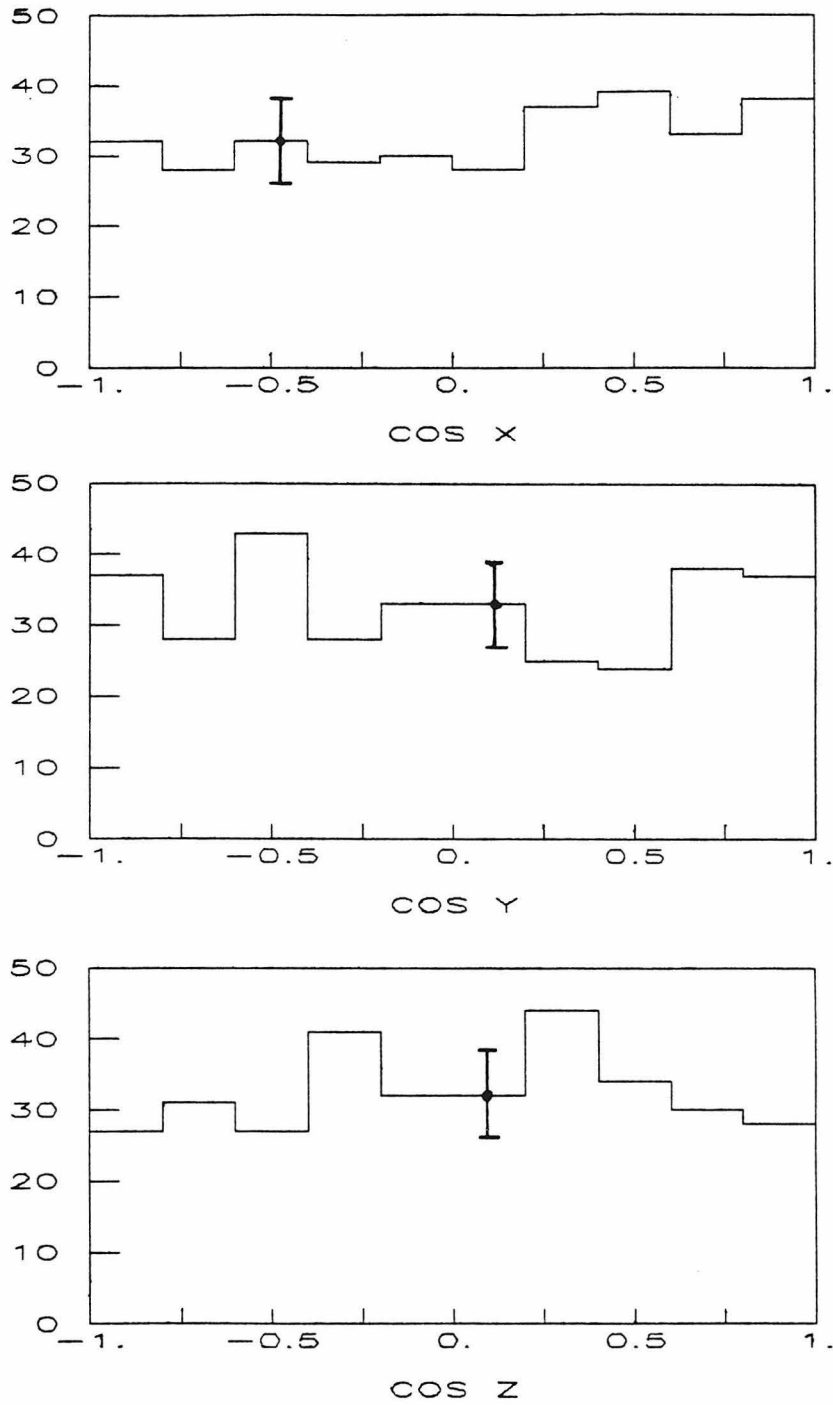


Figure 5-2. Direction cosine distribution of 326 events in the X, Y, and Z directions. There is no excess of downward going events.

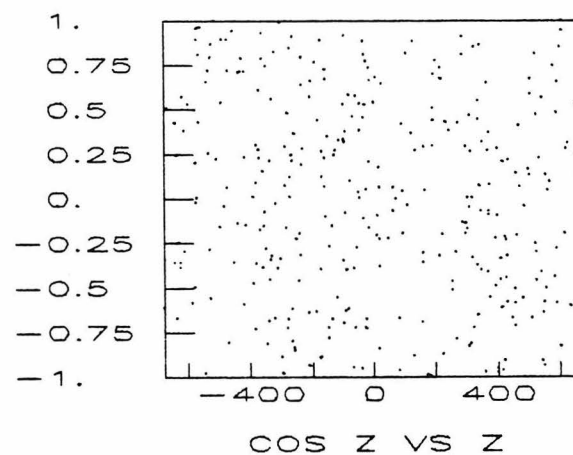
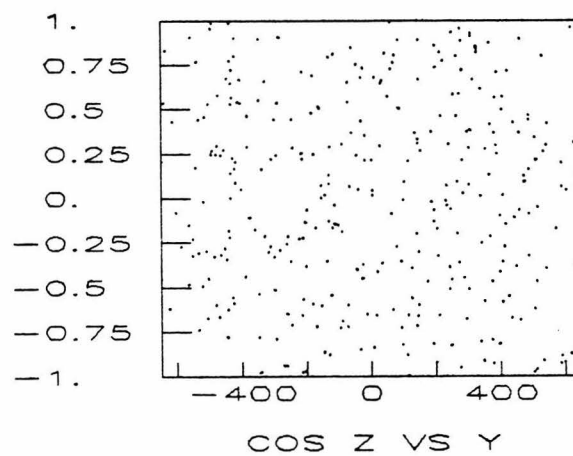
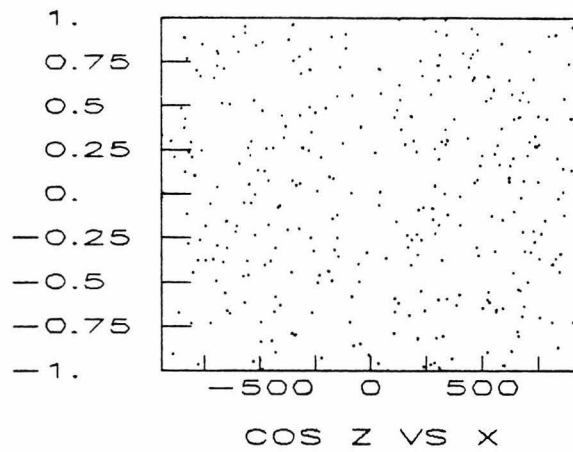


Figure 5-3. Z-direction cosine vs. vertex position for 326 events in the X, Y, and Z directions. There is no excess of downward going events near the fiducial boundary.

the event vertex to the firing P.M.T.'s (c.f. equations(7.3) and (B.3)). Basically, it is the direction of the visible momentum of an event. In figure (5-2), we show histograms of the direction cosines of the sample in the X, Y, and Z directions. In figure (5-3), we show scatter plots of the Z direction cosines with the vertex positions in the X, Y and Z directions. There is no significant enhancement of events which are close to boundary of the fiducial volume and moving downwards.

5.4 CONCLUSIONS.

The rate of events for this analysis is $0.78 \pm 0.04 \text{ day}^{-1}$, which appears to be consistent with the expected rate for neutrino interactions, at $1.0 \pm 0.2 \text{ day}^{-1}$ (section 6.4). We conclude that the data sample is indeed free of entering contamination. The sample is consistent with events which have originated within the detector.

The characteristics of individual events will be analyzed in chapter 7, but first, we must understand what to expect from atmospheric neutrino interactions, and from a possible proton decay signal. To do this quantitatively, we prepared samples of simulated events. We shall explain how we did this in the next chapter.

6. Simulations

6.1 INTRODUCTION

A good Monte-Carlo simulation of events is necessary to study the data quantitatively. In this chapter, we describe some of the physics and the algorithms we have used to create both simulated data of events which we should expect to see (i.e., the atmospheric neutrino interactions), and of the proton decay events which we are searching for.

There were originally three independent Monte-Carlo programs in use by the I.M.B. collaboration, the output from which have been cross-checked and found to be in substantial agreement.

The program, upon which we have based our simulations, was written by B. G. Cortez⁵⁵ and G. W. Foster⁶², with the nuclear interactions of mesons included by work from T. W. Jones,^{66,67} D. W. Kielczewska,⁶⁸ and E. Shumard.⁶⁴ See Appendix A: The IMB Collaboration.

The code we have added includes the generation of proton decays, the tracking of decay products through the nucleus, and in particular, the ρ resonance mass distribution, which, as we shall discuss, is a function of the decay mode under consideration because of the available phase-space.

The signal simulation was a monumental computational task, involving the generation and analysis of 39,000 events from 78 separate simulation files, and using over 400 hours of c.p.u. time on a VAX/780. The background simulation involved the processing of over 25,000 neutrino and anti-neutrino events from 3 of the world's bubble chambers.

In the next section, we shall give a description of the sections of the Monte-Carlo which are common to all the simulations.

6.2 GENERAL MONTE CARLO FEATURES

Propagation and Interaction in Water. Particles are propagated through the water in 0.5 cm steps. During the propagation, if the particle is charged, then Cherenkov photons are generated according to the β of the track (as described in the next subsection). At the end of the step, the loss in particle energy is calculated according to published dE/dx tables.⁵³ The dice are then thrown, and the outcome determines whether the particle interacts with the water, decays, or continues to the next step until it exits the detector or stops. If the particle has stopped, it is allowed to be invisibly absorbed (μ^- , π^-), or decay (μ^\pm , π^\pm), or do nothing (e^\pm , p^+ , n).

Most of the particle types are not actually propagated in the water, since their decay length is extremely small in comparison with both their interaction length and the scale of the event. This includes the π^0 , η , K_S^0 , ρ , ω and K^* , all of which either interact or decay in the parent nucleus, or decay to within the order of a centimeter of it.

The interactions, relevant for our analysis, basically come in two types:

- (a) Electromagnetic showering interactions of the e^\pm and γ . For this, we use the EGS Monte-Carlo code.⁵⁴ Also, for calculating the visible energy of through-going muons of mean total energy 200 GeV, (section 4.3), we include the effects of knock-ons, brehmasstrahlung, and pair production.⁶²
- (b) Strong interactions of the π^\pm and the \bar{K}^0 component of the K_L^0 with the hydrogen and oxygen nuclei. Interactions of the K^+ are suppressed due to its strangeness. Its interaction length in water is 18m, to be compared with its range of 10cm—consequently we assume that all K^+ 's decay.

The pions are allowed to interact either with the free protons of hydrogen, or the O^{16} nuclei. The cross-sections for the outcomes of πO^{16} and πH interactions in the simulations were derived from published data.⁷⁰⁻⁷⁵ The pions can either

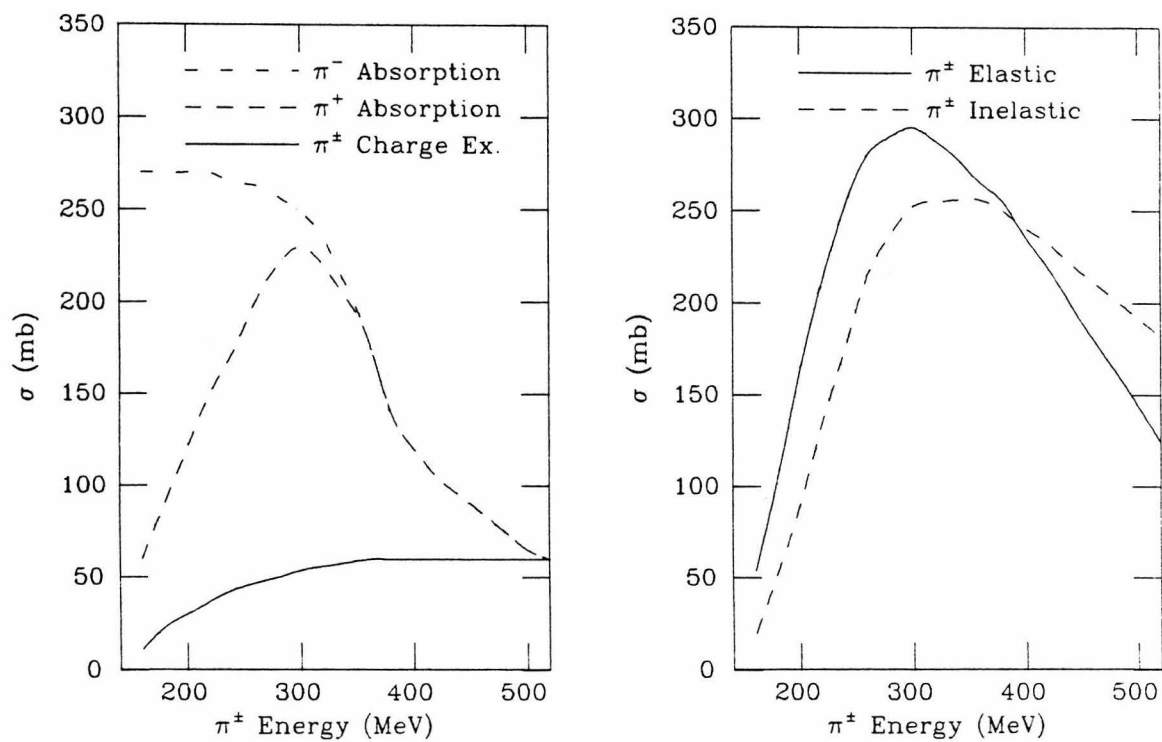


Figure 6-1. Cross-sections for πO^{16} , as used in the simulation. These curves are interpolations of various experimental measurements.⁷⁰⁻⁷⁵

scatter elastically, inelastically, charge exchange, or be absorbed. In figure (6-1), we show the πO^{16} cross-sections used in the simulation.

The scattering and absorption cross-sections peak for πO^{16} at about $\sigma \sim 300\text{mb}$ with $E_\pi \sim 300\text{MeV}$. Scattering effectively takes place off individual nucleons, for which final state momenta of nucleons below the Fermi energy ($\simeq 230\text{MeV}$) is suppressed ("Pauli blocking"). Consequently, the scattering is actually peaked backwards.

The charge exchange cross-section for πO^{16} rises and plateaus at $\sigma \sim 50\text{mb}$ with $E_\pi \sim 300\text{MeV}$. Charge exchange for the π^+ cannot, of course, take place on hydrogen.

Absorption is only allowed on nucleon pairs in O^{16} , however, to conserve four momentum. All π^+ 's which come to rest are allowed to decay, whereas all π^- 's are absorbed, and the subsequent nuclear breakup produces no Cherenkov light.

We note that π^0 's, either directly from proton decay, neutrino interactions, or charge exchange, decay effectively instantaneously, and we do not consider its interactions in water (though we do inside a nucleus for proton decay, section (6.3)). We shall discuss individual πN interactions in section 6.3.

We now consider the K^0 . Upon birth, the K_S^0 component of the K^0 dies out after a few centimeters at our energies in water. For this reason, the K^0 's are given a 50% probability of decaying immediately as a K_S^0 , or as a K_L^0 which propagates in the water. The K_L^0 is allowed to decay or interact. Also, the K_S^0 component is allowed to regenerate, caused by the preference of the water to interact with the \bar{K}^0 component. The total cross-section of $K_L^0\text{H}$ has been measured at 31 mb at the relevant K_L^0 momentum of 300 MeV. The total cross-section of 450 mb for $K_L^0\text{O}^{16}$ was determined⁶⁴ using an interpolation of published data for K_L^0 's in various materials. The partial cross-sections for $K_L^0\text{H}$ were determined using published data, isospin relations, and detailed balance. For $K_L^0\text{O}^{16}$, the results were scaled to agree with the total cross-section. The total

interaction length in water was found⁶⁴ to be 80 cm, to be compared with the long decay length of over 900 cm. This is, in a way, fortunate for two reasons:

- (a) If K_L^0 decays were significant, this would cause severe reconstruction problems, particularly since we make use of the point source approximation in the data reduction.
- (b) The short interaction length means that the same arguments we used to claim that entering neutrons were not a background problem, apply to K_L^0 's; see section 3.3.

Cherenkov Light Generation and Propagation. For a more detailed discussion on the physics of Cherenkov light generation, see section 3.2. The number of photons generated in a segment of track is given according to the formula (3.15). To save time, the wavelength of the photons are generated according to the P.M.T. quantum efficiency folded with the Cherenkov spectrum.

Each photon is assigned a random attenuation length, according to its wavelength; see figure (4-2). If the photon travels this distance before hitting a P.M.T. or the wall of the detector, it interacts according to the algorithm: (i) if $\lambda < 400$ nm, the photon scatters with a 90% probability, otherwise it is absorbed; (ii) all photons with $\lambda > 400$ nm are absorbed. The result is that, in total, about 20% of the photons scatter.

Actually, to speed up the generation of events, the number of generated photons has been decreased by a factor of nine, and, to compensate, the dimensions of the P.M.T.'s have been made larger by a factor of 3. This is obviously a valid approximation, considering that each enlarged tube still covers only 11% of its surrounding area.

The Detector. The simulated detector has dimensions of almost identical dimensions to the real one; see the second subsection of section 4.3. With the coordinate system at the center of the detector, the walls are at $x = \pm 1190$ cm, $y = \pm 890$ cm, $z = \pm 950$ cm, and for historical reasons, the tube planes are at

$x = \pm 943$ cm, $y = \pm 642$ cm, $z = \pm 692$ cm. The 2048 P.M.T.'s are positioned on a rectangular surface lattice, of a 1 meter spacing.

After the event data have been "taken," the P.M.T.'s which fire due to noise are simulated under the approximation that all P.M.T.'s fire randomly at a mean rate of 2.7 KHz. This is about the mean rate of random firing per P.M.T., corresponding to only about 3 P.M.T.'s firing by noise on the $T1$ scale.

The P.M.T. collection efficiency has been adjusted in the Monte-Carlo to 60%, in order to give good agreement between simulated and real muon data. The number of photons hitting the each P.M.T. is calculated according to the probability of collection, and the angular response (equation (4.1)).

The pulse height of the tubes is smeared by summing the contributions from each photoelectron. This is done by choosing a random value from the measured pulse height distribution at the single p.e. level.⁵⁵ The timing data from the tubes is then smeared using the first photon effect model⁵⁵ (see the discussion following equation (4.2)), and the measured P.M.T. time jitter at the single p.e. level (figure (4-3)).

The simulated data is then digitized in the precise form of the real data, to enable the analysis programs to read them both without "knowing" the difference—a simple precaution worth taking.

6.3 SIGNAL SIMULATION.

Overview of Monte-Carlo Files. In all, 78 files were generated for the various decays of protons and neutrons, including 28 files for the analysis of free proton decay. In all, 37 individual decay modes of the nucleon were simulated, 17 of which were also analyzed for free proton decay. For several of the modes, more than one Monte-Carlo file was generated to allow for the separate analysis of different branching modes of the daughter mesons.

In deciding the number of generated events required for determining the

efficiency for seeing the various decay modes, we considered the following:

- (a) Real proton decays could occur with equal probability, anywhere inside the pool and not just in the fiducial volume. Just generating events inside the fiducial volume would tend to underestimate efficiencies, because in reality, events either side of the boundary could get reconstructed either outside or inside. We decided to generate events randomly in the total volume. The ratio of the fiducial volume to the total volume is 0.416, which means that out of the total number generated, we can at best expect only 42% of them to be analyzed for a signal.
- (b) With foresight of the need to calculate lifetime limits, it is important that the square of fractional error (s.f.e.) in the efficiency be much less than the s.f.e. in the number of observed candidates. If we anticipate a number of candidates of N_c , the s.f.e. in this is $F_c = 1/N_c$. If we now impose the condition that the confidence of the lifetime limit be insensitive to an error in the efficiency, then we would desire an s.f.e. in the efficiency of the order $F_\epsilon < 0.1F_c$, and hence $N_\epsilon > 10N_c$, where N_ϵ is the final number of simulated events accepted as a signal. For example, if we anticipate the final number of candidates to be of the order 10, then we would need to accept at least 100 Monte-Carlo events in the analysis requirements. (Note that we are not considering an “error” in the lifetime limit, whatever that means, but an error in the lifetime *measurement*, which is precisely what a lifetime limit measures—the confusion on this point has been made in the past by various honorable people.)

Taking into account these considerations, the number of events generated in the total volume should be at least $10N_c/(0.416\epsilon_a)$, where ϵ_a is the total acceptance for Monte-Carlo events, normalized to the fiducial volume. For example, if we have 5 candidates, and an acceptance of 40%, then we would need at least 300 events generated in the total volume.

The actual files generated have at least 400 events, most have 500, and, when

required, some have 1000 or 1500 events.

In the following subsections, we will give some of the details of the physics behind the workings of the signal simulation program.

Decay Parameters.

- (a) For the case of files containing bound plus free protons, each event is given a 20% probability of being free, and thus with no net momentum.
- (b) The decay vertex, on the scale of the detector, is chosen homogeneously in the total volume (see item (a) in the last subsection). On the scale of the nucleus, the vertex for bound nucleon decay is chosen from the density distribution⁶⁹ in figure (6-2).
- (c) The free proton energy is taken to be 938 MeV; in the detector frame, the bound nucleon energy is taken to be 931 MeV to account for the binding energy (we are not implying that the difference is observable to us!) The center of mass decay energy is then given by equation (2.10), with the Fermi momentum subtracted in quadrature from 931 MeV.
- (d) Magnitude of the bound nucleon momentum is chosen under the approximation of the Fermi gas model. The direction of the momentum is isotropic.
- (e) The decay orientation is assumed to be isotropic in the frame of the decaying nucleon; the products are then Lorentz boosted into the frame of the detector (and nucleus).
- (f) Out of the 37 decay modes investigated, 33 of them are two-body decays, and as such, the only free parameter in the nucleon frame is the decay orientation (e). For the 4 three-body modes of the type $N \rightarrow \bar{\ell}\ell\bar{\ell}$, we made the simplest assumption of a flat phase space. Due to the properties of the variables used to analyze the data (Chapter 7, and Appendix B), the results are insensitive to this assumption, with the possible exception where one of the leptons is a neutrino.

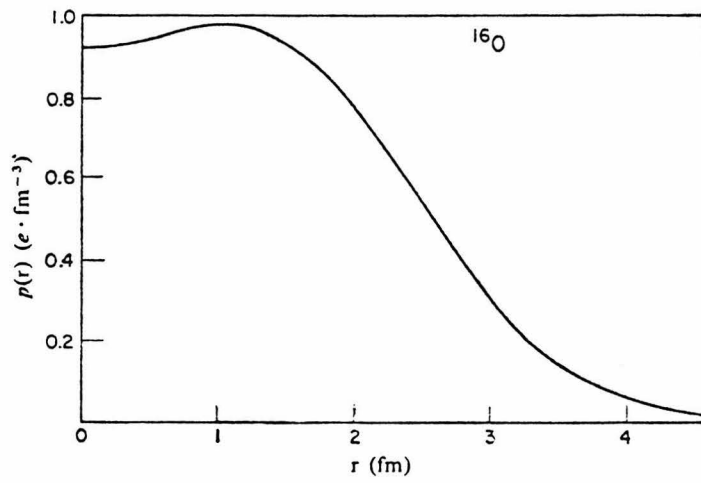


Figure 6-2. Density distribution of nucleons in O^{16} .

Rho Resonance Mass Distribution. The initial parameters of the decay products have now been all fixed, except for case of the meson resonances. The only resonance with a significant width, compared to our energy resolution, is the ρ , with a mass, $m_0 = 769\text{MeV}$, and full width, $\Gamma = 154\text{MeV}$ (the K^* is also of interest, because its mass is close to that of the nucleon.⁶⁴)

Since a significant fraction of the Breit-Wigner mass distribution is above the proton rest mass, it is necessary to account for how the shape of the ρ resonance needs to be modified. One can speculate in advance that if the ρ were accompanied by a μ , that the modifications may be quite substantial, which, as we shall show, is indeed the case.

The resonance shape is modified from the standard Breit-Wigner form, taking into account the following effects:

- (a) The phase-space of the $\pi\pi$ pair. This modifies the low energy tail of the distribution, causing a smooth cutoff at around 270 MeV. We assume that the ρ decay is pure P -wave.
- (b) The phase-space of the $\ell\rho$ from the nucleon decay. This modifies the high energy tail, causing a smooth cutoff at $(m_p - m_\ell)$.

Formally, we follow the arguments of Jackson.⁴² We must compare the rate of production of $\ell\rho(m)$ with that of $\ell\varrho(m)$, where ϱ is a fictitious ρ which is perfectly stable (see figure (6-3)), but has the same invariant mass as the ρ .

First, we take into account the effect of the $\ell\rho$ phase-space. The two-body phase space of the of the $\ell\varrho$ pair is proportional to q , the momentum of the ϱ (and, of course, the ℓ) in the nucleon rest frame, so we write the rate of production:

$$d\sigma_{\varrho}(m) = \frac{q_{\rho}(m)}{q_{\rho}(m_0)} d\sigma_{\varrho}(m_0), \quad (6.1)$$

where m is the invariant mass of the $\pi\pi$ pair, and we will let m_0 be the value of m at the peak of the pure Breit-Wigner distribution of the ρ ; m_0 is not, in general, the peak of the modified mass distribution.

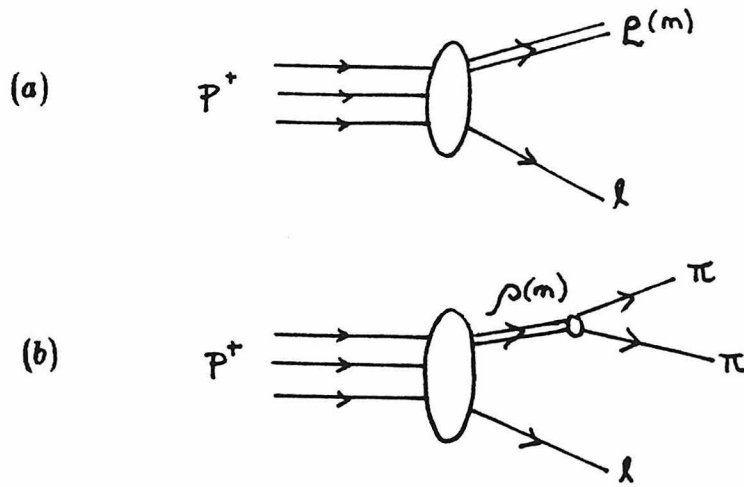


Figure 6-3. Phase-space considerations for ρ decay. We must consider (a) the ρ , which is a stable, fictitious ρ of equal invariant mass to (b) the $\pi\pi$ pair of the real ρ .

To relate the ρ to the ρ , we express the rate of $\ell\rho$ production at mass, m , as:

$$d\sigma_{\rho}(m) = d\sigma_{\rho}(m) \frac{1}{\pi} \left(\frac{m_0 m \Gamma(m)}{(m_0^2 - m^2)^2 - m_0^2 \Gamma^2(m)} \right) dm, \quad (6.2)$$

where, in order to account for the phase-space of the $\pi\pi$ pair, the "width," Γ , is a function of m , because it is proportional to the square of the matrix element integrated over the available $\pi\pi$ phase-space (a statement of Fermi's Golden Rule):

$$\Gamma(m) \propto \int |V|^2 \frac{q_{\pi}(m)}{m} d\Omega. \quad (6.3)$$

Since the ρ decay is P -wave, we must consider the dependence of the matrix element on, $q_{\pi}(m)$, the π momentum. Partial wave amplitudes of angular momentum l , go as $(qr)^l$ near the decay region, so, from equation (6.3), we expect:

$$\Gamma(m) = \Gamma(m_0) \left(\frac{q_{\pi}(m)}{q_{\pi}(m_0)} \right)^{2l+1} \frac{m_0}{m}. \quad (6.4)$$

For the case if the ρ , we substitute $l = 1$ in the above equation, and follow Jackson's⁴² suggestion of replacing the factor (m_0/m) in the above equation, with the empirical factor of $2q_\pi^2(m_0)/(q_\pi^2(m_0) + q_\pi^2(m))$.

The results of our calculations are shown in figure (6-4), which give the mass distributions for $\mu\rho$ and $e\rho$; alongside for comparison are the Breit-Wigner curve, and the effects separately including the $\pi\pi$ phase-space, and the $\ell\rho$ phase-space. We do not need to distinguish between distributions for $e\rho$ and $\nu\rho$.

The most noticeable effects on the resonance shape are as follows:

- (a) The mean of the distributions have been shifted from 770 MeV to 725 MeV for $e\rho$, and 706 MeV for $\mu\rho$.
- (b) The peak of the distributions have been slightly shifted from 770 MeV to 750 MeV.
- (c) The FWHM of the distributions have been narrowed slightly from 154 MeV, to 125 MeV.

We can deduce from these observations, that the biggest effect is the asymmetry of the distribution about the peak, caused by a depletion of ρ decays at high invariant mass.

Propagation and Interaction in the Nucleus. Leptonic decay products, and γ 's are allowed to exit the nucleus unscathed, and are immediately passed to the section of the code dealing with propagation in water. The mesons, however, can interact strongly with the nucleus in bound decays, and can in some cases decay inside the nucleus. At the energies of interest to us, it is a good approximation that the meson interact with individual nucleons (the exception being for absorption, discussed below).

For this purpose, we employ a cascade model inside the nucleus,⁶⁶ which, besides being able to naturally account for Pauli blocking, has the benefit of giving for each event, the number, types, and momenta of particles leaving the

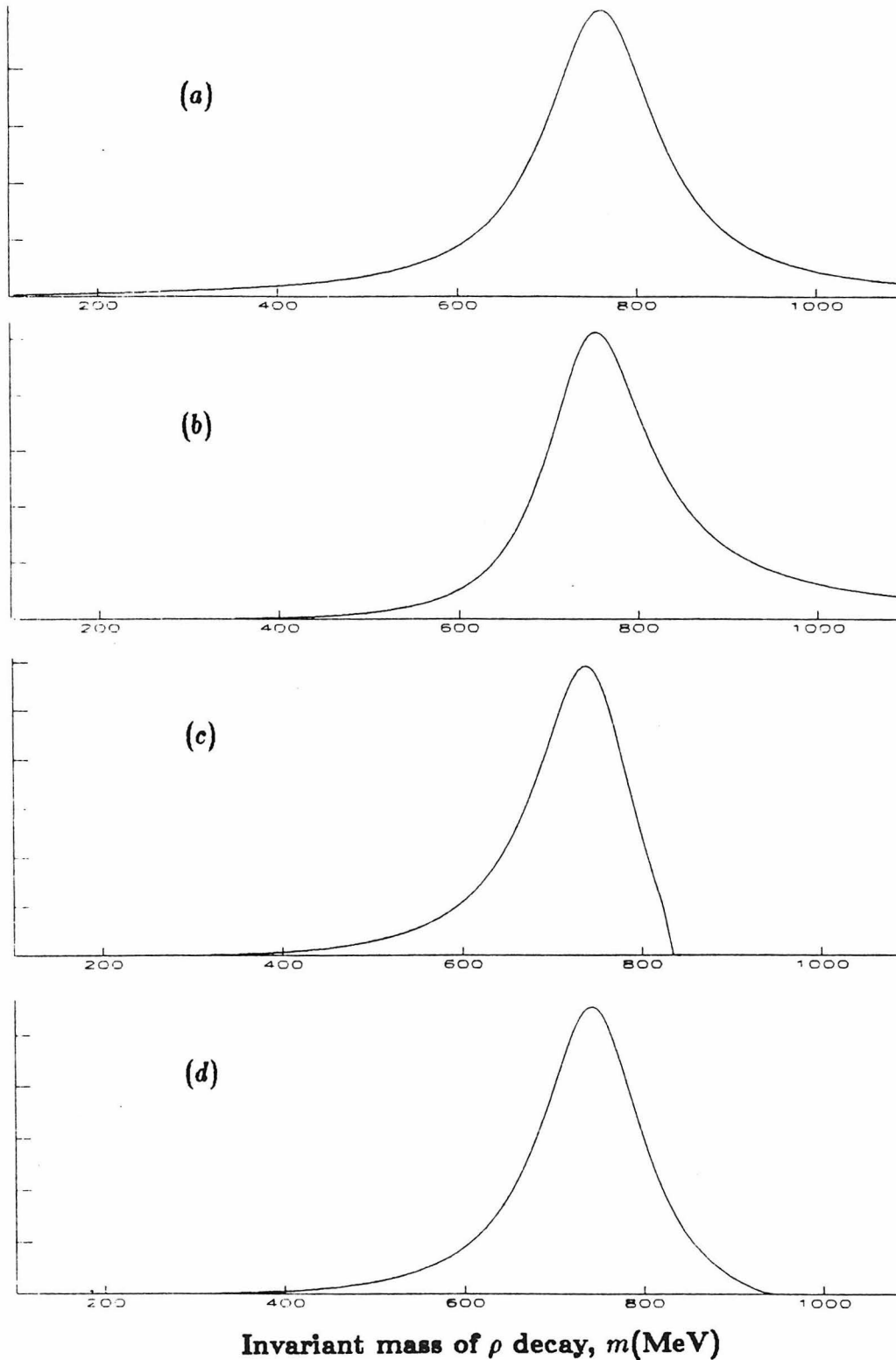


Figure 6-4. The shape of the ρ resonance in proton decay (a) the pure Breit-Wigner, (b) with $\pi\pi$ P -wave phase-space, (c) with $p \rightarrow \mu\rho$ phase-space, (d) with $p \rightarrow \nu/e\rho$ phase-space.

nucleus, after which they are allowed to propagate through the water. The mesons are followed through the nucleus in steps of 0.2 fm, and at each step are giving the chance to either decay or interact, until the meson is > 6 fm from the center of the nucleus.

Decays are straightforward—we use published branching ratios and lifetimes, and the products are then themselves tracked through the nucleus. The only particles which have a short enough lifetime to decay in the nucleus are the ρ , ω , and K^* .

The ω has a $c\tau = 20$ fm, but its velocity is small enough that it has a decay length $\lambda_\omega = c\tau\gamma\beta = 3$ fm, which is of the same order as the size of the O^{16} nucleus, with $\langle r \rangle = 2.75$ fm. Due to its low β , the K^* resonance has a decay length of about 0.75 fm. The ρ resonance is a special case—since it has such a large width, it decays effectively instantly at less than 0.2 fm from the proton decay vertex. Consequently, we assume that all ρ 's decay immediately following production.

Interactions are more difficult, since frequently the available data is either tenuous or non-existent. For the O^{16} nucleus itself, we use a published density distribution,⁶⁹ figure (6-4), and the Fermi gas model. The treatment of each of the mesons is as follows:

- (a) Pions. For elastic scattering and charge exchange, we take into account both the $I = \frac{1}{2}$ and the $I = \frac{3}{2}$ amplitudes by using published cross-sections⁷⁶ for $\pi^+p \rightarrow \pi^+p$, $\pi^-p \rightarrow \pi^-p$, and $\pi^-p \rightarrow \pi^0n$; then the other permutations are deduced by use of simple isospin relations, and detailed balance. We make the good approximation that the masses of the pions are equal, and the masses of the nucleons are equal. In figure (6-5), we show the mean πN cross-sections per nucleon as used in our program.

Absorption is believed to occur predominantly on nucleon pairs. The πD absorption cross-section has a slightly different energy dependence than

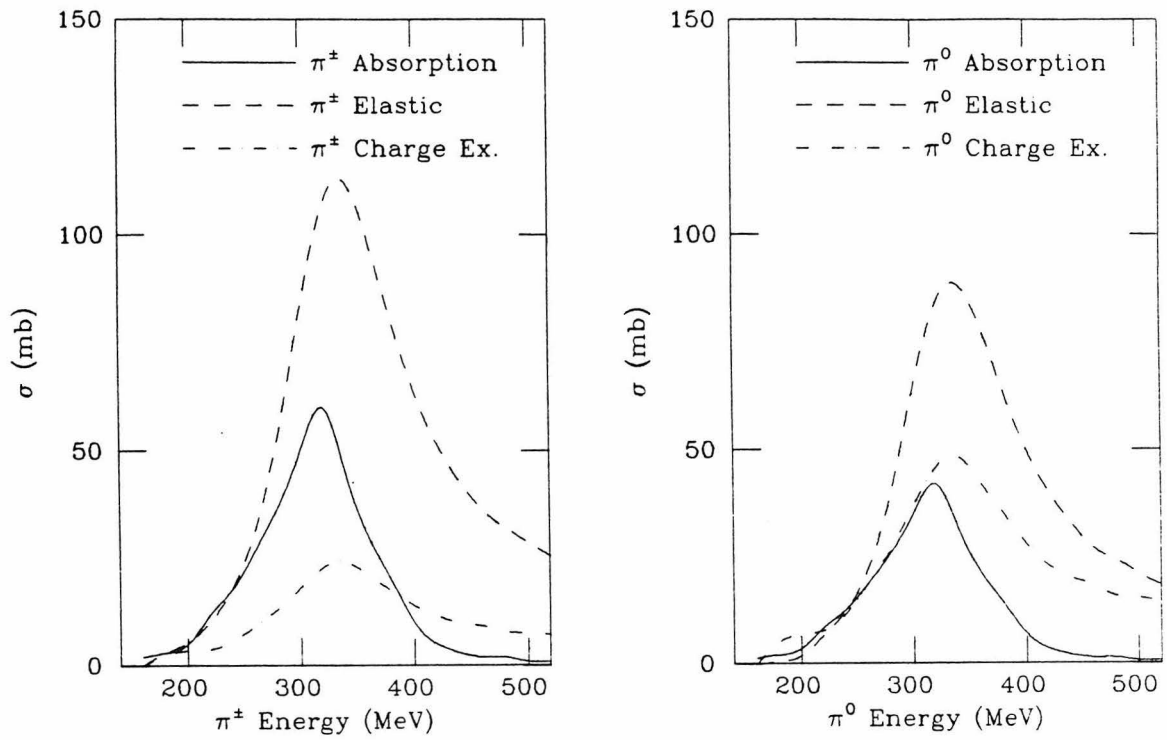


Figure 6-5. Mean cross-sections per nucleon for πN in the O^{16} nucleus.

for πO^{16} , so deriving the elementary cross-section is not trivial.⁶⁶ Various authors have assumed a “ ρ ” model and a “ ρ^2 ” model with mixed success.⁶⁸ Since we are using a cascade model which already includes scattering, we use Kielczewska’s fit,⁶⁸ which gives good agreement with the measured absorption on O^{16} . For the π^0 , we also use her calculation that $\sigma_{\text{abs}}(\pi^0\text{O}^{16})/\sigma_{\text{abs}}(\pi^+\text{O}^{16}) = 0.7$. In figure (6-6) we show the fate of π ’s in the O^{16} nucleus.

- (b) Kaons. Grand Unified theories predict proton decays to the K , and not the \bar{K} (see section 2-1), and so consequently we have \bar{s} -quarks in the final state. Inelastic interactions of the K^0 and K^+ are therefore inhibited, and we are left with the small possibility of elastic scattering ($\sigma \sim 10$ mb), and charge exchange ($\sigma \sim 3$ mb). We estimate that at worst, only 5% of the signal would be lost through nuclear interactions, and include this factor in our efficiency calculation.
- (c) Etas. The available data is in the form of the decay of nucleon resonances. Since the η is isoscalar, only the “ N ” resonances of $I = \frac{1}{2}$ are relevant. The dominant resonance is $N(1535)$ which decays to $N\eta$ with a 35% branching ratio, and an η momentum of 180 MeV in the resonance frame. Now, two-body proton decays give an η momentum of 300 MeV in the proton frame, which, coincidentally, corresponds to 180 MeV in the center of mass frame of the proton and η . This makes the η susceptible to scattering off spectator nucleons. The cross-sections are of the order 30 mb, corresponding to an interaction length of around 2 fm. The resonance can then decay to $N\pi$. We use published cross-sections⁷⁷⁻⁸² for $\pi^-p \rightarrow \eta n$; then, as in (a), derive cross-sections for the other permutations using isospin relations and detailed balance. In figure (6-7) we show the fate of η ’s inside the O^{16} nucleus.
- (d) Omegas. The ω is the least understood in terms of its interactions, one of the reasons being that there are no nucleon resonances available to it. We have taken a simple approach. At worst, we estimate that the inelastic

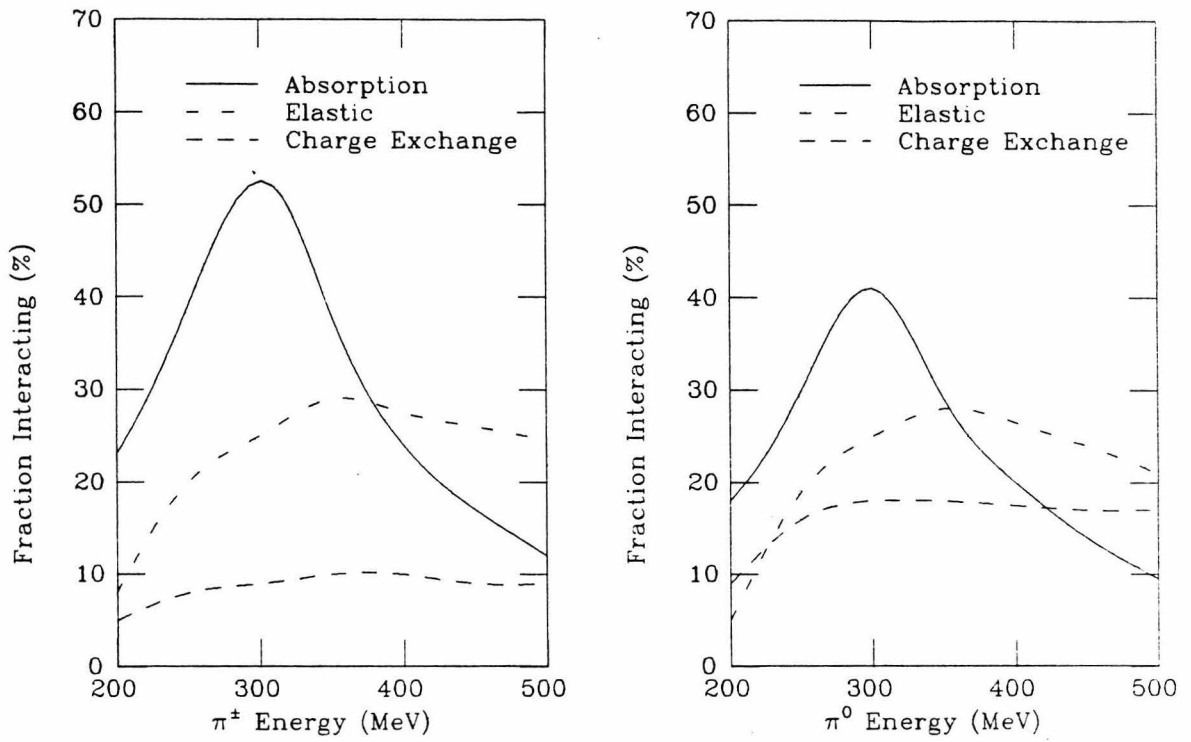


Figure 6-6. The fate of π 's inside the O^{16} nucleus.

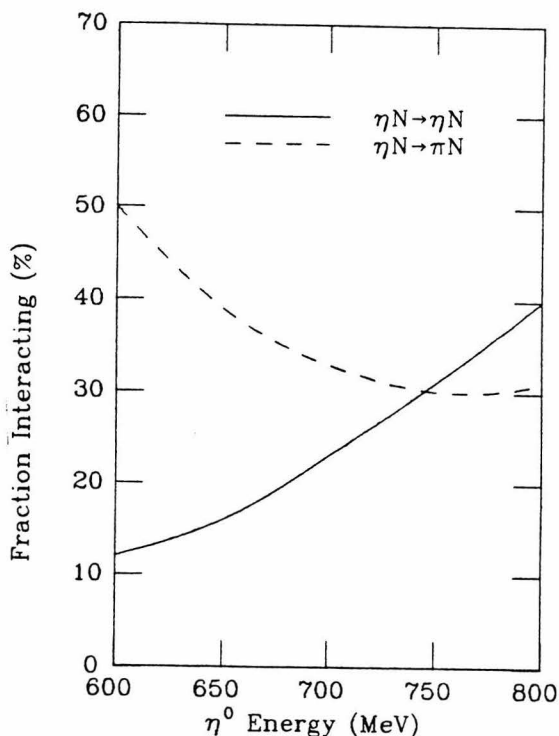


Figure 6-7. The fate of η 's inside the O^{16} nucleus.

nuclear effects are equal to that of the η multiplied by a spin factor of $\frac{1}{3}$. Since $< 40\%$ of the η 's interact to give pions, we will be overly conservative and assume that 20% of bound proton decays with an ω in the final state would be lost from the signal of any analysis because of nuclear interactions of the ω . Note that if the ω decays in the nucleus, the simulation still allows any resulting π 's to interact, which results in a further loss of efficiency.

Simulated Data Reduction. In a sense, there really is no "simulated" data reduction, because the simulated and real data are analyzed blindly by the same programs. After a simulation file has been generated, a new file is created consisting of only those events surviving the data reduction analysis chain (chapter 5). These events all have vertices reconstructed in the fiducial volume, and have between 40-300 firing P.M.T.'s, just as in the real data. The "reconstruction efficiency," ϵ_r , is defined for each branching mode, as the number of proton de-

Decay Mode	Reconstruction Efficiency	Decay Mode	Reconstruction Efficiency
$n \rightarrow \nu\gamma$	0.87	$n \rightarrow e^+\rho^-$	0.91
$p \rightarrow e^+\gamma$	0.93	$n \rightarrow \mu^+\rho^-$	0.61
$p_{\text{free}} \rightarrow e^+\gamma$	0.95	$n \rightarrow \nu\rho^0$	0.27
$p \rightarrow \mu^+\gamma$	0.80	$p \rightarrow e^+\rho^0$	0.84
$p_{\text{free}} \rightarrow \mu^+\gamma$	0.90	$p_{\text{free}} \rightarrow e^+\rho^0$	0.90
$n \rightarrow e^+\pi^-$	0.82	$p \rightarrow \mu^+\rho^0$	0.28
$n \rightarrow \mu^+\pi^-$	0.77	$p_{\text{free}} \rightarrow \mu^+\rho^0$	0.34
$n \rightarrow \nu\pi^0$	0.65	$p \rightarrow \nu\rho^+$	0.65
$p \rightarrow e^+\pi^0$	0.90	$p_{\text{free}} \rightarrow \nu\rho^+$	0.98
$p_{\text{free}} \rightarrow e^+\pi^0$	0.88	$n \rightarrow e^-\rho^+$	0.80
$p \rightarrow \mu^+\pi^0$	0.79	$n \rightarrow \mu^-\rho^+$	0.59
$p_{\text{free}} \rightarrow \mu^+\pi^0$	0.92	$n \rightarrow \nu\omega^0$	0.76
$n \rightarrow e^-\pi^+$	0.91	$p \rightarrow e^+\omega^0$	0.74
$n \rightarrow \mu^-\pi^+$	0.81	$p_{\text{free}} \rightarrow e^+\omega^0$	0.90
$n \rightarrow \nu K^0$	0.33	$p \rightarrow \mu^+\omega^0$	0.77
$p \rightarrow e^+K^0$	0.86	$p_{\text{free}} \rightarrow \mu^+\omega^0$	0.84
$p_{\text{free}} \rightarrow e^+K^0$	0.94	$n \rightarrow \nu K^{*0}$	0.22
$p \rightarrow \mu^+K^0$	0.61	$p \rightarrow \nu K^{*+}$	0.30
$p_{\text{free}} \rightarrow \mu^+K^0$	0.58	$p_{\text{free}} \rightarrow \nu K^{*+}$	0.71
$p \rightarrow \nu K^+$	0.27	$n \rightarrow e^-K^{*+}$	0.47
$p_{\text{free}} \rightarrow \nu K^+$	0.24	$n \rightarrow e^+e^-\nu$	0.94
$n \rightarrow e^-K^+$	0.77	$p \rightarrow e^+e^-e^+$	1.0
$n \rightarrow \mu^-K^+$	0.42	$p_{\text{free}} \rightarrow e^+e^-e^+$	0.87
$n \rightarrow \nu\eta^0$	0.64	$n \rightarrow \mu^+\mu^-\nu$	0.60
$p \rightarrow e^+\eta^0$	0.83	$p \rightarrow \mu^+\mu^-\mu^+$	0.82
$p_{\text{free}} \rightarrow e^+\eta^0$	0.96	$p_{\text{free}} \rightarrow \mu^+\mu^-\mu^+$	0.92
$p \rightarrow \mu^+\eta^0$	0.68		
$p_{\text{free}} \rightarrow \mu^+\eta^0$	0.86		

Table 6-1. Reconstruction efficiency for nucleon decay modes. We have included nuclear effects and meson branching ratios.

cays which survive the data reduction analysis chain, divided by the number which were generated in the fiducial volume. This definition includes taking into account the necessary meson branching ratios, nuclear effects, etc. In table (6–1), we list the decay modes and the reconstruction efficiencies derived from the simulations.

6.4 BACKGROUND SIMULATION

Overview of Monte-Carlo Files. Our background estimates, which we will derive in chapter 7, are based on the well-reasoned assumption that they are atmospheric neutrino dominated (section 3.3). Monte-Carlo simulations of background events were created using, as inputs,

- (a) neutrino flux estimates,
- (b) neutrino cross-sections, and
- (c) the types and four momenta of the interaction products from bubble chamber event data.

In all, 4 background files were made, using data from 3 bubble chamber experiments. For one of the experiments (Gargamelle), 2 opposing assumptions have been made, concerning a π/p ambiguity in certain tracks, to create 2 separate files for analysis. The bubble chamber events are chosen in a prescribed way, to match the flux estimates and cross-sections. The events are then generated in the simulated detector in the usual way (section 6.2)

In the following subsections, we shall explain some of the details of the inputs to the Monte-Carlo, including the various assumptions and approximations.

Neutrino Flux Estimates. Neutrino flux estimates have been made by various authors,^{83–86} based on the measured flux of primary protons, and the subsequent interaction chain in the atmosphere which we mentioned in section 3.3; see equation (3.24). In figure (6–8), we show some of the estimates as a function of energy for $(\nu_e + \bar{\nu}_e)$, and $(\nu_\mu + \bar{\nu}_\mu)$.

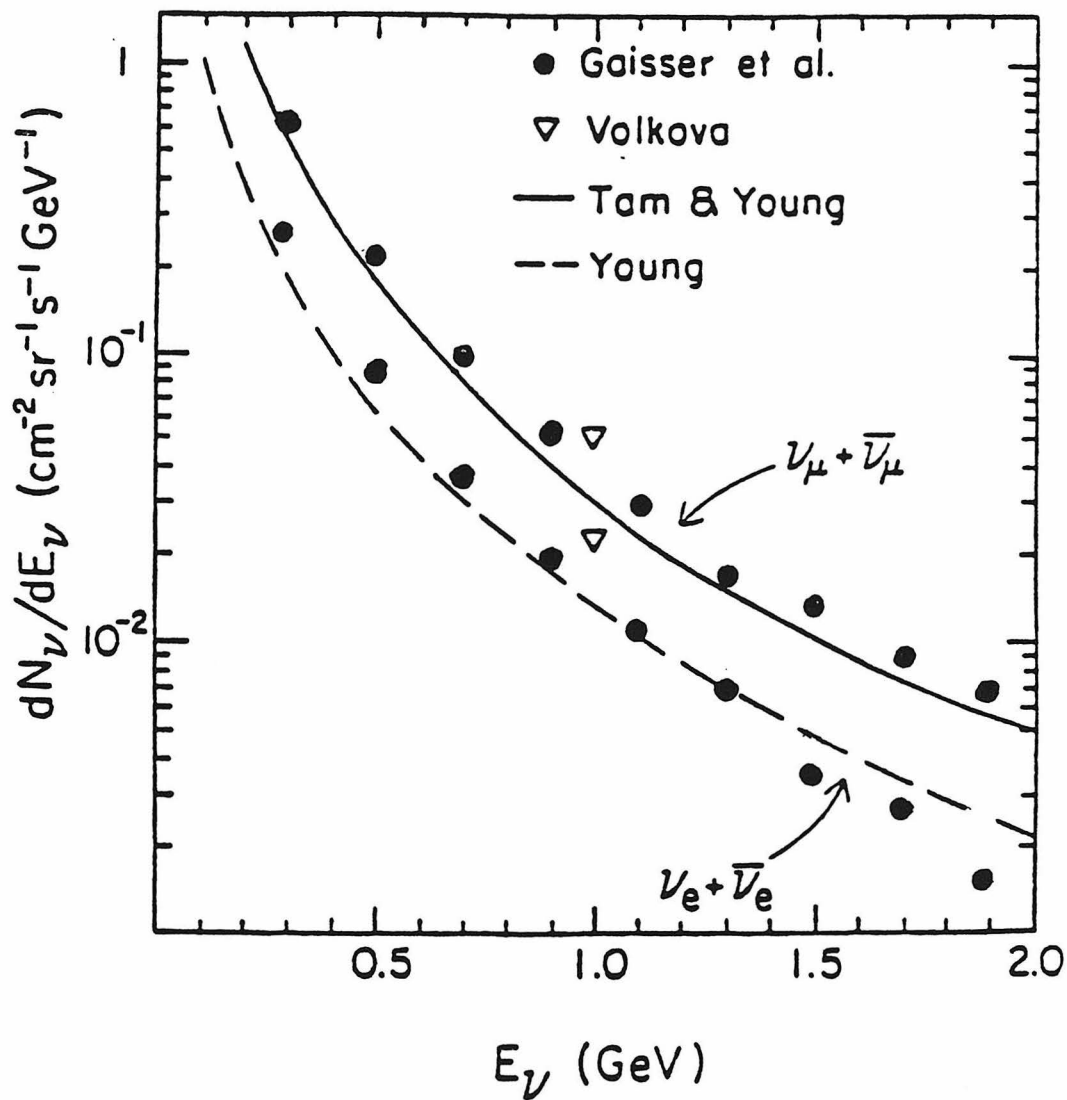


Figure 6-8. Various flux estimates of neutrinos vs. energy. We use Gaisser and Stanev's estimate.⁸³

The spectrum follows the cosmic ray primaries, and goes as $E^{-2.7}$ in our energy range. The ratio of fluxes for $(\nu_\mu + \bar{\nu}_\mu) : (\nu_e + \bar{\nu}_e)$ is about 2, basically following the pion and muon decay chain. The ratio of fluxes for $\nu_e : \bar{\nu}_e$ is about 1.25, following the ratio of $\pi^+ : \pi^-$ production, and the ratio for $\nu_\mu : \bar{\nu}_\mu$ is essentially unity, due to the fact that muon number is conserved. This number increases slightly above unity for neutrinos with energies greater than 2 GeV, because of the finite lifetime of the muon (i.e., a net muon number is “lost” in the muons which pass by without decaying).

The flux is approximately isotropic, the most significant anisotropy being a horizontal enhancement of less than 20%, caused by the increased slant depth for the pion decay in the atmosphere. The Earth’s magnetic field at our latitude (52°) cuts off the primary spectrum below 2 GeV, and has a small effect on the local downward flux of neutrinos at low energies. For purposes of studying proton decay, considerations of a slightly anisotropic flux are academic, because the background arises only from neutrino event topologies and energies. Hence, for the background simulation, we use an isotropic flux.

The total flux varies by about 25% at 1 GeV with the activity of the solar magnetic field. The solar cycle has a period of 11 years, and we have taken data at around the point of maximum activity (and hence, minimum flux).

Based on the difference between results of various calculations, we estimate a $\pm 20\%$ error in flux estimates at neutrino energies relevant to proton decay. In generating samples of background events, we have used the calculations of Gaisser and Stanev,⁸³ who have conveniently made calculations explicitly for I.M.B. detector, and have included the effect of the solar cycle, and the geomagnetic cutoff.

Neutrino Cross-Sections. At very high energies (> 10 GeV), neutrino inclusive cross-sections per nucleon rise linearly with energy with a measured coefficient of $0.67 \pm 0.02 \times 10^{-38} \text{ cm}^2 \text{ GeV}^{-1}$. In figure (6–9), we show the various measurements

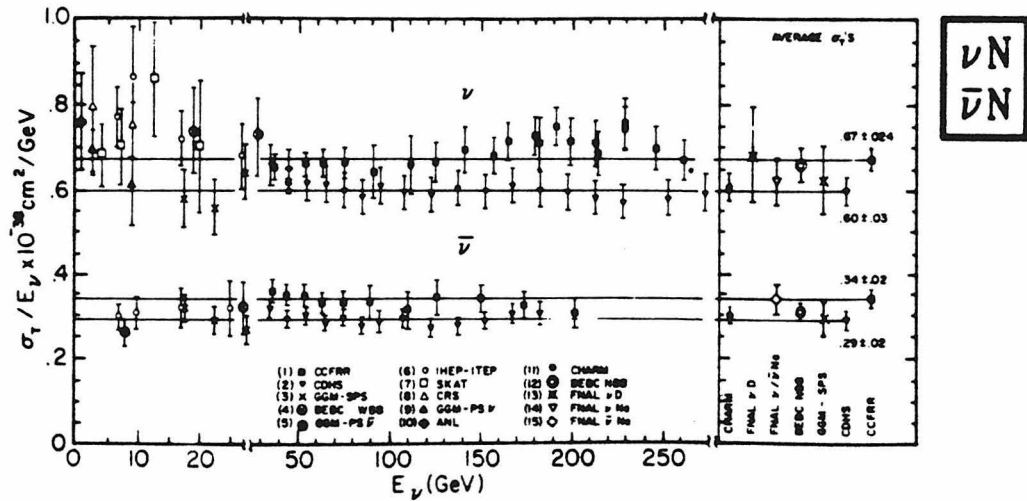


Figure 6-9. Inclusive cross-section coefficients for νN and $\bar{\nu} N$ taken from the particle data book.⁸⁷ We are interested in $E < 10 \text{ GeV}$, for which we assume coefficients 0.75 and 0.30, respectively, with an estimated 10% error.

taken from the particle data book,⁸⁷ for which we are interested in energies below 10 GeV. Linearity is still approximately valid, though the linear coefficient appears to be in the range of $0.7-0.8 \times 10^{-38} \text{ cm}^2 \text{ GeV}^{-1}$. We shall assume a value of $0.75 \times 10^{-38} \text{ cm}^2 \text{ GeV}^{-1}$, with an estimated error of 10%. For the anti-neutrinos, we assume a value of $0.3 \times 10^{-38} \text{ cm}^2 \text{ GeV}^{-1}$.

It is, perhaps, amusing to consider a phenomenon discovered in 1973, to be a background to a possible phenomenon in 1985. For neutral current events, we assume a world average⁸⁸ of the ratios of neutral to charged current inclusive cross-sections of $R_\nu = 0.30$, and $R_{\bar{\nu}} = 0.36$.

Bubble Chamber Data. To emulate the background event topologies, and track energies, we used the particle types and four momenta of tracks from three different bubble chamber experiments:

- (a) The Gargamelle bubble chamber,^{89,90} situated in the CERN PS, with a proton energy of 24 GeV. We used 6200 ν_μ and 4500 $\bar{\nu}_\mu$ events from a freon (CF_3Br) exposure. We used two opposing interpretations of this data for the cases of tracks with a π^+/p^+ ambiguity, and call the background estimates "GGM/ π ," and "GGM/ p " respectively.
- (b) The Brookhaven 7-foot bubble chamber,⁹¹ situated in the Brookhaven AGS, with a proton energy of 28 GeV. We used 7900 ν_μ and 4300 $\bar{\nu}_\mu$ events from a neon-hydrogen (5Ne : 3H) exposure. We call the background estimate "BNL."
- (c) The Argonne 12-foot bubble chamber,^{92,93} situated in the Argonne ZGS with a proton energy of 13.4 GeV. We used 500 ν_μ events from a deuterium (H^2) exposure. We call the background estimate "ANL."

The simulation for the neutrino types for which we have no data, are derived from the above events by making a few changes. In the case of the ν_e events, we simply substituted the muon 3-momentum for the electron 3-momentum. Although this does not conserve energy, it is only a good approximation considering

the small muon mass. In the case of neutral current events, the muon was simply removed from the charged current events. Any effect of this approximation in the context of proton decay will be small, because (i) neutral current topologies are less “dangerous” than charged current topologies, because they have at least one invisible track; (ii) the low neutral current cross-section; (iii) the invisible neutrino track means that the ratio of charged to neutral current events at a particular visible energy is further decreased.

The bubble chamber events were selected according to the flux times cross-section estimates. Because the bubble chamber neutrino spectrum is not quite the same as the atmospheric spectrum, we had to reuse events of low energy in order to get the necessary statistics at the high energy end. This is a reasonable thing to do, considering that it is the high energy neutrinos which are far more likely to be proton decay background; furthermore, the reused events were generated at different parts of the detector and with different orientations.

Neutrino Event Rates. The event rate for neutrino interactions, can, perhaps, be calculated on the back of the proverbial envelope, but what is relevant to us is the rate of events we expect to see in our data sample, having passed all of the data reduction requirements. A more accurate estimate can be given by using the simulated data files, and using the same data reduction chain as was used for the real data.

The result of this calculation gives an event rate of $1 \pm 0.2 \text{ day}^{-1}$, where we assume the error is dominated by the flux calculations. In the final analysis, we have decided not to rely on the *total* flux estimates for event rates, but have, instead, quantified the characteristics of events in terms of percentages, and then normalized these to the number of real data events observed. We justify this decision by the following line of reasoning:

- (a) The flux estimates have a rather large error of $\pm 20\%$.
- (b) As we shall see in chapter 7, the fraction of multi-track events agrees with

the data to within 5% of the total, giving a plausible estimate the possible fraction of proton decays to be *at most* 5%.

- (c) Therefore, our own data gives a better estimate on the number of neutrino events in the data sample than any simulation can, without even considering the errors in cross-sections.

We would like to point out in advance that this assumption has very little bearing on our final results, since the error in the background estimate is far smaller than the statistical error in the number of candidates we observe.

7. The Search for a Signal

7.1 NUCLEON DECAY EXCLUSIVE FINAL STATES.

General Physical Characteristics. In the search for nucleon decay, we look for exclusive final states which satisfy the following basic symmetries:

- (a) Conservation of energy. This constrains the decay products to particle types of mass less than the nucleon. It also provides a useful constraint when searching for decay candidates.
- (b) Conservation of angular momentum. Along with (a), this implies that an odd number of leptons must be present in the final state. We note that nucleon decay must necessarily violate lepton number conservation.
- (c) Conservation of charge.
- (d) Conservation of momentum. This places no constraint on the particle types, but it does provide for an excellent nucleon decay signature. For free proton decays, the events would have zero momentum, and for bound nucleon decay in O^{16} , the momentum distribution peaks at 150 MeV, with a HWHM of 75 MeV; see figure (2-2).

From the physicist's point of view, even though these laws have not been proved to be valid at 10^{-28} m the "correct" way to proceed is to test one law at a time, and assume that baryon number conservation is broken on a scale much larger than for the above laws (if, indeed, they are broken at all). We summarize the candidate final states as follows, where energy and charge conservation are understood:

$$N \rightarrow \ell + nX, \text{ where } \begin{cases} X \in \{2\ell, \gamma, \pi, K, \eta, \rho, \omega, K^*\}; \\ \ell \in \{\nu, e, \mu\}; \\ \text{and } n = 1, 2, 3, \dots \end{cases} \quad (7.1)$$

In many cases, the decay products can themselves decay in different ways. It is important to look for each of these decays in order to increase the sensitivity, and to provide a consistency check should a signal be found.

General Visible Characteristics. The four-momentum constraint on nucleon decays is really the key to finding a signal, should it exist. A significant excess of events with low momenta and of energies around 1 GeV would indeed be profound proof of proton decay. However, the information available from our detector is limited, in particular:

- (a) Events with final state neutrinos, or with particles created below Cherenkov threshold, have invisible tracks, and so we have missing four-momentum.
- (b) Particle identification is poor, leading to difficulties in converting a track's visible energy into a true energy and momentum.

Despite these setbacks, the visible quantities are, on the whole, well constrained for each individual decay mode (but not for proton decays as a whole). The strategy is therefore clear: each exclusive final state must be searched for on an individual basis.

For most of the decay modes, the events are visibly characterized by at least two tracks of wide opening angles. The SU(5) favored mode, $p \rightarrow e^+ \pi^0$ has the most distinguished signature of two, almost equally energetic tracks with an opening angle greater than 150° . It is generally the neutral mesons (except for the rho) which decay into showering tracks, so conservation of charge and angular momentum imply that the most visibly energetic nucleon decays with a visible momentum balance (for a water Cherenkov detector) are of the type $p \rightarrow e^+ + \text{meson}$. By similar reasoning, neutron decays tend to have less visible energy, with a greater apparent momentum imbalance, and so do not have such an obvious signature. Supersymmetric theories favor a neutrino in the final state, which makes for an apparent momentum imbalance. Consequently, these modes are more background limited.

Degradation of the signal occurs for two basic reasons.

- (a) A finite detector resolution.
- (b) Nuclear interactions of the decay products.

Since we have about 180 P.M.T.'s firing at approximately the 1 p.e. level for an event of visible energy 940 MeV, the statistical visible energy resolution is

$$\frac{\sigma_{\text{stat}}(E_c)}{E_c} = \frac{7\%}{\sqrt{E_c}(\text{GeV})}. \quad (7.2)$$

The systematic error, arising mainly from the absolute energy calibration, has been conservatively estimated at 15%, so for individual events, systematics become important above $E_c \simeq 200 \text{ MeV}$, which actually corresponds to the number of firing P.M.T.'s required for analysis.

$$\frac{\sigma_{\text{sys}}(E_c)}{E_c} = 15\%. \quad (7.3)$$

We note that the percentage resolution of *true* energy, E , (given a particle hypothesis for a track) is less than or equal to the visible energy resolution, because the amount of visible energy lost below the Cherenkov threshold is precisely known.

$$\frac{\sigma_{\text{sys}}(E)}{E} < 15\%. \quad (7.4)$$

Therefore, the true percentage energy resolution is actually better for events containing non-showering tracks, when the particle types are assumed.

We also have a finite ability to identify tracks and to resolve their directions, which contributes to an error in the total momentum of an event. One approach to this problem is to not attempt to analyze tracks at all, and base the analysis entirely on global, visible event variables (see section 7.2.) The other approach is to search for only well-defined tracks to perform a kinematic analysis,

which sometimes means trading efficiency for a more substantial decrease in the expected background (see section 7.4.)

In chapter 6, we discussed the interactions of decay products as they propagate through the parent nucleus, and through the surrounding water. There are two approaches to dealing with this problem. First, one can search only for “clean” signals from decays where the products either did not interact, or sustained interactions which only slightly affected the experimental observables. The second method is to search for those events where the products did interact. We employ either, or both, of these approaches, depending upon the decay mode. The first method is applicable when either the fraction of interacting products is small, or when the events with interactions have very unconstrained observables and may easily be imitated by background events. The second method is usually used by necessity, either when the “clean” signal is below our analysis threshold of about $E_c \simeq 200 \text{ MeV}$ (e.g., $p \rightarrow \nu\pi^+$ may be observed if the π^+ charge exchanges to a π^0), or when the probability of decay product interaction is very large (e.g., $n \rightarrow \nu\rho^0$, the rho decays into pions within the nucleus, and the probability of both pions surviving unscathed is $\sim 10\%$).

As mentioned in the previous subsection, the decay products themselves can often decay in various ways. To search for each of these branching modes generally implies a different choice of criteria for each mode. To search for nucleon decay candidates, the choice of event requirements depends, to some degree, upon the expected background characteristics. In sections 3.3 and 6.3, we discussed this qualitatively. In order to be quantitative, we must investigate the background distributions specific to the analysis procedure. In the rest of this chapter, we shall do this by analyzing the background simulation in an identical fashion to the signal simulation, and the data.

7.2 VISIBLE ENERGY, ANISOTROPY ANALYSIS^{46,47}

This analysis is based on the idea, outlined in the previous section, that a signal may be discovered using global, visible event variables. The variables we have chosen are the total visible energy of the event, E_c , the energy anisotropy, A , and the number of muon decays in the event, n_μ . We will now define, and discuss these quantities in the context of proton decay.

Visible Energy. The visible energy of an event was defined by equation (3.19) as “the energy of a shower which would produce the equivalent light yield.” The way in which it is calculated for an event is explained in section 4.3:

$$\begin{aligned} E_c &= \sum_{i=1}^{2048} e_i \\ &= k \sum_{i=1}^{2048} \left(\frac{\alpha_i}{\Lambda(r_i)A(\theta_i)} \right) q_i. \end{aligned} \tag{4.6}$$

In figure (3-1) we showed the relation between the true energy of a particle, and the amount of visible energy it would deposit in a water Cherenkov detector. Due to these finite Cherenkov threshold effect, visible energies for a particular final state are confined to regions either at or below 1 GeV. As a rule of thumb (though not used explicitly in our analysis), the expected visible energy for a particular mode of decay can be approximated by subtracting from 940 MeV:

- (a) 230 MeV for each μ ;
- (b) 300 MeV for each π^\pm .

Anisotropy. The energy anisotropy, A_c , is defined as the magnitude of the energy-weighted vector sum of directions from the event vertex to those P.M.T.’s which fire within ± 14 ns of their expected firing time, t'_0 :

$$A_c = \left| \sum_i e_i \hat{r}_i \right| / \sum_i e_i, \quad \text{for } i : |t'_i - t'_0| < 14 \text{ ns}, \tag{7.5}$$

where the energy contribution from each tube, e_i , is defined by the above equation (4.6).

The timing requirement reduces the “noise” resulting from tubes which fire due to scattered light, because these tubes contain little directional information. For the purposes of this calculation, t'_0 is determined by the following iterative procedure. First, the firing time of each tube, t_i , is corrected for the distance to the event vertex to give the timing residuals, t'_i . The distribution of the corrected residuals should now follow the standard P.M.T. timing distribution, with an excess of late firing tubes from scattered light. As a first guess for t'_0 , the mean of the residual distribution is taken. Then, so as to reduce the influence of the “scattered tubes,” t'_0 is taken to be the mean time residual of tubes firing within ± 28 ns of the first guess. We note that the time window for acceptance, ± 14 ns, is much greater than the mean vertex error of 1 m, which corresponds to 4 ns, so that the tube selection is negligably affected by our vertex resolution. Furthermore, it is much greater than the standard P.M.T. time jitter of 5.5 ns HWHM, figure (4-3).

The anisotropy is a measure of the apparent momentum balance for an event. A single-track event has an anisotropy of approximately $A_c \simeq \cos(41.7^\circ) = 0.75$, whereas multi-track events have anisotropies smaller than this. An event with two tracks of equal visible energy, and opening angle, ϕ , has an anisotropy $A_c \simeq 0.75 \cos(\phi/2)$. If the two tracks are visibly separated, i.e., $\phi > 84^\circ$, then $A_c < 0.56$. Events which have equally energetic back-to-back tracks, or multi-track events which give an isotropic energy deposition, have anisotropies $A_c = 0$.

For purposes of analysis, we will divide the data into “single-prong” and “multi-prong” events as follows (“prong” means a visible track):

$$\begin{aligned} A_c(\text{single-prong}) &> 0.55, \\ A_c(\text{multi-prong}) &< 0.55. \end{aligned} \tag{7.6}$$

For most of the nucleon decay modes, we demand that the event be at least multi-

pronged. The advantage of using this variable is to eliminate much of the neutrino interactions which are dominated by single-prong, quasi-elastic scattering.

Muon Decays. The definition of a muon decay signal was given in section 4.3. Events can be rejected, or accepted as candidates for specific decay modes on the basis of its number of muon decays, n_μ . This is particularly to our advantage when we are studying models which suggest that protons decay into many particles, including μ 's and π^+ 's. Any local enhancement or depletion of events with muon decays in the E_c - A_c plane would be suggestive of proton decay.

Background/Data Comparison.

- (a) **Multi-Prong Events.** Figure (7-1) shows the anisotropy distributions for real data events, and for the background simulations. We find 52 out of 326 events in the real data to be “multi-pronged,” as defined in equation (7.6). This constitutes $16.0 \pm 2.0\%$ of the total sample, which is to be compared with the background estimates of (i) $10.3 \pm 0.7\%$ (GGM/ p), (ii) $13.1 \pm 1.2\%$ (GGM/ π), and (iii) $11.4 \pm 1.7\%$ (ANL), where the error bars are statistical. If the proton decay signal is in the form of multiprong events, we find the signal to be present at the level of 2.4σ , 1.1σ , and 1.6σ for the respective background estimates. We conclude that, based on the number of multiprong events alone, there is no significant evidence for proton decay.
- (b) **Energy Spectrum.** Figure (7-2) shows the visible energy distributions for the data, and for the various background simulations. There is no obvious evidence for new physics based on this distribution. Figure (7-3) shows the same distributions for those events found to be multi-pronged. The slight excess of 10–20 multi-pronged events, as described above in (a), appears to be spread uniformly about the visible energy distribution. This lack of an obvious signal indicates that we must search harder.
- (c) **Events with Muon decays.** The fraction of events with one muon decay, $\epsilon(n_\mu = 1) = 85/326 = 26.1 \pm 2.4\%$, and with more than two muon de-

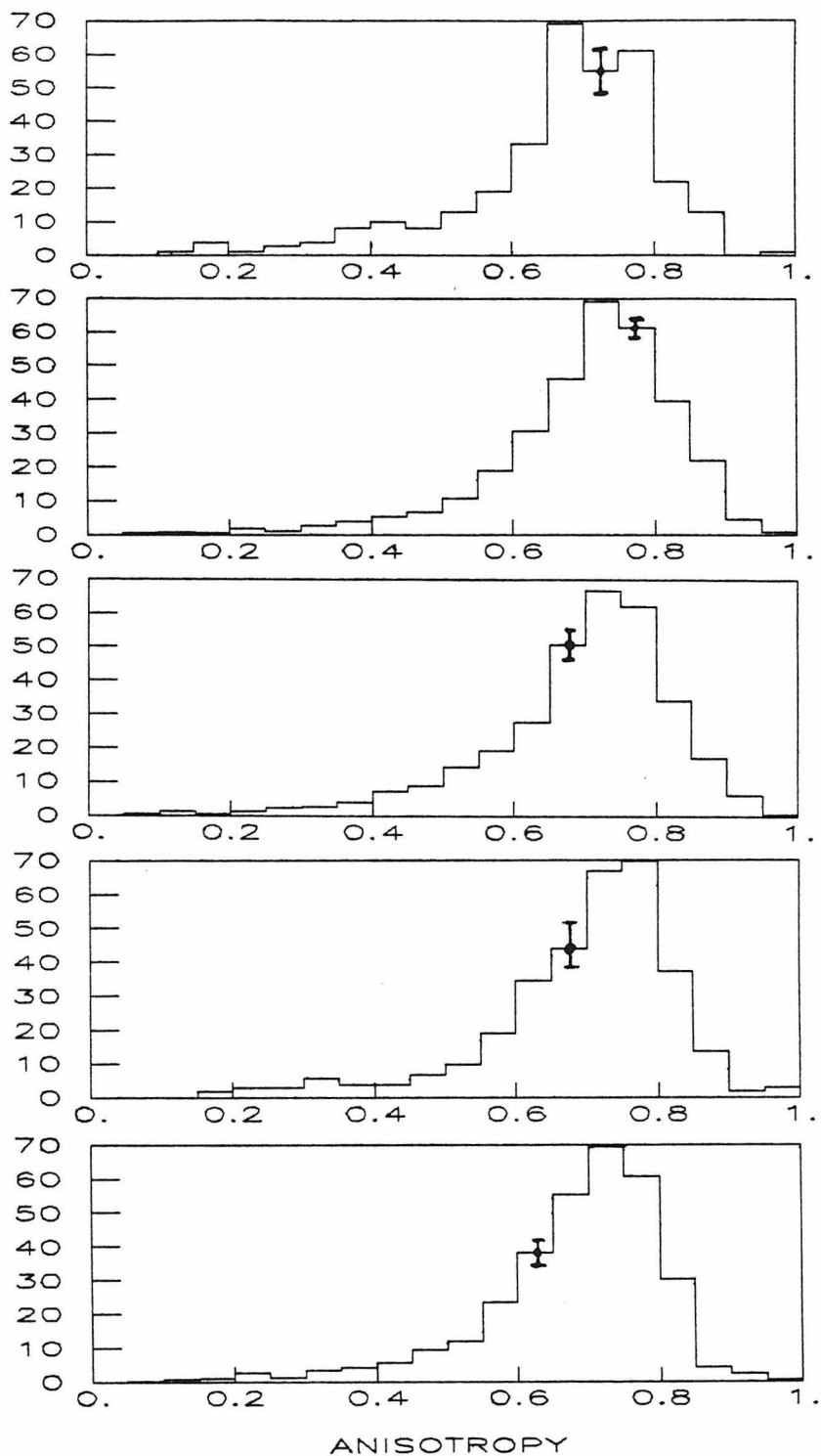


Figure 7-1. Event distributions in anisotropy for (a) real data, (b) GGM/p (c) GGM/ π (d) ANL (e) BNL.

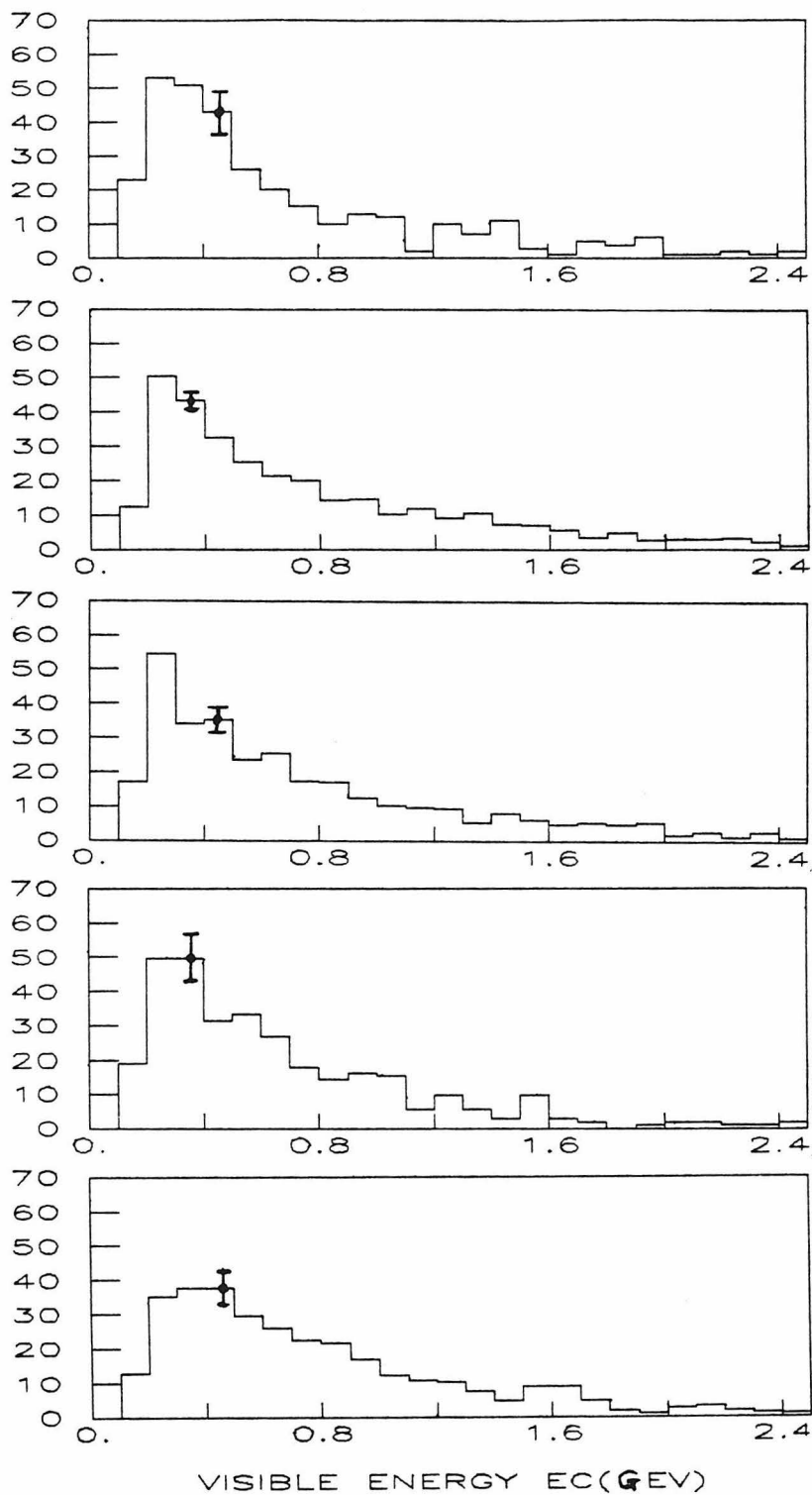


Figure 7-2. Event distributions in visible energy for (a) real data, (b) GGM/p (c) GGM/ π (d) ANL (e) BNL.

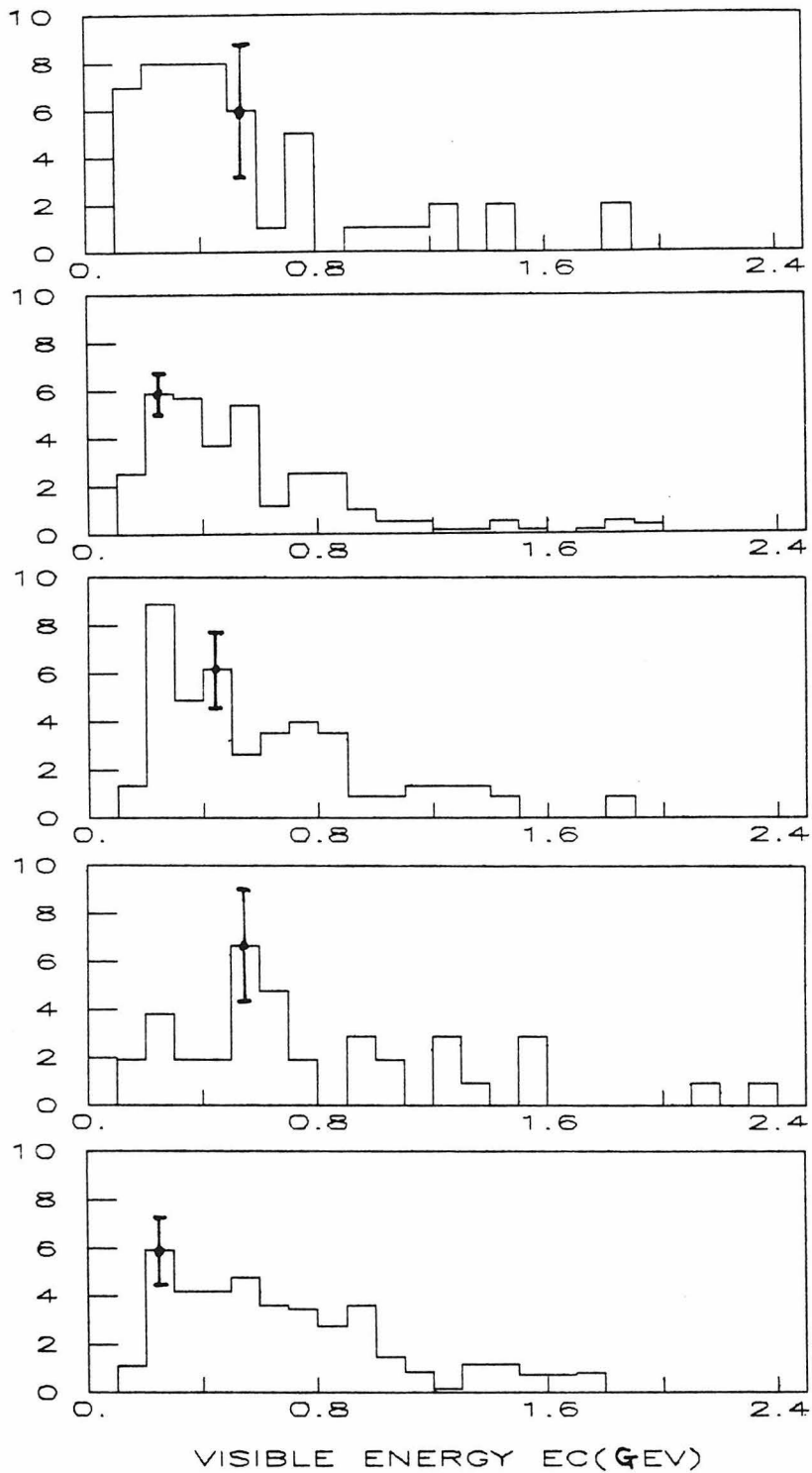


Figure 7-3. Multi-prong event distributions in visible energy for (a) real data, (b) GGM/p (c) GGM/ π (d) ANL (e) BNL.

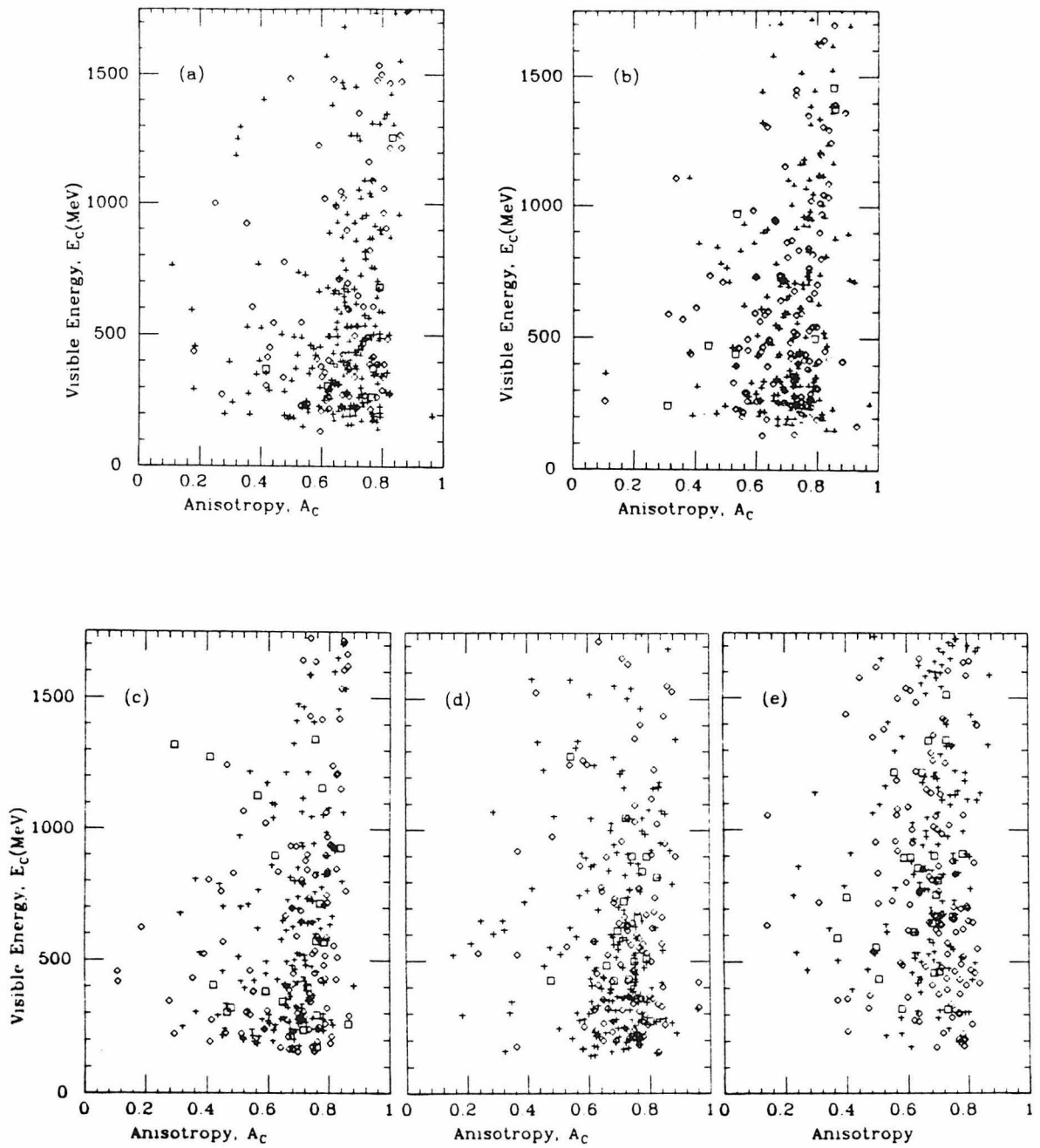


Figure 7-4. Event distributions in the E_c - A_c - n_μ plane for (a) real events, (b) GGM/p (c) GGM/ π (d) ANL (e) BNL. The number of muon decays is + = 0, \diamond = 1, \square = 2.

cays, $\epsilon(n_\mu > 2) = 7/326 = 2.1 \pm 0.8\%$. This is to be compared with the background estimates given in equation (7.7), of 33% and 5%, respectively. The difference between the observed and the expected fraction of events with one muon decay is a significant 2.8σ effect. The cause of this discrepancy is unclear at present. There is no significant change in these numbers if we look only at multi-pronged events, or events with visible energies less than 500 MeV. The depletion of events with muon decays appears to be independent of the region on the E_c - A_c plane (to within statistical fluctuations). This would not be expected if, say, the proton decayed preferentially through modes with no muon decay in the final state, so we believe the discrepancy is not connected with proton decay.

- (d) Figure (7-4) shows the data events plotted in the E_c - A_c - n_μ plane, along with similar plots for the various background estimates. The similarity between the plots is good evidence that we are, at least for the most part, observing atmospheric neutrino interactions.

Expected Signal/Background Comparison. The candidate requirements on the number of muon decays of an event, n_μ , were decided in a systematic manner, and were decided entirely upon the signal efficiencies and the expected background:

- (a) In table (7-1), we list the expected fraction of background events which contain $n_\mu = 0, 1, > 2$ muon decays. There was very good agreement between the three simulations, with mean fractions of:

$$\begin{aligned}\epsilon_\mu(n_\mu = 0) &= 62 \pm 1.1\%, \\ \epsilon_\mu(n_\mu = 1) &= 33 \pm 0.8\%, \\ \epsilon_\mu(n_\mu > 2) &= 5 \pm 0.5\%.\end{aligned}\tag{7.7}$$

- (b) Next, we investigated the E_c - A_c dependence of ϵ_μ . We list in table (7-2) the values of ϵ_μ for the subset of events with $E_c < 500$ MeV, and in table

	0 muons	1 muon	2 muons
GGM/proton	62.8+-1.1%	33.9+-1.1%	3.4+-0.4%
GGM/pion	60.5+-1.8%	32.8+-1.7%	6.7+-0.9%
ANL	62.9+-2.6%	32.5+-2.5%	4.7+-1.1%
Real Data	71.8+-2.5%	26.1+-2.4%	2.1+-0.8%

Table 7-1. Fraction of all events containing μ decays for data and simulations.

	0 muons	1 muon	2 muons
GGM/proton	61.2+-1.7%	35.8+-1.7%	2.9+-0.6%
GGM/pion	61.2+-2.7%	31.2+-2.6%	7.6+-1.5%
ANL	64.3+-3.8%	31.8+-3.7%	3.8+-1.5%
Real Data	71.2+-3.5%	26.5+-3.4%	2.4+-1.2%

Table 7-2. Fraction of low-energy events containing μ decays with $E_c < 500$ MeV.

	0 muons	1 muon	2 muons
GGM/proton	57.8+-3.5%	37.7+-3.4%	4.5+-1.5%
GGM/pion	53.1+-5.1%	38.5+-5.0%	8.3+-2.8%
ANL	69.2+-7.4%	25.6+-7.0%	5.1+-3.5%
Real Data	69.2+-6.4%	28.8+-6.3%	1.9+-1.9%

Table 7-3. Fraction of multi-prong events containing μ decays with $A_c < 0.55$

(7-3) for the “multi-prong” subset (see equation (7.6)) with $A_c < 0.55$. We concluded that the effect is negligible enough to enable us to decide on the n_μ criteria independent of the E_c - A_c plane.

- (c) We found the fraction of muon decays expected of the signal for all the decay modes under investigation, and for each mode we determined the appropriate n_μ requirement by maximizing the signal to background ratio of the fraction of muon decays, using the background values of equation (7.7).

The above approach has the advantages that the criteria are not biased by any of the experimenter’s prior knowledge of the real data (which is always a problem in experimental analyses), and the inherent statistical fluctuations which may be present for the background estimates in local regions of the E_c - A_c plane.

Having automatically selected the muon decay requirement, the anisotropy and visible energy requirements were decided upon for particular decay mode candidates by studying the E_c - A_c plane as a whole. In figure (7-5) we show some examples of the expected signal as derived from Monte-Carlo simulations discussed in section 6.2. The requirements were chosen without reference to the data characteristics, by keeping in mind the following general observations:

- (a) The background increases with larger values of A_c , and rapidly increases for $A_c > 0.5$ (due to quasi-elastic neutrino scattering).
- (b) The estimate on the magnitude of the systematic error in the visible energy is $< 15\%$. Our acceptance windows were chosen to be much larger than this.
- (c) Some decay modes are physically related (e.g., those for which all the tracks are showering). We have attempted to keep the requirements physically consistent, without being blindly dependent upon Monte-Carlos.

Results. Because of the relatively large uncertainty in the background estimates, we have not attempted a background subtraction, but have instead cal-

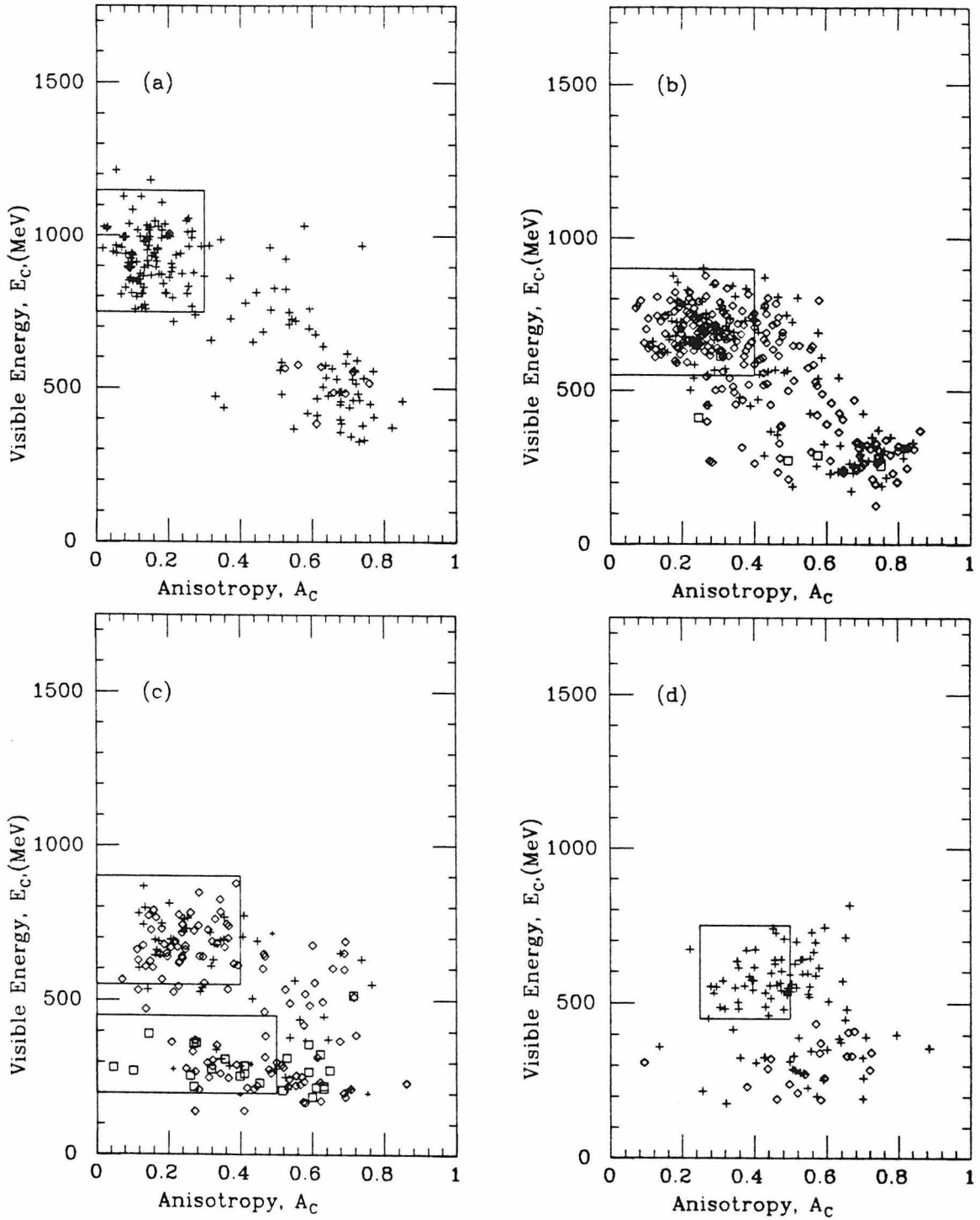


Figure 7-5. Event distributions in the E_c - A_c - n_μ plane for simulated proton decay (a) $p \rightarrow e^+ \pi^0$, (b) $p \rightarrow \mu^+ \pi^0$, (c) $p \rightarrow \mu^+ \eta^0$, (d) $n \rightarrow \nu K^0$. The number of muon decays is $+ = 0, \diamond = 1, \square = 2$.

Table 7-4 (opposite page). Partial lifetime limits for 37 nucleon decay modes at the 90% confidence level without background subtraction. Nuclear interactions of mesons have been taken into account. Direct nuclear effects on the bound nucleon lifetime are assumed negligible for the water limits, an assumption which is unnecessary for the free limits.

culated lower limits on the partial lifetimes of the proton under the most conservative assumption that all the candidates are due to proton decay.

The formula for calculating lifetime limits was explained in chapter 2:

$$\tau/B = \frac{t_d N_n}{U_c} (\epsilon_f f_f + \rho \epsilon_b f_b), \quad (2.18)$$

where U_c is an upper limit on the number of candidates, which we will take at the 90% confidence level. Since the number of observed candidates, N_c , in a given region over a given livetime has a Poisson distribution, $P(N_c, \bar{N}_c)$, the appropriate equation is

$$\sum_{i=0}^{N_c} P(i, U_c) = 10\%, \quad (7.8)$$

which must be solved numerically. For cases where we have two independent acceptance regions (due to different meson branching modes), we define the confidence level of an upper limit on the total number of candidates, as the probability that we would have observed more than the measured number of candidates in either region. Taking the converse statement of this definition:

$$\sum_{i=0}^{N_{c1}} \sum_{j=0}^{N_{c2}} P(i, \epsilon_1 U_c) P(j, \epsilon_2 U_c) = 10\%, \quad (7.9)$$

where the subscripts 1 and 2 denote the two regions, and the relative signal efficiencies, ϵ_1 and ϵ_2 add up to one. Equation (7.8) is just a special case of (7.9), with $\epsilon_1 = 1$.

Decay Mode	E_c (MeV)	A_c	n_μ	ϵ	GGM (p)	GGM (π)	ANL	BNL	Mean N_b	Cand. N_c	Limit (10^{31} yr)
$n \rightarrow \nu\gamma$	300-650	>0.6	0	0.82	53.5	52.8	62.9	48.0	54.3	69	1.0
$p \rightarrow e^+\gamma$	750-1150	<0.3	0	0.84	0.2	0.9	1.0	2.7	1.2	1	27.2
$p_{\text{free}} \rightarrow e^+\gamma$	750-1150	<0.25	0	0.90	0.2	0.4	0.0	2.7	0.8	1	5.8
$p \rightarrow \mu^+\gamma$	550-900	<0.4	1	0.55	1.7	0.9	0.0	1.6	1.0	1	17.7
$p_{\text{free}} \rightarrow \mu^+\gamma$	550-900	<0.35	1	0.51	0.8	0.9	0.0	1.6	0.8	0	5.6
$n \rightarrow e^+\pi^-$	450-950	<0.5	0	0.35	4.7	5.8	9.5	8.0	7.0	7	3.0
$n \rightarrow \mu^+\pi^-$	250-550	<0.5	1	0.22	3.7	4.9	1.9	4.5	3.7	7	1.9
$n \rightarrow \nu\pi^0$	300-650	>0.6	0	0.56	53.5	52.8	62.9	48.0	54.3	69	0.7
$p \rightarrow e^+\pi^0$	750-1150	<0.3	0	0.50	0.2	0.9	1.0	2.7	1.2	1	16.2
$p_{\text{free}} \rightarrow e^+\pi^0$	750-1150	<0.25	0	0.85	0.2	0.4	0.0	2.7	0.8	1	5.5
$p \rightarrow \mu^+\pi^0$	550-900	<0.4	1	0.28	1.7	0.9	0.0	1.6	1.0	1	8.9
$p_{\text{free}} \rightarrow \mu^+\pi^0$	550-900	<0.35	1	0.56	0.8	0.9	0.0	1.6	0.8	0	6.1
$n \rightarrow e^-\pi^+$	450-950	<0.5	0	0.21	4.7	5.8	9.5	8.0	7.0	7	1.8
$n \rightarrow \mu^-\pi^+$	250-550	<0.5	2	0.10	0.3	1.8	1.0	0.0	0.8	1	2.5
$n \rightarrow \nu K^0$	450-750	0.25-0.5	0	0.12	2.5	3.5	5.7	3.9	3.9	3	1.8
$p \rightarrow e^+K^0$	750-1150	<0.3	0	0.14	0.2	0.9	1.0	2.7	1.2	1	
	300-600	<0.5	1	0.15	4.2	4.9	1.9	4.3	3.8	6	4.7
$p_{\text{free}} \rightarrow e^+K^0$	750-1150	<0.3	0	0.21	0.2	0.9	1.0	2.7	1.2	1	
	300-600	<0.5	1	0.14	4.2	4.9	1.9	4.3	3.8	6	1.4
$p \rightarrow \mu^+K^0$	550-900	<0.4	1	0.12	1.7	0.9	0.0	1.6	1.0	1	
	150-400	<0.5	2	0.09	0.5	0.9	0.0	0.8	0.6	1	5.5
$p_{\text{free}} \rightarrow \mu^+K^0$	550-900	<0.35	1	0.14	0.8	0.9	0.0	1.6	0.8	0	
	150-350	<0.5	2	0.04	0.5	0.9	0.0	0.8	0.6	0	2.0
$p \rightarrow \nu K^+$	150-400	<0.6	1	0.07	8.3	8.4	2.9	8.2	6.9	7	0.8
$p_{\text{free}} \rightarrow \nu K^+$	150-400	<0.6	1	0.07	8.3	8.4	2.9	8.2	6.9	7	0.1
$n \rightarrow e^-K^+$	350-700	<0.5	1	0.14	4.2	5.3	1.9	4.7	4.0	5	1.6
$n \rightarrow \mu^-K^+$	200-500	<0.5	2	0.10	0.7	1.8	1.0	0.8	1.1	1	2.7
$n \rightarrow \nu\eta^0$	500-850	0.2-0.5	0	0.31	3.2	4.9	7.6	4.6	5.1	4	3.9
$p \rightarrow e^+\eta^0$	750-1150	<0.3	0	0.33	0.2	0.9	1.0	2.7	1.2	1	
	350-650	<0.5	1	0.07	4.0	4.9	1.9	4.3	3.8	5	10.8
$p_{\text{free}} \rightarrow e^+\eta^0$	750-1150	<0.25	0	0.65	0.2	0.4	0.0	2.7	0.8	1	
	350-650	<0.5	1	0.14	4.0	4.9	1.9	4.3	3.8	5	4.2
$p \rightarrow \mu^+\eta^0$	550-900	<0.4	1	0.17	1.7	0.9	0.0	1.6	1.0	1	
	200-450	<0.5	2	0.06	0.5	1.8	1.0	0.8	1.0	1	6.4
$p_{\text{free}} \rightarrow \mu^+\eta^0$	550-900	<0.35	1	0.39	0.8	0.9	0.0	1.6	0.8	0	
	200-450	<0.5	2	0.11	0.5	1.8	1.0	0.8	1.0	1	4.5
$n \rightarrow e^+\rho^-$	450-750	<0.5	0	0.41	3.2	4.0	8.6	4.0	5.0	5	4.5
$n \rightarrow \mu^+\rho^-$	250-600	<0.5	1	0.12	5.1	5.8	1.9	5.3	4.5	7	1.0
$n \rightarrow \nu\rho^0$	200-600	<0.5	0	0.07	7.6	6.7	6.7	5.2	6.5	14	0.4
$p \rightarrow e^+\rho^0$	200-450	<0.5	1	0.16	3.2	3.5	0.0	4.1	2.7	5	2.2
$p_{\text{free}} \rightarrow e^+\rho^0$	200-450	<0.5	1	0.33	3.2	3.5	0.0	4.1	2.7	5	0.9
$p \rightarrow \mu^+\rho^0$	150-450	<0.5	2	0.04	0.5	1.8	1.0	0.8	1.0	1	1.4
$p_{\text{free}} \rightarrow \mu^+\rho^0$	150-450	<0.5	2	0.07	0.5	1.8	1.0	0.8	1.0	1	0.5
$p \rightarrow \nu^+\rho^+$	200-600	<0.5	1	0.07	5.9	6.7	1.9	5.7	5.0	7	0.7
$p_{\text{free}} \rightarrow \nu^+\rho^+$	200-600	<0.5	1	0.20	5.9	6.7	1.9	5.7	5.0	7	0.4
$n \rightarrow e^-\rho^+$	450-750	<0.5	1	0.18	3.4	4.0	1.9	3.5	3.2	3	2.7
$n \rightarrow \mu^-\rho^+$	250-600	<0.5	2	0.04	0.3	1.8	1.0	1.2	1.1	1	1.1
$n \rightarrow \nu\omega^0$	600-1000	<0.4	0	0.06	1.3	3.5	4.8	4.5	3.5	2	
	150-550	<0.5	1	0.10	5.1	6.2	2.9	5.0	4.8	7	1.5
$p \rightarrow e^+\omega^0$	750-1150	<0.3	0	0.05	0.2	0.9	1.0	2.7	1.2	1	
	300-600	<0.5	1	0.16	4.2	4.9	1.9	4.3	3.8	6	2.6
$p_{\text{free}} \rightarrow e^+\omega^0$	750-1150	<0.25	0	0.07	0.2	0.4	0.0	2.7	0.8	1	
	300-600	<0.5	1	0.38	4.2	4.9	1.9	4.3	3.8	6	1.0
$p \rightarrow \mu^+\omega^0$	650-950	<0.35	1	0.03	0.5	0.4	0.0	1.5	0.6	0	
	200-450	<0.5	2	0.08	0.5	1.8	1.0	0.8	1.0	1	4.0
$p_{\text{free}} \rightarrow \mu^+\omega^0$	650-950	<0.3	1	0.05	0.3	0.4	0.0	0.3	0.3	0	
	200-450	<0.5	2	0.12	0.5	1.8	1.0	0.8	1.0	1	1.2
$n \rightarrow \nu K^{*0}$	700-950	<0.3	0	0.02	0.2	0.4	0.0	2.7	0.8	1	
	200-500	<0.5	1	0.04	3.5	5.3	0.0	4.5	3.3	6	0.7
$p \rightarrow \nu K^{*+}$	250-750	<0.5	1	0.10	5.7	6.7	1.9	7.3	5.4	8	1.0
$p_{\text{free}} \rightarrow \nu K^{*+}$	250-750	<0.5	1	0.24	5.7	6.7	1.9	7.3	5.4	8	0.5
$n \rightarrow e^-K^{*+}$	250-600	<0.5	1	0.09	5.1	5.8	1.9	5.3	4.5	7	0.7
$n \rightarrow e^+e^-\nu$	500-950	<0.5	0	0.40	4.5	4.9	8.6	6.8	6.2	6	3.8
$p \rightarrow e^+e^-\nu$	750-1150	<0.3	0	0.96	0.2	0.9	1.0	2.7	1.2	1	31.1
$p_{\text{free}} \rightarrow e^+e^-\nu$	750-1150	<0.25	0	0.82	0.2	0.4	0.0	2.7	0.8	1	5.3
$n \rightarrow \mu^+\mu^-\nu$	150-500	<0.5	2	0.12	0.7	1.8	1.0	0.8	1.1	1	3.1
$p \rightarrow \mu^+\mu^-\mu^+$	200-450	<0.4	2	0.46	0.3	0.0	0.0	0.0	0.1	0	25.3
$p_{\text{free}} \rightarrow \mu^+\mu^-\mu^+$	200-450	<0.4	2	0.62	0.3	0.0	0.0	0.0	0.1	0	6.8

As for the problem in not knowing the theoretical parameter, ρ (the ratio of bound to free decay rates), we have used method (c) described at the end of chapter 2, in which we give limits for the cases of $\rho = 0$ (equivalent to using only the free protons in water), and $\rho = 1$ (equivalent to using all protons in water, assuming the decay rates to be equal for free and bound protons). We term the two cases as “free limits,” and “water limits,” respectively:

$$\begin{aligned}\tau_f/B &= 0.2\epsilon_f \frac{t_d N_n}{S} \\ \tau_w/B &= \epsilon_w \frac{t_d N_n}{S}.\end{aligned}\tag{7.10}$$

In table (7-4) are listed the lifetime limits for all the analyzed decay modes, and included is summary of the acceptance regions, efficiencies, expected backgrounds, and candidates. We also list a mean background of the 4 estimates, and estimate an error of $\begin{smallmatrix} +100\% \\ -50\% \end{smallmatrix}$ based on the discrepancies between the various estimates.

A comparison of the number of candidates and the expected background for each mode shows no evidence for a signal in any channel. In all, we found 16 candidates for at least one decay mode with no final state neutrino, which constitutes $4.9 \pm 1.2\%$ of the total data sample. In table (7-5), we list the candidate events, their characteristics, and the modes for which they are candidates.

Conclusions. We have analyzed 37 decay modes of nucleons in water as a whole, and 17 decay modes of free protons from hydrogen in water. Although estimates in the background are rather imprecise, no obvious signal for nucleon decay has emerged from this analysis. Lifetime limits have been set in the range of 10^{31} – 10^{32} years for nucleons in water as a whole, under the assumption that direct nuclear effects (section 2.2) are negligible. With no such assumptions being necessary, limits on the free proton lifetime have been set in the range of 10^{30} – 10^{32} years. The method of this analysis served as useful for a general analysis of any decay mode, and as an initial step to set conservative limits. It is obviously deficient in

Event #	E_c (MeV)	A_c	n_μ	Source	Decay Products
299-72044	770	0.39	0	P_{free}	(none)
				P_{water}	(none)
				n_{oxygen}	$e^+\pi^-, e^-\pi^+$
420-34248	450	0.18	0	P_{free}	(none)
				P_{water}	(none)
				n_{oxygen}	$e^+\pi^-, e^-\pi^+, e^+\rho^-$
588-8320	370	0.42	2	P_{free}	$\mu^+\eta^0, \mu^+\rho^0, \mu^+\omega^0$
				P_{water}	$\mu^+\eta^0, \mu^+\rho^0, \mu^+\omega^0$
				n_{oxygen}	$\mu^-\pi^+, \mu^+K^0, \mu^-K^+, \mu^-\rho^+$
656-11673	520	0.40	0	P_{free}	(none)
				P_{water}	(none)
				n_{oxygen}	$e^+\pi^-, e^-\pi^+, e^+\rho^-$
663-1770	500	0.47	0	P_{free}	(none)
				P_{water}	(none)
				n_{oxygen}	$e^+\pi^-, e^-\pi^+, e^+\rho^-$
747-44203	339	0.47	1	P_{free}	$e^+K^0, e^+\rho^0, e^+\omega^0$
				P_{water}	$e^+K^0, e^+\rho^0, e^+\omega^0$
				n_{oxygen}	$\mu^-\pi^+, \mu^+\rho^-, e^-K^{*+}$
889-10424	280	0.27	1	P_{free}	$e^+\rho^0$
				P_{water}	$e^+\rho^0$
				n_{oxygen}	$\mu^+\pi^-, \mu^+\rho^-, e^-K^{*+}$
1047-13889	440	0.18	1	P_{free}	$e^+K^0, e^+\eta^0, e^+\rho^0, e^+\omega^0$
				P_{water}	$e^+K^0, e^+\eta^0, e^+\rho^0, e^+\omega^0$
				n_{oxygen}	$\mu^+\pi^-, e^-K^+, \mu^+\rho^-, e^-K^{*+}$
1238-48756	310	0.42	1	P_{free}	$e^+K^0, e^+\rho^0, e^+\omega^0$
				P_{water}	$e^+K^0, e^+\rho^0, e^+\omega^0$
				n_{oxygen}	$\mu^-\pi^+, e^-K^{*+}$
1238-67704	420	0.42	1	P_{free}	$e^+K^0, e^+\eta^0, e^+\rho^0, e^+\omega^0$
				P_{water}	$e^+K^0, e^+\eta^0, e^+\rho^0, e^+\omega^0$
				n_{oxygen}	$\mu^+\pi^-, e^-K^+, \mu^+\rho^-, e^-K^{*+}$
1268-63668	530	0.36	0	P_{free}	(none)
				P_{water}	(none)
				n_{oxygen}	$e^+\pi^-, e^-\pi^+, e^+\rho^-, \mu^+\rho^-$
1270-31957	540	0.44	1	P_{free}	$e^+K^0, e^+\eta^0, e^+\omega^0$
				P_{water}	$e^+K^0, e^+\eta^0, e^+\omega^0$
				n_{oxygen}	$\mu^+\pi^-, e^+K^0, e^-K^+, \mu^+\rho^-, e^-\rho^+, e^-K^{*+}$
1349-17473	590	0.17	0	P_{free}	(none)
				P_{water}	(none)
				n_{oxygen}	$e^+\pi^-, e^-\pi^+, e^+\rho^-$
1486-42698	450	0.43	1	P_{free}	$e^+K^0, e^+\eta^0, e^+\omega^0$
				P_{water}	$e^+K^0, e^+\eta^0, e^+\omega^0$
				n_{oxygen}	$\mu^+\pi^-, e^-K^+, \mu^+\rho^-, e^-\rho^+, e^-K^{*+}$
1513-31678	610	0.37	1	P_{free}	$e^+\eta^0$
				P_{water}	$\mu^+\gamma, \mu^+\pi^0, \mu^+K^0, e^+\eta^0$
				n_{oxygen}	$e^-K^+, e^-\rho^+$
1528-42652	760	0.11	0	P_{free}	$e^+\gamma, e^+\pi^0, e^+K^0, e^+\eta^0, e^+\omega^0, e^+e^-e^+$
				P_{water}	$e^+\gamma, e^+\pi^0, e^+K^0, e^+\eta^0, e^+\omega^0, e^+e^-e^+$
				n_{oxygen}	$e^+\pi^-, e^-\pi^+$

Table 7-5. Candidate events for nucleon decay with no final state neutrino as found by the visible energy, anisotropy analysis.

the sense that it uses little information on the topology of the events, and thus is not intended to be a statement of "the state of the art." Historically, when the first results of this method published,^{46,47} they were the best limits in the world—a worthy achievement in itself.

7.3 TWO-PRONG ANALYSIS⁴⁸

Of course, more information is available to us than was used in the visible energy, anisotropy analysis. In an attempt to classify events further, we have devised an algorithm to automatically select "clean," two-prong events. An excess of two-prong events in the data may indicate the presence of proton decay, of which many possible final states should give clean, wide-angle, two-prong events. Furthermore, the selection of events with well-defined tracks allows for a superior kinematic analysis, in which the invariant mass and total momentum of an event can be measured (see section 7.4.)

Decays with Two-Prongs. The reason that two-prong events are worthy of study is that a sizeable number of "allowed" exclusive final states (in the sense of equation (7.1)), would appear as two-prongs in our detector. There are five regions of center of mass energy (or, "invariant mass," M), which are important for proton decay:

- (1) The Nucleon Region, $M = 940 \text{ MeV}$ ($p \rightarrow e^+ \gamma$; $p \rightarrow \mu^+ \gamma$; $n \rightarrow e^+ \pi^-$; $n \rightarrow \mu^+ \pi^-$; $p \rightarrow e^+ \pi^0$; $p \rightarrow \mu^+ \pi^0$; $n \rightarrow e^- \pi^+$; $n \rightarrow \mu^- \pi^+$). For all of these decay modes, we do not have any inefficiency due to meson branching ratios.
- (2) The Omega Region, $M = 780 \text{ MeV}$ ($p \rightarrow \mu^+ \omega^0$; $n \rightarrow \nu \omega^0$). The ν is, of course, invisible; it turns out that the μ is below Cherenkov threshold. Observation of two-prongs results if we have $\omega \rightarrow \pi^0 \gamma$, which has a 9% branching ratio. The momentum of the ω is small enough for the $\pi^0 \gamma$ opening angle to be greater than 160° , and the π^0 is energetic enough to appear as a single prong (see section 7.4 for a detailed discussion on the

π^0 .) In the rest frame of the nucleon, the ω momentum varies between 100 MeV to 150 MeV, depending on the accompanying lepton type.

- (3) The Rho Region, $M = 770 \text{ MeV}$ ($n \rightarrow \mu^+ \rho^-$; $n \rightarrow \nu \rho^0$; $p \rightarrow \mu^+ \rho^0$; $p \rightarrow \nu \rho^+$; $n \rightarrow \mu^- \rho^+$). The uncertainty in the ρ mass leads to a less well-defined invariant mass than for the other two-prong decay modes. More significant, though, is that the efficiency for detecting two-prongs is expected to be very low on account of nuclear interactions distorting the event 90% of the time. Due to the phase space effects discussed in section 6.2, the mean ρ mass is actually 730 MeV for $\nu\rho$ modes, and 710 MeV for $\mu\rho$ modes, giving momenta in the nucleon center of mass frame of around 200 MeV.
- (4) The Eta Region, $M = 550 \text{ MeV}$ ($n \rightarrow \nu \eta^0$). The two-prong decay, $\eta \rightarrow \gamma\gamma$ has a 39% branching ratio, and has an opening angle greater than 120° . In the neutron center of mass frame, the η has a momentum 300 MeV.
- (5) The Kaon Region, $M = 500 \text{ MeV}$ ($p \rightarrow \nu K^+$, $K^+ \rightarrow \pi^+ \pi^0$; $n \rightarrow \nu K^0$, $K_S^0 \rightarrow \pi^+ \pi^- / \pi^0 \pi^0$). First, we note that the K 's are invisible until they decay. However, few of these decays appear in our detector as two prongs. The problem is due to the low pion energies of about 300 MeV:
- a) The π^\pm are heavily affected by the Cherenkov threshold, and emit less than 40 MeV visible energy, which corresponds to less than 8 tubes firing per track. This is insufficient for a reliable track reconstruction, and, in the case of $K^0 \rightarrow \pi^+ \pi^-$, the total visible energy is much lower than our analysis requirement of about 200 MeV.
- b) The $K^0 \rightarrow \pi^0 \pi^0$ opening angle is $\simeq 100^\circ$, and the $\pi^0 \rightarrow \gamma\gamma$ opening angle is $\simeq 50^\circ$. Hence the γ tracks tend to overlap, making track selection extremely difficult, and disguising the two-prong nature of the event. Also, the K momentum, $\simeq 340 \text{ MeV}$ in the nucleon rest frame, is rather high, and thus is more background limited than the other two-prong decay modes. We shall therefore not consider two-prong events as candidates

for K modes.

Selection of Two-Prongs. Our definition of a “multi-prong” event is given by equation (7.6), where the anisotropy, $A_c < 0.55$. We define the “two-prong” events as the subset of the multi-prong events which are found by the following algorithm:

- (a) All tubes within $\theta < \cos^{-1} 0.3 = 72^\circ$ of the “strongest” track direction are removed from the analysis.
- (b) The remaining tubes must define a second, single track, i.e., their anisotropy must satisfy:

$$A'_c(\text{two-prong}) > 0.55. \quad (7.11)$$

- (c) The second track must have more than 10 tubes firing “in time.” This corresponds to a track of visible energy greater than about 50 MeV.
- (d) The opening angle between the two track directions must be greater than 115° (to account for the Cherenkov angle, plus the search cone angle).

We need to define some terms used above:

- A tube firing “in time” is defined in equation (7.5).
- The direction of the second track is defined to be the energy-weighted direction to all the tubes that fire in time, and are not in the first track.
- The “strongest” track direction is found by the following iterative procedure:
 - (1) The energy-weighted direction, from the vertex, to all the tubes that fire in time, is used as the first guess.
 - (2) Only the tubes in the forward hemisphere of this direction are used to recalculate the energy-weighted direction.
 - (3) We repeat (2) until the direction does not change.
 - (4) Only the tubes within $\theta < \cos^{-1} 0.3 = 72^\circ$ of this direction are used to recalculate the energy-weighted direction.

(5) We repeat (4) until the direction does not change.

Items (1)-(3) ensure that we end up in the hemisphere with the greatest energy flux. Items (4)-(5) ensure that the first track direction has an energy distribution which independent of azimuthal angle (as it should be), and is determined solely by those tubes defined to lie in the first track.

Background/Data Comparison In the data, we find that out of 326 events reconstructed in the fiducial volume, 13 of them appear as two-prongs, which is $4.0 \pm 1.1\%$ of the data sample.

For our background estimate, we analyzed the four simulations of atmospheric neutrino interactions as described in section 6.4, and found remarkable agreement with the data, as shown in figure (7-6). The weighted mean of the estimates gives $4.1 \pm 0.3\%$, where the error bar is purely statistical. The χ^2/DOF for the four estimates from the weighted mean is 0.4, which leads us to believe that the systematic errors associated with bubble chamber liquid type, assumptions of ambiguous tracks, etc., are negligible in comparison with the statistical errors in the estimates.

We conclude, therefore, that there is no evidence for proton decay on the basis of the fraction of observed clean two-prong events. To go further, we must examine these two-prong events in detail, and compare them to the expected signal.

7.4 INVARIANT MASS, MOMENTUM ANALYSIS⁴⁸

We analyzed the kinematics of the events found by the two-prong analysis above, and found the total momentum and center of mass energy (invariant mass) of the events, under the various particle hypotheses appropriate to proton decay. The candidate requirements are much more physically obvious than, say, for visible energy and anisotropy. The expected momenta can be understood in terms of Fermi motion and simple kinematics; the invariant mass should be that

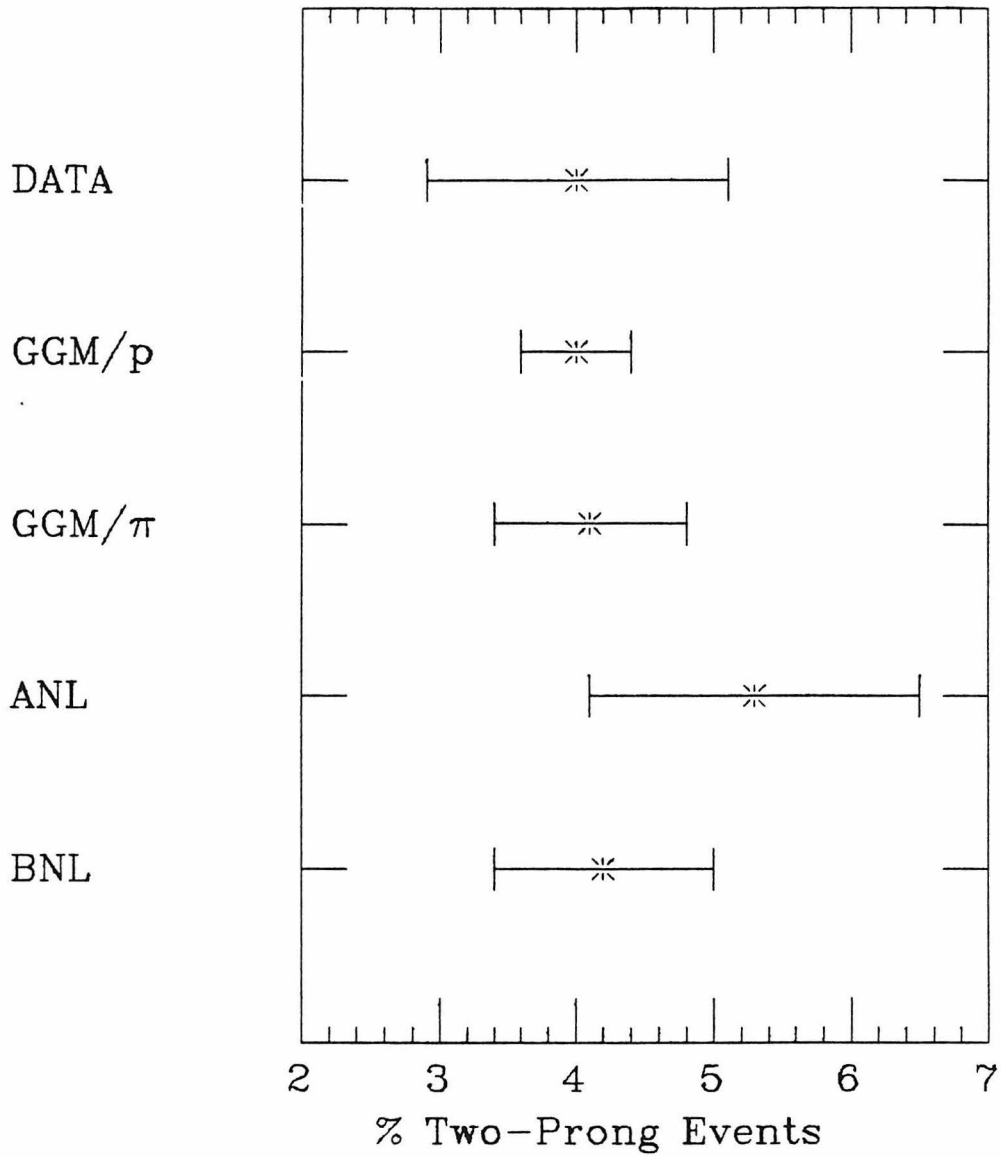


Figure 7-6. Fraction of two-prong events for the data and the simulated backgrounds. The mean background estimate is $4.1 \pm 0.3\%$, and the $\chi^2/\text{DOF} = 0.4$, indicating that statistical errors dominate over the systematic differences of the bubble chamber data.

of the appropriate decay particle. As we noted above, the appropriate decay particle need not be a nucleon at all, e.g., for $p \rightarrow \mu^+\omega$, the muon is created below Cherenkov threshold, so the invariant mass we should look for is that of the ω .

We emphasise this because the requirements we make are based on simple physical grounds, and are not as dependent upon event simulation Monte-Carlo as the visible energy, anisotropy analysis. The signal simulations were used to determine the efficiency of the procedure, and to check that the correct invariant masses and momenta were, in fact, being reconstructed well.

We then compared the results to the various background simulations, and made a background subtraction to derive lifetime limits for various decay modes.

Momentum Reconstruction Momentum reconstruction begins by assigning a visible energy to each track, E_{c1} , and E_{c2} . In doing this, care must be taken to account for the tubes which fire from scattered light ($\simeq 20\%$), because, as we noted in the discussion of anisotropy, this light contains negligible direction information. This means that we cannot, on an individual basis, associate late firing tubes with a particular track. We have devised an algorithm by which the “scattered energy,” E_{scat} , from tubes firing ± 14 ns later than expected, is assigned to a track, j , in proportion to its “direct energy,” $E_{\text{dir } j}$. This has the effect of scaling the event’s total direct energy, E_{dir} , up to its total visible energy:

$$\begin{aligned} E_{c1} &= E_{\text{dir } 1} + \left(\frac{E_{c1}}{E_c} \right) E_{\text{scat}}, \\ &= \left(\frac{E_c}{E_{\text{dir}}} \right) E_{\text{dir } 1}; \end{aligned} \quad (7.12)$$

and similarly,

$$E_{c2} = \left(\frac{E_c}{E_{\text{dir}}} \right) E_{\text{dir } 2};$$

where we have used,

$$E_{\text{dir}} = E_{\text{dir } 1} + E_{\text{dir } 2} \quad \text{and} \quad E_c = \begin{cases} E_{c1} + E_{c2}, \\ E_{\text{dir}} + E_{\text{scat}}. \end{cases}$$

We can intuitively see why this makes sense by the following reasoning: The scattered light is distributed almost isotropically into the total solid angle as seen from the event vertex, and the amount of scattering from a given track is proportional to the number of photons it generates. Therefore, the amount of energy missing from a track is proportional to its visible energy.

The next step is to assign particle types to the tracks—the hypothesis depending upon the decay mode under investigation. In table (7–6) we list the particle hypotheses we use for the two tracks. The *true* track energy, E_j , is inferred from the visible track energy, as in figure (3–1). The track momentum is then simply $\vec{p}_j = \sqrt{E_j^2 - m_j^2} \hat{x}_j$, where \hat{x}_j is in the measured direction of track j .

The total event momentum is trivially the vector sum of the track momenta:

$$\vec{P} = \sqrt{E_1^2 - m_1^2} \hat{x}_1 + \sqrt{E_2^2 - m_2^2} \hat{x}_2. \quad (7.13)$$

Under the special case that one of the particle hypotheses is a π^0 , we must take care that the expected energy deposition of $\pi^0 \rightarrow \gamma\gamma$ is consistent with our definition of a single prong. To select the consistency criteria, we first consider the following theorems concerning visible properties of the π^0 decay (see Appendix B for their derivation):

Theorem 1. *The visible energy of the decay $\pi^0 \rightarrow \gamma\gamma$ is independent of the orientation of the center of mass decay axis relative to its direction of motion, and is equal to its true energy.*

Theorem 2. *The mean direction of visible energy flux (the “direction of anisotropy”) of $\pi^0 \rightarrow \gamma\gamma$ is independent of the orientation of the center of mass decay axis relative to its direction of motion, and is in the direction of its motion.*

Theorem 3. *The anisotropy of the decay $\pi^0 \rightarrow \gamma\gamma$ is independent of the orientation of the center of mass decay axis relative to its direction of motion, and is equal to 0.75β (where β is the π^0 velocity).*

The first two theorems together provide the powerful statement that the momentum vector of a π^0 can be deduced entirely from its visible energy deposition, irrespective of its decay orientation. This is good justification for using, as a measurement of the momentum direction, the mean energy-weighted direction from the vertex to all the firing tubes. The third theorem justifies the use of anisotropy in determining the analysis requirements.

For the hypothesis that the π^0 is the first track, we must ensure that the visible energy be contained within our search cone of half opening angle, $\theta_{\text{cone}} = 72^\circ$. This implies that the decay half opening angle must be $\phi_{\gamma\gamma} < (72^\circ - 42^\circ) = 30^\circ$, which corresponds to a minimum total energy

$$E_{\pi^0} > \frac{m_{\pi^0}}{\sin \phi_{\gamma\gamma}} = 270 \text{ MeV}.$$

We actually choose to require,

$$E_{\pi^0} > 300 \text{ MeV}. \quad (7.14)$$

If the hypothesis is that the π^0 is the second track, we use the third theorem to choose the energy above which the π^0 becomes defined as a single-prong:

From theorem 3,

$$\begin{aligned} A'_c &= 0.75\beta \\ &= 0.75\sqrt{1 - (m_{\pi^0}/E_{\pi^0})^2}. \end{aligned}$$

But, by equation (7.11),

$$A'_c > 0.55;$$

therefore,

$$E_{\pi^0} > 200 \text{ MeV}. \quad (7.15)$$

In summary, we require:

$$E_{\pi^0} > \begin{cases} 300 \text{ MeV,} & \text{for the first track hypothesis;} \\ 200 \text{ MeV,} & \text{for the second track hypothesis.} \end{cases} \quad (7.16)$$

1st Track	2nd Track	Decay Modes
e^\pm/γ	e^+/γ	$p \rightarrow e^+\gamma, n \rightarrow \nu\eta^0$
e^\pm/γ	$\pi^0(E > 200 \text{ MeV})$	$p \rightarrow e^+\pi^0, p \rightarrow \nu\omega^0, p \rightarrow \mu^+\omega^0$
e^\pm/γ	π^\pm	$n \rightarrow e^\mp\pi^\pm$
e^\pm/γ	μ^\pm	$p \rightarrow \mu^+\gamma$
μ^\pm	π^\pm	$n \rightarrow \mu^\mp\pi^\pm$
$\pi^0(E > 300 \text{ MeV})$	μ^\pm	$p \rightarrow \mu^+\pi^0$
$\pi^0(E > 300 \text{ MeV})$	π^\pm	$p \rightarrow \nu\rho^+, n \rightarrow \mu^\mp\rho^\pm$
π^\pm	π^\pm	$n \rightarrow \nu\rho^0, p \rightarrow \mu^+\rho^0$

Table 7-6. Particle hypotheses for two-body nucleon decays. The strongest track is determined by an algorithm described in section 7.3 under "Selection of Two-Prongs." Use this table when referring to figures (7-8) and (7-9).

Invariant Mass Reconstuction Once the energy and momenta of the two-prongs have been found under specific particle hypotheses, the event kinematics are fully defined, and the center of mass energy, or “invariant mass” can be found using the formula:

$$M = \sqrt{(E_1 + E_2)^2 - |\vec{p}_1 + \vec{p}_2|^2}. \quad (7.17)$$

If the two tracks are actually the result of the decay of some particle, then we would expect the invariant mass to be reconstructed at that particle’s mass. Any peaks in the event rate at known particle masses in the invariant mass distribution at the masses of the known particles below 1 GeV, could be indicative of proton decay, particularly if these events also have a low momentum.

Expected Signal/Background Comparison In figure (7-7), we show the results of the invariant mass and momentum reconstruction under various particle hypotheses, for some of the simulated proton decays; in figure (7-8) we show one of the background simulations —the Gargamelle (proton option) data is used here as an example. We see that for the background, the reconstructed momentum is high for high invariant mass. This arises because the opening angle distribution is peaked at the lower angle cut of 115°.

In contrast, the simulated proton decays give low reconstructed momenta with the invariant mass appropriately confined, depending on the decay mode. We note that the successful reconstruction of invariant mass and momentum for simulated decays at their physically expected values gives us confidence that the procedure works well.

To procede with a search for a signal, we decided to count the number of real data candidates for individual decay modes, which satisfy certain requirements in invariant mass and momentum (“*M-P* requirements”), and to compare this number with that expected of the background. These requirements were chosen by taking into account the following general considerations:

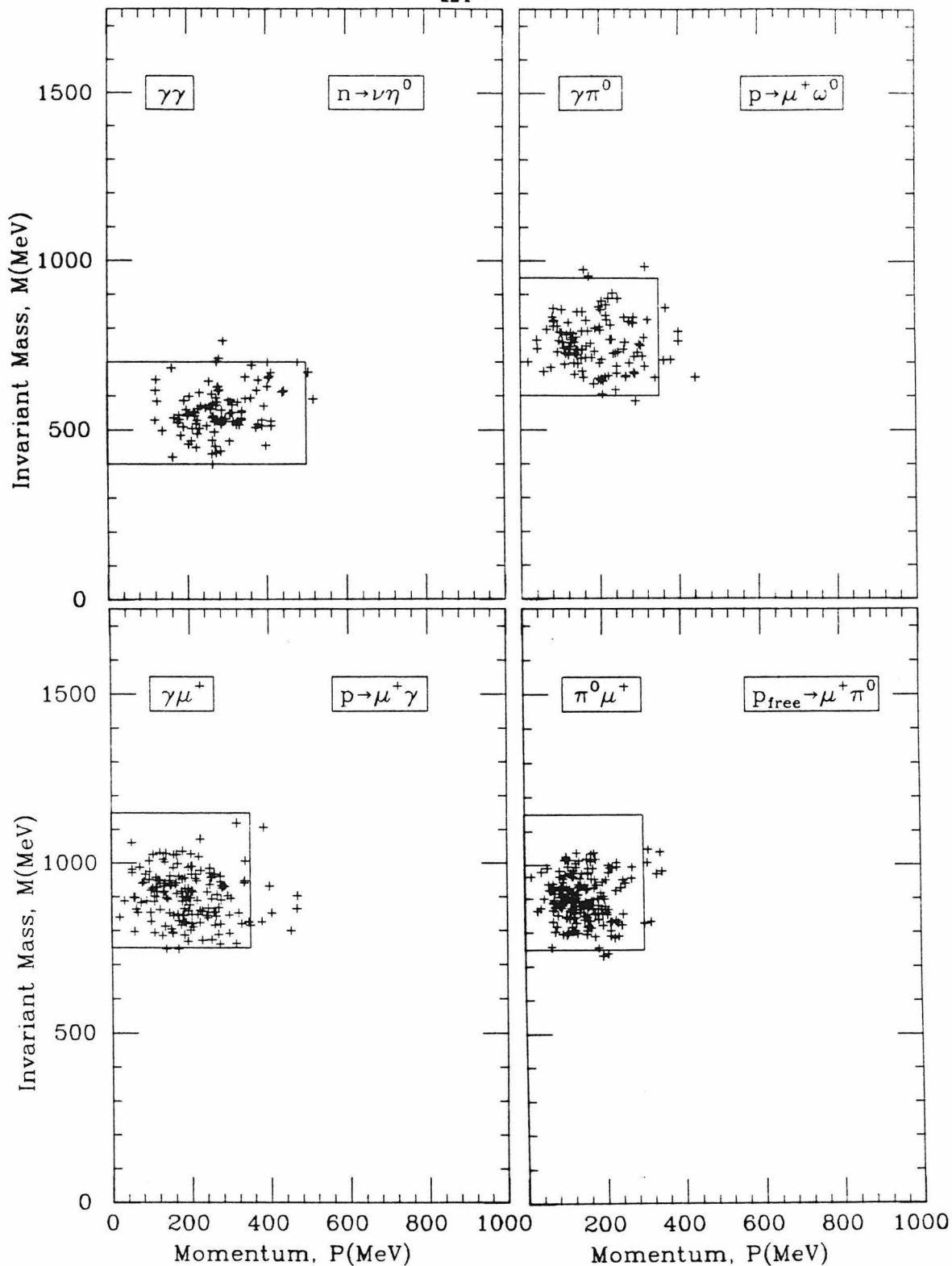


Figure 7-7. Event distributions in the M - P plane for some of the signal simulations.

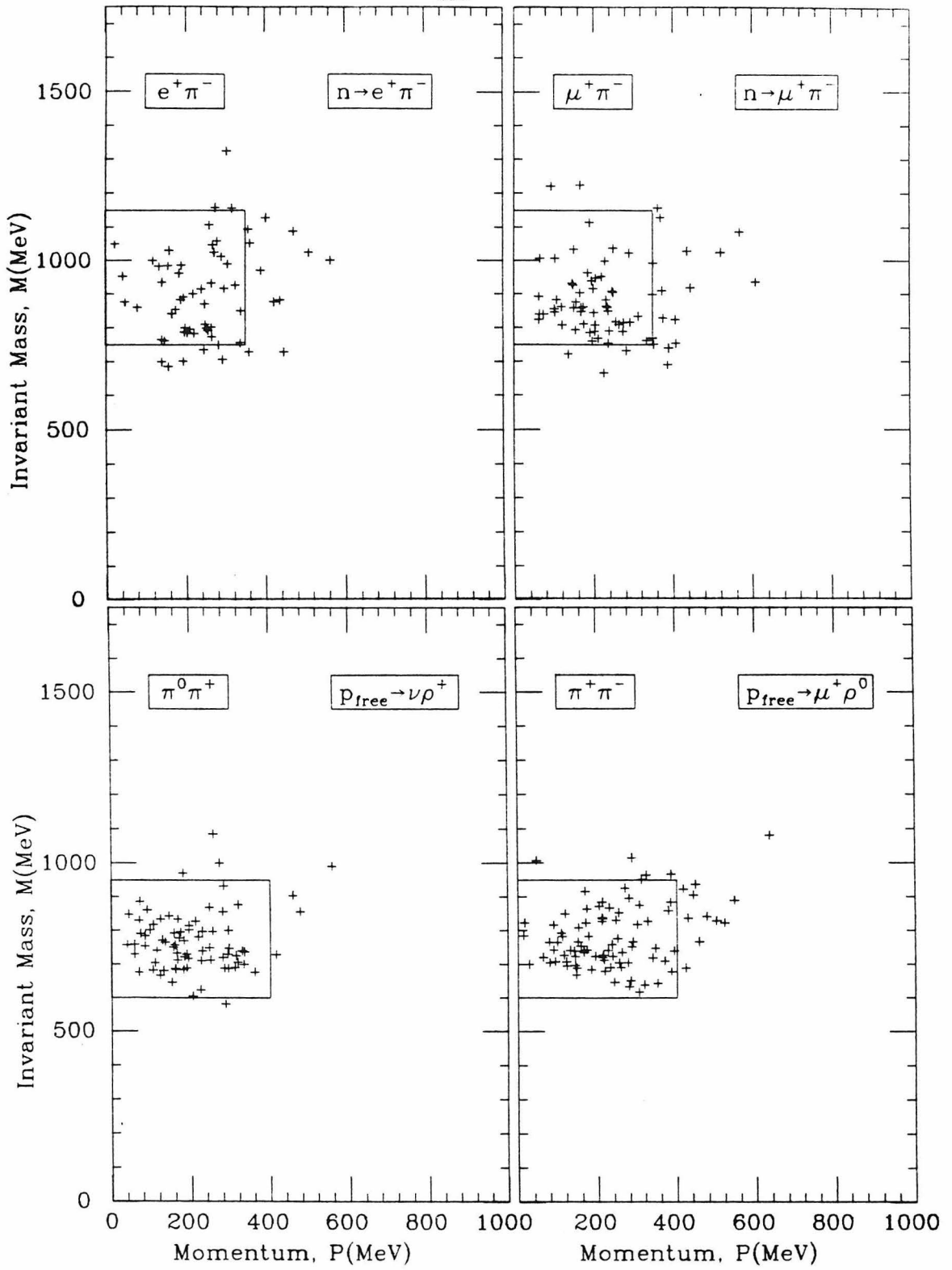


Figure 7-7. (continued).

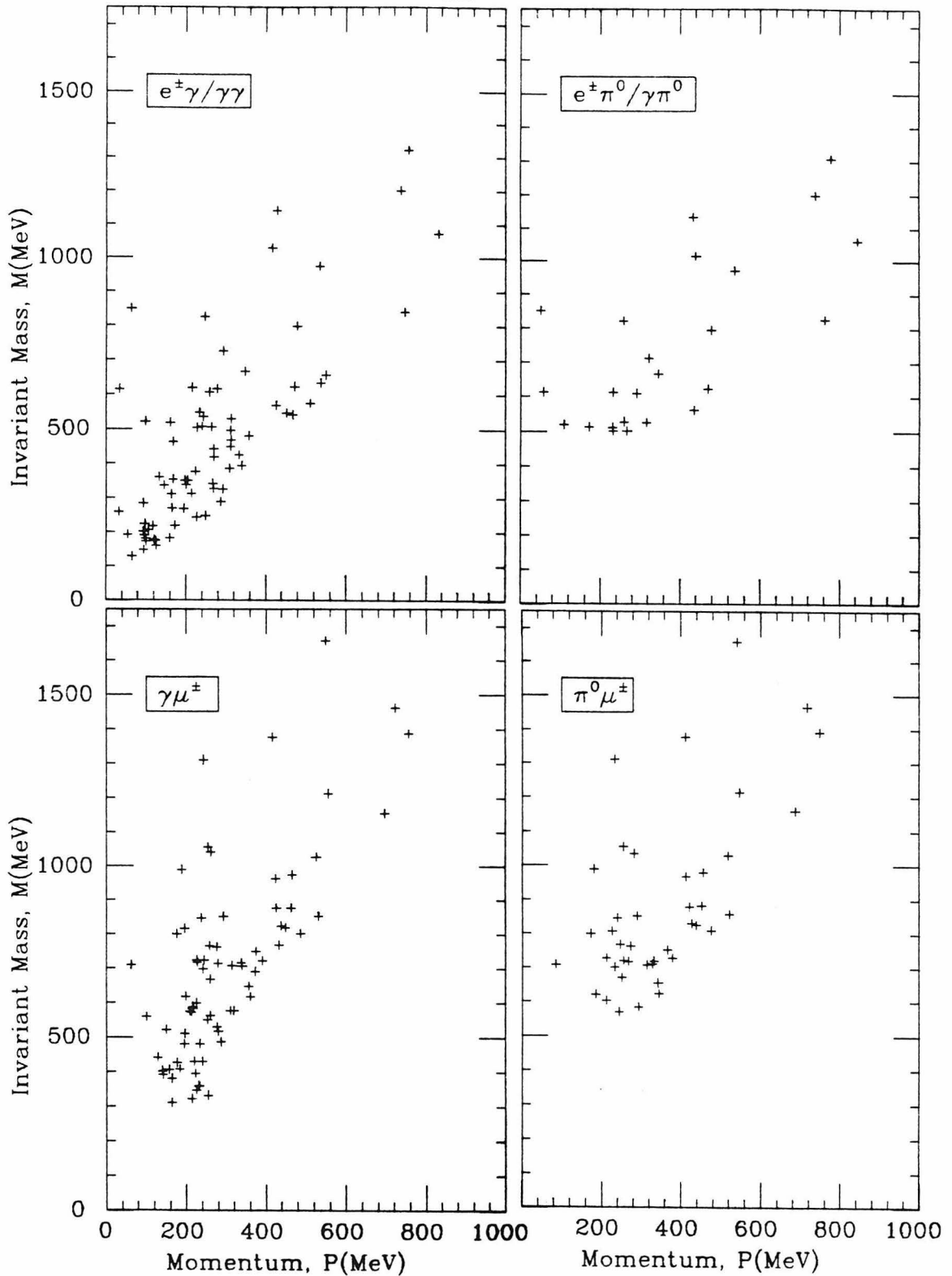


Figure 7-8. Event distributions in the M - P plane for simulated background under all possible particle hypotheses (see table (7-6)). These plots use the GGM/ p file, with an equivalent of about 6 times the analyzed livetime for the real data.

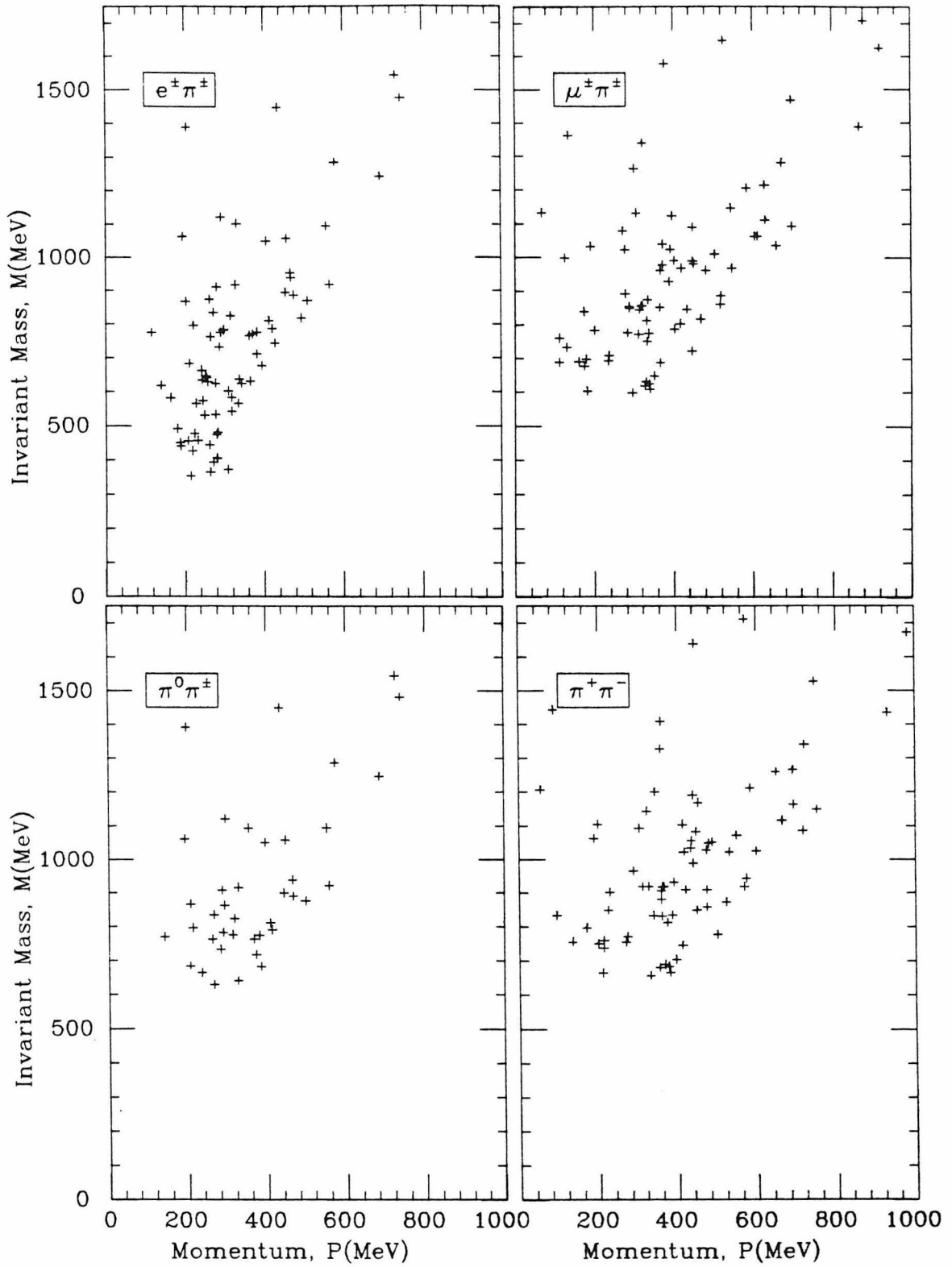


Figure 7-8. (continued).

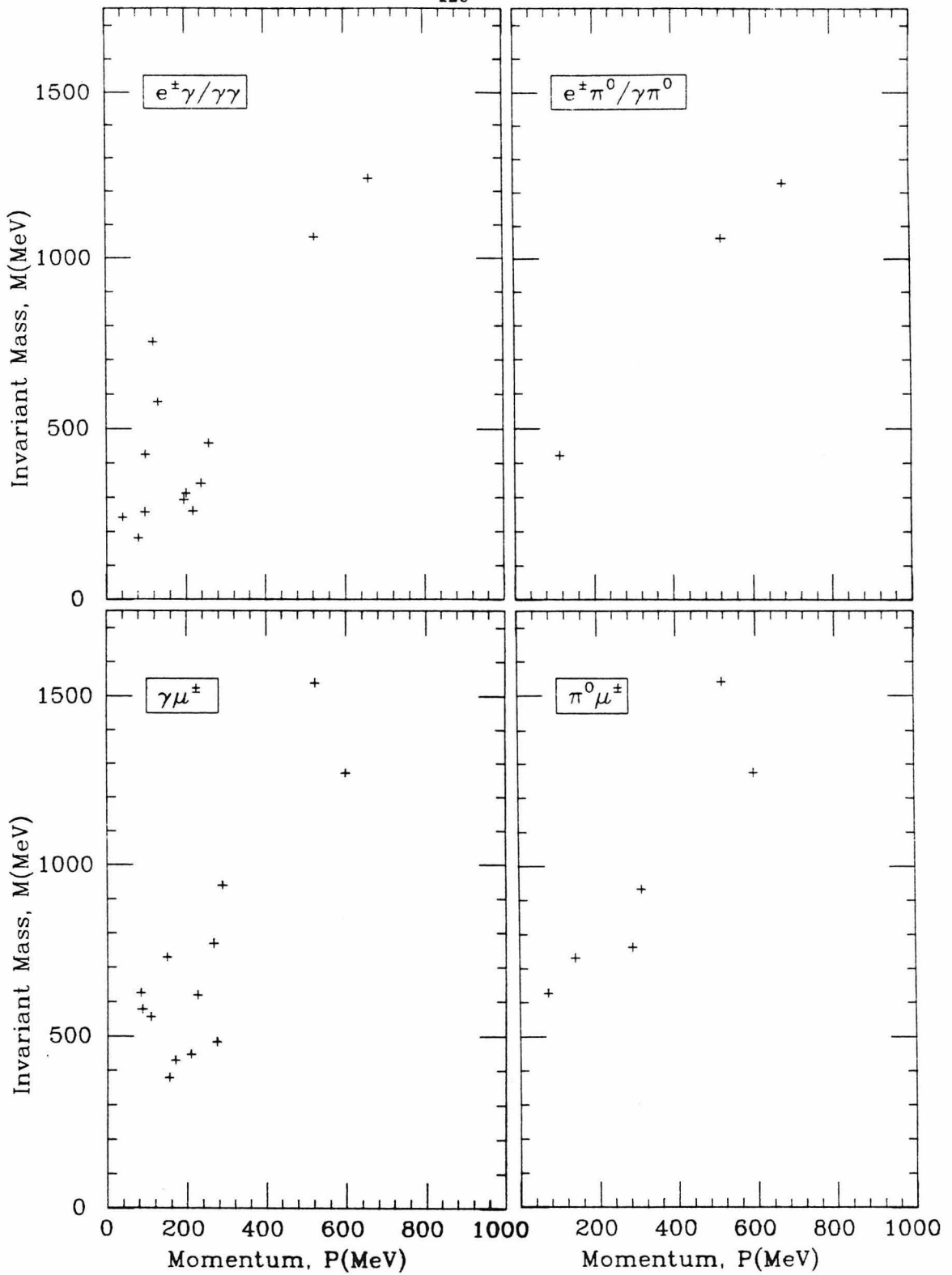


Figure 7-9. Event distributions in the M - P plane for the real data under all possible particle hypotheses (see table (7-6)).

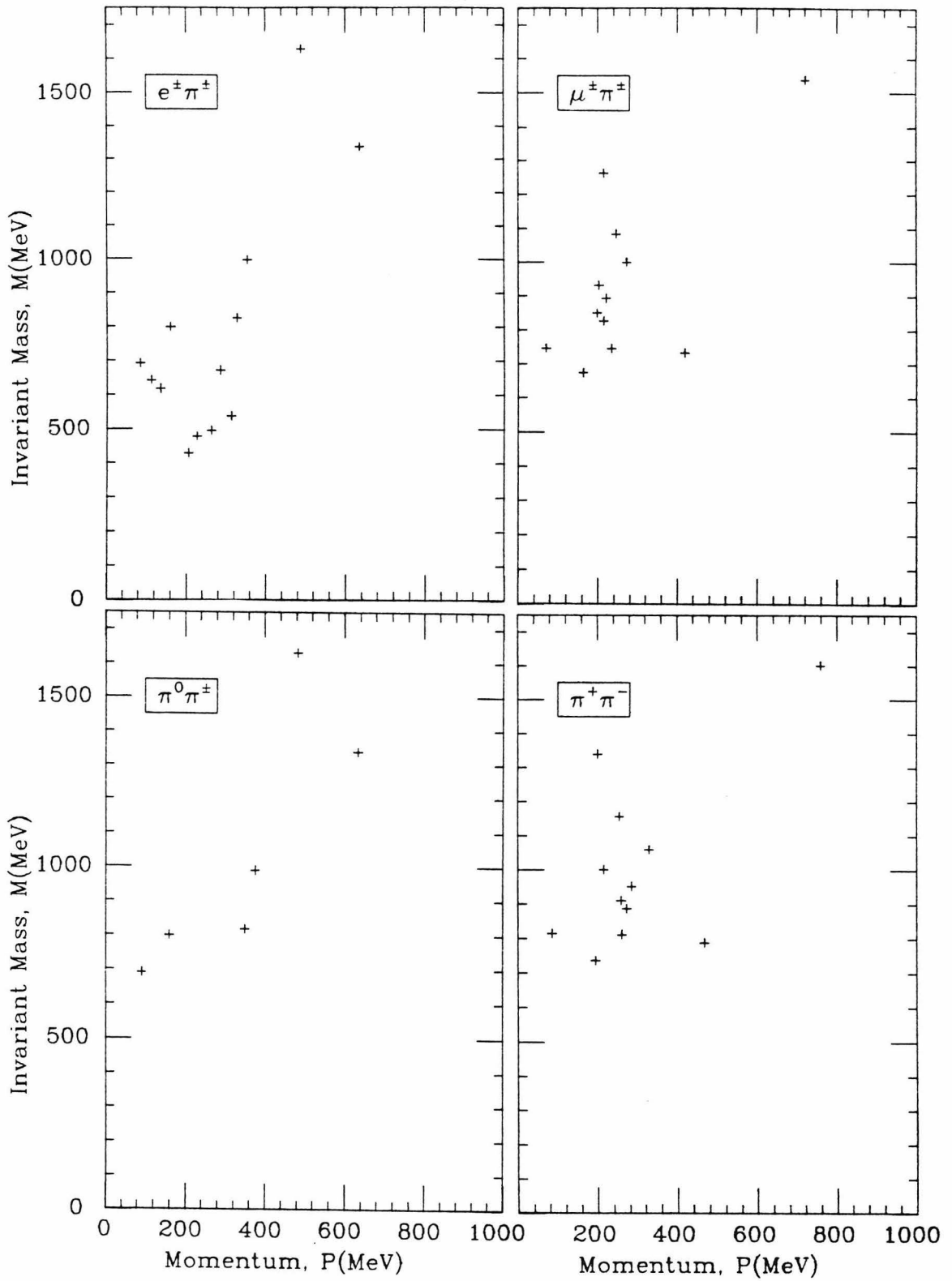


Figure 7-9. (continued).

- (a) The agreement the four background simulations in the M - P plane is consistent with pure statistics. For the requirements and hypotheses we actually used, the χ^2/DOF for most of the estimates were less than 1. We conclude that the systematic error in using the weighted mean of the estimates is small, and therefore, we believe our background estimate to be correct to within the quoted (statistical) error bars.
- (b) In the discussion following equation (3.6), we pointed out that if we wanted the best possible sensitivity in an analysis, then maximizing the signal acceptance, ϵ , was more important than minimizing the number of expected background, N_b , *provided* we have a good estimate of the expected background. Since we believe that we do have a good estimate (see (a)), our M - P requirements were chosen to accept almost all of the simulated signal which satisfied the two-prong criteria.
- (c) As we alluded to in section 7.3, we expect the reconstructed momentum distributions to be slightly dependent upon the decay mode because of simple kinematic considerations; for example, in the case of the ρ , its momentum in the nucleon frame is comparable to the nucleon’s fermi momentum. Also, momentum requirements for free proton decay can be more stringent due to the lack of fermi momentum. Table (7-7) lists the requirements, which vary between 300 MeV ($p_{\text{free}} \rightarrow \ell + \pi/\gamma$) to 500 MeV ($n \rightarrow \nu\eta$). We note that for multi-pronged events in general, the error in the momentum is due to both collection statistics, and to reconstruction systematics. The momentum is extremely insensitive to the hidden systematic error in the absolute energy calibration constant, since the errors from each track would tend to cancel each other.
- (d) The reconstructed invariant masses of the signal simulation are indeed reconstructed correctly in the mean, indicating that any hidden systematic error in the mean of M would be due to a systematic error in the absolute energy calibration constant. As we reasoned in the discussion preceding

Decay Mode	Invariant Mass M (MeV)	Momentum P (MeV)
$p \rightarrow e^+ \gamma$	750-1150	<350
$p_{\text{free}} \rightarrow e^+ \gamma$	750-1150	<300
$p \rightarrow \mu^+ \gamma$	750-1150	<350
$p_{\text{free}} \rightarrow \mu^+ \gamma$	750-1150	<300
$n \rightarrow e^+ \pi^-$	750-1150	<350
$n \rightarrow \mu^+ \pi^-$	750-1150	<350
$p \rightarrow e^+ \pi^0$	750-1150	<350
$p_{\text{free}} \rightarrow e^+ \pi^0$	750-1150	<300
$p \rightarrow \mu^+ \pi^0$	750-1150	<350
$p_{\text{free}} \rightarrow \mu^+ \pi^0$	750-1150	<300
$n \rightarrow e^- \pi^+$	750-1150	<350
$n \rightarrow \mu^- \pi^+$	750-1150	<350
$n \rightarrow \nu \eta^0$	400-700	<500
$n \rightarrow \mu^+ \rho^-$	600-950	<400
$n \rightarrow \nu \rho^0$	600-950	<450
$p \rightarrow \mu^+ \rho^0$	600-950	<400
$p_{\text{free}} \rightarrow \mu^+ \rho^0$	600-950	<400
$p \rightarrow \nu \rho^+$	600-950	<450
$p_{\text{free}} \rightarrow \nu \rho^+$	600-950	<400
$n \rightarrow \mu^- \rho^+$	600-950	<400
$n \rightarrow \nu \omega^0$	600-950	<400
$p \rightarrow \mu^+ \omega^0$	600-950	<350
$p_{\text{free}} \rightarrow \mu^+ \omega^0$	600-950	<350

Table 7-7. Invariant mass, momentum requirements for two-body decay modes.

equation (7.4), the fractional systematic error in the total energy is

$$\frac{\sigma_{\text{sys}}(E)}{E} < 15\%. \quad (7.4)$$

Because the signal distribution would have a small momentum compared to its invariant mass, we estimate the fractional systematic error in the mean of M to be about 15%. We have chosen acceptance windows of about $\pm 20\%$ around the appropriate values of M , taking the conservative approach of not being sensitive to a hidden systematic error, and, due to the smaller statistical error in M (see equation (7.2)), this gives the wide signal acceptance we wanted (see (b) above). The actual requirements are listed in table (7-7).

In table (7-8) we breakdown the efficiency for each proton decay mode under consideration, listing the meson branching ratio, the detection efficiency, the two-prong efficiency, the M - P efficiency, and the total product efficiency. The efficiencies are given for both free proton decay, ϵ_f , and for proton decay in water as a whole, ϵ_w , which is given under the assumption that the theoretical parameter, $\rho = 1$ (see equation (2.6).)

Background/Data Comparison. In figure (7-9) we show the results of the M - P reconstruction for the real data under the various particle hypotheses, to be compared with figure (7-8), which is an example of the simulated background, derived from the GGM/ p -option. Out of the 13 selected two-prong events, 10 were found to be candidates for at least one decay mode. This constitutes $10/326 = 3.1 \pm 1.0\%$ of the total data sample. We list the 10 candidate events, their various properties, and the modes for which they are candidates in table (7-9).

The level of the expected background for the four estimates are listed in table (7-10). The background estimates are in good agreement with each other, and give a weighted mean of $3.1 \pm 0.3\%$, with a χ^2/DOF of 0.5. We conclude

Decay Mode	Meson Branching Ratio	Detection Efficiency ϵ_r	Two Prong Efficiency ϵ_t	M-P Efficiency ϵ_M	Total Efficiency ϵ
$p \rightarrow e^+ \gamma$	1	0.93	0.98	0.91	0.83
$p_{\text{free}} \rightarrow e^+ \gamma$	1	0.95	1	0.96	0.91
$p \rightarrow \mu^+ \gamma$	1	0.80	0.98	0.95	0.74
$p_{\text{free}} \rightarrow \mu^+ \gamma$	1	0.90	0.99	0.97	0.87
$n \rightarrow e^+ \pi^-$	1	0.82	0.45	0.67	0.25
$n \rightarrow \mu^+ \pi^-$	1	0.77	0.47	0.72	0.26
$p \rightarrow e^+ \pi^0$	1	0.90	0.58	0.87	0.46
$p_{\text{free}} \rightarrow e^+ \pi^0$	1	0.88	0.98	0.97	0.84
$p \rightarrow \mu^+ \pi^0$	1	0.79	0.60	0.87	0.41
$p_{\text{free}} \rightarrow \mu^+ \pi^0$	1	0.92	0.98	0.95	0.87
$n \rightarrow e^- \pi^+$	1	0.91	0.32	0.67	0.20
$n \rightarrow \mu^- \pi^+$	1	0.81	0.55	0.71	0.32
$n \rightarrow \nu \eta^0$	0.38	0.91	0.43	0.94	0.14
$n \rightarrow \mu^+ \rho^-$	1	0.61	0.07	0.67	0.03
$n \rightarrow \nu \rho^0$	1	0.27	0.18	0.71	0.04
$p \rightarrow \mu^+ \rho^0$	1	0.28	0.25	0.73	0.05
$p_{\text{free}} \rightarrow \mu^+ \rho^0$	1	0.34	0.43	0.82	0.12
$p \rightarrow \nu \rho^+$	1	0.65	0.13	0.92	0.08
$p_{\text{free}} \rightarrow \nu \rho^+$	1	0.98	0.19	0.90	0.16
$n \rightarrow \mu^- \rho^+$	1	0.59	0.08	0.80	0.04
$n \rightarrow \nu \omega^0$	0.09	0.88	0.76	0.92	0.05
$p \rightarrow \mu^+ \omega^0$	0.09	0.89	0.64	0.87	0.04
$p_{\text{free}} \rightarrow \mu^+ \omega^0$	0.09	0.88	0.97	0.94	0.07

Table 7-8. Detection efficiencies for two-body nucleon decay modes.

Event	E_{c_1} (MeV)	E_{c_2} (MeV)	Angle	M (MeV)	P (MeV)	Decay Modes
141-12931	270	83	157°	830	220	$n \rightarrow \mu^\pm \pi^\mp$
				890	270	$n \rightarrow \nu \rho^0, p \rightarrow \mu^+ \rho^0$
588-8230	280	88	162°	850	200	$n \rightarrow \mu^\pm \pi^\mp$
				910	260	$n \rightarrow \nu \rho^0, p/p_{\text{free}} \rightarrow \mu^+ \rho^0$
656-11673	380	142	157°	800	160	$n \rightarrow e^\pm \pi^\mp, p/p_{\text{free}} \rightarrow \nu \rho^+, n \rightarrow \mu^\pm \rho^\mp$
				460	260	$n \rightarrow \nu \eta^0$
846-29750	130	66	151°	740	190	$n \rightarrow \nu \rho^0, p/p_{\text{free}} \rightarrow \mu^+ \rho^0$
889-10424	160	110	143°	810	260	$n \rightarrow \nu \rho^0, p/p_{\text{free}} \rightarrow \mu^+ \rho^0$
1047-13889	230	200	155°	930	200	$n \rightarrow \mu^\pm \pi^\mp$
				430	98	$n \rightarrow \nu \eta^0$
1153-38524	140	110	169°	810	85	$n \rightarrow \nu \rho^0, p/p_{\text{free}} \rightarrow \mu^+ \rho^0$
1238-67704	330	91	166°	890	220	$n \rightarrow \mu^\pm \pi^\mp$
				690	92	$p/p_{\text{free}} \rightarrow \mu \rho^+, n \rightarrow \mu^\pm \rho^\mp$
1349-17473	300	290	155°	770	270	$p/p_{\text{free}} \rightarrow \mu^+ \gamma$
				830	330	$n \rightarrow e^\pm \pi^\mp$
				1080	250	$n \rightarrow \mu^\pm \rho^\mp$
				760	290	$p/p_{\text{free}} \rightarrow \mu^+ \pi^0$
				820	350	$p/p_{\text{free}} \rightarrow \mu \rho^+, n \rightarrow \mu^\pm \rho^\mp$
				580	130	$n \rightarrow \nu \eta^0$
1528-42652	360	401	163°	940	290	$p/p_{\text{free}} \rightarrow \mu^+ \pi^0$
				930	310	$p \rightarrow \mu^+ \pi^0$
				750	120	$p/p_{\text{free}} \rightarrow e^+ \gamma$
				750	110	$p/p_{\text{free}} \rightarrow e^+ \pi^0, p/p_{\text{free}} \rightarrow \mu^+ \omega^0, n \rightarrow \nu \omega^0$

Table 7-9. Two-prong data events with their measured characteristics, and the decay modes for which they are candidates in the invariant mass, momentum analysis.

	Fraction
GGM/ p	$3.3 \pm 0.4\%$
GGM/ π	$3.0 \pm 0.6\%$
ANL	$2.3 \pm 0.8\%$
BNL	$3.3 \pm 0.7\%$
Mean	$3.1 \pm 0.3\%$
(Real Data	$3.1 \pm 1.0\%$)

Table 7-10. Two-prong background estimates for the total number of candidates in the invariant mass, momentum analysis.

that there is no evidence for proton decay on the basis of the total fraction of two-prong candidates in the total sample.

Next, we looked at the individual decay modes to search for any significant excess of candidates. In table (7-11) we list for every decay mode, the four background estimates, the weighted average and the number of data events which are candidates. The error in the number of candidates has been taken to be the 68.2% symmetric confidence window assuming Poisson statistics. The error in the background estimate has been calculated using the procedure recommended by the particle data group,⁸⁷ in which one sigma Gaussian error bars are used, with the modification that they are (conservatively) renormalized if the χ^2/DOF of the various estimates is greater than one.

We also list the difference between the mean background estimate and the fraction of candidates, in units of sigma. We conclude that there is no significant evidence for proton decay on the basis of the fraction of candidates for individual two-prong decay modes.

Decay Mode	GGM/p %	GGM/ π %	ANL %	BNL %	Mean %	Mean #	Candidates #
$p \rightarrow e^+ \gamma$	0.10 ± 0.08	0.14 ± 0.19	0 ± 0.34	0.62 ± 0.45	0.11 ± 0.07	0.37 ± 0.23	1
$p_{\text{free}} \rightarrow e^+ \gamma$	0.10 ± 0.08	0.14 ± 0.19	0 ± 0.34	0.62 ± 0.45	0.11 ± 0.07	0.37 ± 0.23	1
$p \rightarrow \mu^+ \gamma$	0.46 ± 0.16	0.82 ± 0.34	0.88 ± 0.54	1.2 ± 0.5	0.60 ± 0.13	1.9 ± 0.4	2
$p_{\text{free}} \rightarrow \mu^+ \gamma$	0.46 ± 0.16	0.54 ± 0.29	0.58 ± 0.46	0.68 ± 0.47	0.50 ± 0.13	1.6 ± 0.4	2
$n \rightarrow e^+ \pi^-$	0.77 ± 0.20	0.68 ± 0.32	0.88 ± 0.54	0.77 ± 0.48	0.76 ± 0.15	2.5 ± 0.5	2
$n \rightarrow \mu^+ \pi^-$	1.1 ± 0.2	0.82 ± 0.34	0.88 ± 0.54	0.63 ± 0.42	0.92 ± 0.17	3.0 ± 0.6	6
$p \rightarrow e^+ \pi^0$	0.10 ± 0.08	0.27 ± 0.21	0 ± 0.34	0.62 ± 0.45	0.13 ± 0.07	0.42 ± 0.23	1
$p_{\text{free}} \rightarrow e^+ \pi^0$	0.10 ± 0.08	0.14 ± 0.19	0 ± 0.34	0.62 ± 0.45	0.11 ± 0.07	0.37 ± 0.23	1
$p \rightarrow \mu^+ \pi^0$	0.46 ± 0.16	0.82 ± 0.34	0.88 ± 0.54	0.94 ± 0.49	0.58 ± 0.13	1.9 ± 0.4	2
$p_{\text{free}} \rightarrow \mu^+ \pi^0$	0.46 ± 0.16	0.54 ± 0.29	0.58 ± 0.46	0.63 ± 0.47	0.50 ± 0.13	1.6 ± 0.4	1
$n \rightarrow e^- \pi^+$	0.77 ± 0.20	0.68 ± 0.32	0.88 ± 0.54	0.77 ± 0.48	0.76 ± 0.15	2.5 ± 0.5	2
$n \rightarrow \mu^- \pi^+$	1.1 ± 0.2	0.82 ± 0.34	0.88 ± 0.54	0.63 ± 0.42	0.92 ± 0.17	3.0 ± 0.6	6
$n \rightarrow \nu \eta^0$	1.3 ± 0.3	1.2 ± 0.4	2.1 ± 0.8	1.4 ± 0.5	1.3 ± 0.2	4.4 ± 0.6	3
$n \rightarrow \mu^+ \rho^-$	1.1 ± 0.2	0.82 ± 0.34	1.2 ± 0.6	0.96 ± 0.45	1.0 ± 0.2	3.3 ± 0.6	3
$n \rightarrow \nu \rho^0$	1.6 ± 0.3	1.2 ± 0.4	0.29 ± 0.40	0.74 ± 0.42	1.1 ± 0.28	3.5 ± 0.9	5
$p \rightarrow \mu^+ \rho^0$	1.5 ± 0.3	1.2 ± 0.4	0.29 ± 0.40	0.53 ± 0.41	0.99 ± 0.18	3.2 ± 0.6	5
$p_{\text{free}} \rightarrow \mu^+ \rho^0$	1.5 ± 0.3	1.2 ± 0.4	0.29 ± 0.40	0.53 ± 0.41	0.99 ± 0.18	3.2 ± 0.6	5
$p \rightarrow \nu \rho^+$	1.1 ± 0.2	0.82 ± 0.34	1.5 ± 0.7	1.3 ± 0.4	1.1 ± 0.2	3.5 ± 0.6	3
$p_{\text{free}} \rightarrow \nu \rho^+$	1.1 ± 0.2	0.82 ± 0.34	1.2 ± 0.6	0.96 ± 0.45	1.0 ± 0.2	3.3 ± 0.6	3
$n \rightarrow \mu^- \rho^+$	1.1 ± 0.2	0.82 ± 0.34	1.2 ± 0.6	0.96 ± 0.45	1.0 ± 0.2	3.3 ± 0.6	3
$n \rightarrow \nu \omega^0$	0.41 ± 0.15	0.68 ± 0.32	0.29 ± 0.40	1.2 ± 0.5	0.49 ± 0.12	1.6 ± 0.4	1
$p \rightarrow \mu^+ \omega^0$	0.41 ± 0.15	0.54 ± 0.29	0.29 ± 0.40	1.1 ± 0.5	0.47 ± 0.12	1.5 ± 0.4	1
$p_{\text{free}} \rightarrow \mu^+ \omega^0$	0.41 ± 0.15	0.54 ± 0.29	0.29 ± 0.40	1.1 ± 0.5	0.47 ± 0.12	1.5 ± 0.4	1

Table 7-11. Background estimates, and number of candidates for nucleon decay modes in the invariant mass, momentum analysis.

Background Subtraction Since we do not have significant evidence for a signal, we have chosen to give the results of our analysis in terms of 90% confidence limits on the partial lifetimes, which we will derive in the next subsection. Before doing that, however, we will explain the procedure we used to make a background subtraction from the number of candidates.

For the expected number of background events for each decay mode, we use the weighted mean estimate in table (7-11) scaled to the total number of observed events, giving $N_b \pm \sigma_b$ events, where we make the simplest assumption that the four background estimates are Gaussianly distributed.

We first write down the formula which defines the observed signal, N_s , in terms of the number of candidates, N_c , and the number of background events, N_b :

$$N_s = N_c - N_b. \quad (7.18)$$

The mean quantities are trivially related in the same way. Now, in order to find 90% confidence limits on the lifetimes, we must solve the following equation for the upper limit on the signal, U_s :

$$Q(\bar{N}_s > U_s) = 10\%,$$

or,

$$Q(\bar{N}_c > U_s + \bar{N}_b) = 10\%, \quad (7.19)$$

where we must first determine the form of the probability distribution, Q . If \bar{N}_b were known with certainty, then finding Q would reduce to the problem in Poisson statistics of section 7.2. Since this is not the case, we break Q up as follows:

$$Q = \int R(\bar{N}_c > U_s + x)G(x, \bar{N}_b) dx, \quad (7.20)$$

where G is the distribution of estimate in the mean number of background events, x , which we are assuming to be a Gaussian with a best estimate, \bar{N}_b , and a sigma, σ_b . R can be calculated using Poisson statistics. We must include the conditional probability that the mean number of candidates be greater than or equal to the mean number of background events; i.e., $R(\bar{N}_c > x) = 1$. If we denote $P(i, \bar{N}_c)$ to be the Poisson distribution of a variable, i , with a mean, \bar{N}_c , then R is the following function of the actual number of observed candidates, N_c :

$$\begin{aligned}
 R &= \int_{U_s+x}^{\infty} P(N_c, \bar{N}_c) d\bar{N}_c / \int_x^{\infty} P(N_c, \bar{N}_c) d\bar{N}_c \\
 &= \int_{U_s+x}^{\infty} \frac{\bar{N}_c^{N_c} e^{-\bar{N}_c}}{N_c!} d\bar{N}_c / \int_x^{\infty} \frac{\bar{N}_c^{N_c} e^{-\bar{N}_c}}{N_c!} d\bar{N}_c \\
 &= \sum_{i=0}^{N_c} \frac{(U_s+x)^i e^{-(U_s+x)}}{i!} / \sum_{i=0}^{N_c} \frac{x^i e^{-x}}{i!} \\
 &= \sum_{i=0}^{N_c} P(i, U_s+x) / \sum_{i=0}^{N_c} P(i, x).
 \end{aligned} \tag{7.21}$$

Hence, we must solve for U_s :

$$\int_0^{\infty} \frac{\sum_{i=0}^{N_c} P(i, U_s+x)}{\sum_{i=0}^{N_c} P(i, x)} G(x, \bar{N}_b) dx = 10\%. \tag{7.22}$$

In practice, however, G cannot be perfectly Gaussian because, for example, we cannot have a negative background estimate. We limit the above integration to positive background estimates, taking care to ensure correct normalization. We solved this equation numerically using the binary search technique. We note that, for the special case of making *no* background subtraction, i.e., $\bar{N}_b = 0$ and $\sigma_b = 0$, the problem reduces to the one of simple Poisson 90% confidence limits (c.f. equation (7.8)):

$$\begin{aligned}
 U_s(\bar{N}_b = \sigma_b = 0) &= U_c, \\
 \sum_{i=0}^{N_c} P(i, U_c) &= 10\%.
 \end{aligned} \tag{7.23}$$

Decay Mode	Number of Candidates	Expected Background	Measured Signal	Strength of Signal	90% C.L. Limit on Candidates	90% C.L. Limit on Signal
	N_c	$N_b \pm \sigma_b$	$N_s \pm \sigma_s$	N_s/σ_s	U_c	U_s
$p \rightarrow e^+ \gamma$	1	0.37 ± 0.23	0.63 ± 1.4	0.5	3.9	3.6
$p_{\text{free}} \rightarrow e^+ \gamma$	1	0.37 ± 0.23	0.63 ± 1.4	0.5	3.9	3.6
$p \rightarrow \mu^+ \gamma$	2	1.9 ± 0.4	0.1 ± 1.6	0.1	5.3	3.9
$p_{\text{free}} \rightarrow \mu^+ \gamma$	2	1.6 ± 0.4	0.4 ± 1.6	0.3	5.3	4.1
$n \rightarrow e^+ \pi^-$	2	2.5 ± 0.5	-0.5 ± 1.7	-0.3	3.8	3.7
$n \rightarrow \mu^+ \pi^-$	6	3.0 ± 0.6	3.0 ± 2.6	1.2	11	7.7
$p \rightarrow e^+ \pi^0$	1	0.42 ± 0.23	0.6 ± 1.4	0.4	3.9	3.6
$p_{\text{free}} \rightarrow e^+ \pi^0$	1	0.37 ± 0.23	0.6 ± 1.4	0.5	3.9	3.6
$p \rightarrow \mu^+ \pi^0$	2	1.9 ± 0.4	0.1 ± 1.6	0.1	5.3	3.9
$p_{\text{free}} \rightarrow \mu^+ \pi^0$	1	1.6 ± 0.4	-0.6 ± 1.4	-0.4	3.9	3.1
$n \rightarrow e^- \pi^+$	2	2.5 ± 0.5	-0.5 ± 1.7	-0.3	3.8	3.7
$n \rightarrow \mu^- \pi^+$	6	3.0 ± 0.6	3.0 ± 2.6	1.2	11	7.7
$n \rightarrow \nu \eta^0$	3	4.4 ± 0.6	-1.4 ± 1.9	-0.7	6.7	3.9
$n \rightarrow \mu^+ \rho^-$	3	3.3 ± 0.6	-0.3 ± 1.9	-0.2	6.7	4.3
$n \rightarrow \nu \rho^0$	5	3.5 ± 0.9	1.5 ± 2.5	0.6	9.3	6.2
$p \rightarrow \mu^+ \rho^0$	5	3.2 ± 0.6	1.8 ± 2.4	0.8	9.3	6.4
$p_{\text{free}} \rightarrow \mu^+ \rho^0$	5	3.2 ± 0.6	1.8 ± 2.4	0.8	9.3	6.4
$p \rightarrow \nu \rho^+$	3	3.5 ± 0.6	-0.5 ± 1.9	-0.3	6.7	4.2
$p_{\text{free}} \rightarrow \nu \rho^+$	3	3.3 ± 0.6	-0.3 ± 1.9	-0.2	6.7	4.3
$n \rightarrow \mu^- \rho^+$	3	3.3 ± 0.6	-0.3 ± 1.9	-0.2	6.7	4.3
$n \rightarrow \nu \omega^0$	1	1.6 ± 0.4	-0.6 ± 1.4	-0.4	3.9	3.1
$p \rightarrow \mu^+ \omega^0$	1	1.5 ± 0.4	-0.5 ± 1.4	-0.4	3.9	3.1
$p_{\text{free}} \rightarrow \mu^+ \omega^0$	1	1.5 ± 0.4	-0.5 ± 1.4	-0.4	3.9	3.1

Table 7-12. Measured signal for two-prong nucleon decay modes, and the 90% upper confidence limits.

Results. In table (7-12), we list for each decay mode the number of candidates, the number of expected background events, and the number of signal events; also listed are the 90% confidence level numbers for all the above, which will be used in the calculation of lifetime limits.

Again, we use the formulae for calculating lifetime limits as in section 7.2:

$$\begin{aligned}\tau_f/B &= 0.2\epsilon_f \frac{t_d N_n}{S} \\ \tau_w/B &= \epsilon_w \frac{t_d N_n}{S},\end{aligned}\tag{7.10}$$

where for S we must substitute either U_c (no background subtraction), or U_s (with background subtraction).

In table (7-13) are listed the lifetime limits for all the analyzed decay modes, and included is summary of the previously discussed requirements, efficiencies, expected backgrounds, and candidates.

Conclusions We note that for the decay modes of the type $N \rightarrow \ell + \gamma/\pi$, we have achieved limits of the order 10^{32} years, which was the goal set out in chapter 3 (see equation (3.2).) For the other modes, $N \rightarrow \ell + \eta/\rho/\omega$, we have limits of 10^{31} years. These limits, of course, are under the assumption that the theoretical parameter $\rho = 1$ (see equation (2.6).) Under the most extreme assumption that $\rho = 0$, the free proton lifetimes are applicable, with limits still of the order 10^{32} years for $p \rightarrow \ell + \gamma/\pi$, and 10^{31} years for $p \rightarrow \ell + \rho/\omega$. Even though only $\frac{1}{5}$ of the protons are free, the free decay limits are, in general only about a factor of 3 lower than the water limit, because of the higher sensitivity to free decay. The free decay results are very powerful limits, because of the lack of ambiguity in the theoretical interpretation of them—a point we shall address in the closing chapter.

We have shown that the two-prong events we observe appear consistent with the expected neutrino background. There is no statistically significant excess

Decay Mode	Particle Hypotheses	Invariant Mass M (MeV)	Total Momentum P (MeV)	Total Efficiency ϵ	Expected Background $N_b \pm \sigma_b$	Number of Candidates N_c	90% C.L. Limit (not subtracted) $\tau/B(10^{31} \text{ yr})$	90% C.L. Limit (subtracted) $\tau/B(10^{31} \text{ yr})$
$p \rightarrow e^+ \gamma$	$e^+ \gamma$	750-1150	<350	0.83	0.37 ± 0.23	1	27	29
$p_{\text{free}} \rightarrow e^+ \gamma$	$e^+ \gamma$	750-1150	<300	0.91	0.37 ± 0.23	1	5.9	6.4
$p \rightarrow \mu^+ \gamma$	$\gamma \mu^+$	750-1150	<350	0.74	1.9 ± 0.4	2	17	24
$p_{\text{free}} \rightarrow \mu^+ \gamma$	$\gamma \mu^+$	750-1150	<300	0.87	1.9 ± 0.4	2	4.1	5.3
$n \rightarrow e^+ \pi^-$	$e^+ \pi^-$	750-1150	<350	0.25	2.5 ± 0.5	2	6.5	6.8
$n \rightarrow \mu^+ \pi^-$	$\mu^+ \pi^-$	750-1150	<350	0.26	3.0 ± 0.6	6	2.5	3.4
$p \rightarrow e^+ \pi^0$	$e^+ \pi^0$	750-1150	<350	0.46	0.42 ± 0.23	1	15	16
$p_{\text{free}} \rightarrow e^+ \pi^0$	$e^+ \pi^0$	750-1150	<300	0.84	0.37 ± 0.23	1	5.4	5.9
$p \rightarrow \mu^+ \pi^0$	$\pi^0 \mu^+$	750-1150	<350	0.41	1.9 ± 0.4	2	9.7	13
$p_{\text{free}} \rightarrow \mu^+ \pi^0$	$\pi^0 \mu^+$	750-1150	<300	0.87	1.6 ± 0.4	1	5.6	7.1
$n \rightarrow e^- \pi^+$	$e^- \pi^+$	750-1150	<350	0.20	2.5 ± 0.5	2	5.2	5.4
$n \rightarrow \mu^- \pi^+$	$\mu^- \pi^+$	750-1150	<350	0.32	3.0 ± 0.6	6	3.0	4.2
$n \rightarrow \nu \eta^0$	$\gamma \gamma$	400-700	<500	0.14	3.0 ± 0.6	3	2.1	3.6
$n \rightarrow \mu^+ \rho^-$	$\pi^0 \pi^-$	600-950	<400	0.03	3.3 ± 0.6	3	0.4	0.7
$n \rightarrow \nu \rho^0$	$\pi^+ \pi^-$	600-950	<450	0.04	3.5 ± 0.9	5	0.4	0.6
$p \rightarrow \mu^+ \rho^0$	$\pi^+ \pi^-$	600-950	<400	0.05	3.2 ± 0.6	5	0.7	1.0
$p_{\text{free}} \rightarrow \mu^+ \rho^0$	$\pi^+ \pi^-$	600-950	<400	0.12	3.2 ± 0.6	5	0.3	0.5
$p \rightarrow \nu \rho^+$	$\pi^0 \pi^+$	600-950	<450	0.08	3.5 ± 0.6	3	1.5	2.4
$p_{\text{free}} \rightarrow \nu \rho^+$	$\pi^0 \pi^+$	600-950	<400	0.02	3.3 ± 0.6	3	0.6	1.2
$n \rightarrow \mu^- \rho^+$	$\pi^0 \pi^+$	600-950	<400	0.04	3.3 ± 0.6	3	0.6	0.9
$n \rightarrow \nu \omega^0$	$\gamma \pi^0$	600-950	<400	0.05	1.6 ± 0.4	1	1.4	1.6
$p \rightarrow \mu^+ \omega^0$	$\gamma \pi^0$	600-950	<350	0.05	1.5 ± 0.4	1	1.4	2.0
$p_{\text{free}} \rightarrow \mu^+ \omega^0$	$\gamma \pi^0$	600-950	<350	0.07	1.5 ± 0.4	1	0.5	0.6

Table 7-13. Partial lifetime limits for two-prong nucleon decay in the invariant mass, momentum analysis.

of candidates for any of the decay modes analyzed. The limiting factor for this analysis right now is the amount of data taken. We estimate that at least a factor of 2 more data can be collected before the errors in the background estimates become a limitation to this particular analysis.

8. The Implications

8.1 SUMMARY OF RESULTS.

- (a) A total of 326 contained events were found in a period of 417 livedays. The observed event rate of $0.78 \pm 0.04 \text{ day}^{-1}$ is consistent with the expected neutrino event rate of $1 \pm 0.2 \text{ day}^{-1}$ (see section 5.4.)
- (b) There is no evidence for contamination in the data from entering particles other than neutrinos (see section 5.3.)
- (c) The visible energy and anisotropy distributions of the data are consistent with our background simulations (see section 7.2), which are based on neutrino flux estimates, measured total cross-sections, and measured final state four momenta of particles from various bubble chamber data (see section 6.4.)
- (d) 37 nucleon decay modes were analyzed by the visible energy, anisotropy method, and no significant signal was found. A total of 16 candidates were found for nucleon decay into final states with no neutrinos; see table (7-5). Partial lifetime limits at the 90% confidence level were set in the range 10^{30-32} years, depending on the decay mode (see table (7-5)), and the level of direct nuclear effects on the bound nucleon decay rate (see section 2.2.)
- (e) The number of clean, wide-angle, two-prong events was found at the $4.0 \pm 1.1\%$ level, which is consistent with an expected background rate of $4.1 \pm 0.3\%$ (see section 7.3.)
- (f) 16 nucleon decay modes of the two-prong type (see table (7-6)), were analyzed by the invariant mass, momentum method, and no significant signal was found. A total of 10 candidates were found for nucleon decay into final states with two visible, wide-angle tracks (see table (7-9).) Partial lifetime limits at the 90% confidence level were set at 10^{32} years for $N \rightarrow \ell + \gamma/\pi$, and at 10^{31} years for $N \rightarrow \ell + \eta/\rho/\omega$.

Channel	Static model	Recoil model	Relativistic model	Channel	Static model	Recoil model	Relativistic model
$e^+\omega$	21.4%	24.9%	25.9%	$p\omega$	4.7%	4.5%	4.6%
$e^+\rho^0$	2.4%	6.6%	10.5%	$p\rho^0$	0.6%	1.2%	1.8%
$e^+\pi^0$	35.7%	39.8%	38.4%	$p\pi^0$	7.8%	7.3%	6.8%
$e^+\eta_8$	6.9%	1.5%	0	$p\eta_8$	1.5%	0	0
$p\rho^+$	1.0%	2.6%	4.2%	$e^+\rho^-$	5.5%	11.8%	18.5%
$p\pi^+$	14.3%	15.9%	15.4%	$e^+\pi^-$	78.7%	72.2%	67.8%
μ^+K^0	18.3%	8.4%	4.9%	$p_\mu K^0$	1.1%	3.0%	0.6%
$\nu_\mu K^+$	0	0.2%	0.6%	Total	99.9%	100.0%	100.1%
Total	100.1%	99.9%	99.9%				

Table 8-1. Branching ratios for nucleon decay in SU(5) in three models, as taken from Kane and Karl.²⁶

8.2 THEORETICAL IMPLICATIONS.

The SU(5) Theory. A candidate for the SU(5) favored mode, $p \rightarrow e^+\pi^0$, was found at a rather low invariant mass of 750 MeV, with a momentum of 110 MeV. The expected number of background events was 0.42 ± 0.23 . The lifetime limit we set for the SU(5) theory, as taken from table (7-13) at the 90% confidence level, is as follows:

$$\tau_{\text{exp}}(p \rightarrow \text{any}) > \begin{cases} 0.6 B_{e^+\pi^0} \times 10^{32} \text{ years,} & \text{for } \rho = 0; \\ 1.6 B_{e^+\pi^0} \times 10^{32} \text{ years,} & \text{for } \rho = 1. \end{cases} \quad (8.1)$$

In the above equation, $B_{e^+\pi^0}$ is the theoretical branching ratio for $p \rightarrow e^+\pi^0$, and ρ is the ratio of the bound to free partial decay rate. Similarly for the neutron, we use the $n \rightarrow e^+\pi^-$ limit to deduce:

$$\tau_{\text{exp}}(n \rightarrow \text{any}) > 0.68 B_{e^+\pi^-} \times 10^{32} \text{ years, for } \rho = 1. \quad (8.2)$$

Using the various calculations and assumptions of Kane and Karl²⁶— see table (8-1)— we assign values of $B_{e^+\pi^0} = 0.38 \pm 0.02$ and $B_{e^+\pi^-} = 0.72 \pm 0.05$,

where the uncertainties are taken to be the spread in estimates. If direct nuclear effects were negligible, we would have the following SU(5) dependent limits:

$$\begin{aligned}\tau_{\text{exp}}(p \rightarrow \text{any}; \rho = 1) &> 6 \times 10^{31} \text{ years}, \\ \tau_{\text{exp}}(n \rightarrow \text{any}; \rho = 1) &> 5 \times 10^{31} \text{ years}.\end{aligned}\tag{8.3}$$

However, we assign a conservatively low value of $\rho = 0.3 \pm 0.2$ for these decay modes, based on the arguments we give in section 2.2 (and equations (2.8), (2.14), (2.18)). Assuming a linear relationship between the lifetime limit and the supposed value of ρ (c.f. equation (2.18)), we can write the measured SU(5) proton and neutron lifetime limits at the 90% confidence level as lying in the range:

$$\begin{aligned}\tau_{\text{exp}}(p \rightarrow \text{any}) &> (3 \text{ to } 4) \times 10^{31} \text{ years}, \\ \tau_{\text{exp}}(n \rightarrow \text{any}) &> (1 \text{ to } 3) \times 10^{31} \text{ years}.\end{aligned}\tag{8.4}$$

The spread in the above ranges are derived from extreme assumptions on the theoretically uncertain values of ρ and B . So, despite the larger branching ratio for $n \rightarrow e^+ \pi^-$, we are more sensitive to the proton lifetime because

- (a) $p \rightarrow e^+ \pi^0$ is an optimal mode for detection, and
- (b) free proton decays are not subjected to direct or indirect nuclear effects.

The proton lifetime limit is to be compared with the predicted theoretical range²⁹ of:

$$10^{27} \text{ years} < \tau_{\text{theory}}(p \rightarrow \text{any}) < 4 \times 10^{31} \text{ years}.\tag{8.5}$$

The maximum of this range corresponds to limiting cases at all stages in the calculation, e.g., it assumes a rather large value of $\Lambda = 260 \text{ MeV}$. For comparison, the value of $\Lambda = 160 \text{ MeV}$ gives the lifetime estimate of $\tau = 3 \times 10^{29}$ years, with an upper bound on the estimate at only $\tau = 6 \times 10^{30}$ years; see equation (1.1).

Consequently, we find that our results provide a severe problem for the minimal SU(5) theory. We stress that it was the availability of free protons in our

detector which allowed us to reach this conclusion. This conclusion is of particularly significant, since $SU(5)$ was seriously considered because of its simplicity, and its successful prediction of $\sin^2 \theta_W$. One of the exciting corollaries is that perhaps physicists need not expect a “desert” at high energies.

Other Theories. As for other theories, their predictions on the proton lifetime are less reliable due to unfixed parameters. However, these results could serve to constrain those parameters, e.g., the mass scales of spontaneous symmetry breaking. Because of our null result, we cannot make the measurements, as outlined in section 2.1, which could indicate the structure of the correct theory.

A theorist who wants to test a theory having a predicted proton lifetime with calculated branching ratios, should refer to tables (7-4) and (7-13), then write down the measured limits as in equation (8.1), and carry out an analogous calculation to that described above.

Finally, we consider the fact that—since we have a null result, and have ruled out the only theory giving reliable predictions—the proton lifetime (if it has one) has no obvious reason to be even close to being experimentally accessible.

8.3 EXPERIMENTAL IMPLICATIONS.

For a history of results from other theses in this experiment, we refer you to Appendix C. The results presented here are of the greatest experimental significance in the field. It is well known⁹⁴ that the world’s experiments agree with each other very well in terms of contained event rates, and candidate event rates. We have shown here that the candidate events can be very well understood in terms of the expected neutrino interactions.

This is important, because without the ability to do a background subtraction, the sensitivity approaches a constant very quickly, whereas we have demonstrated how to keep the sensitivity rising with the square root of the livetime. We

estimate that after at least twice our present exposure, a greater understanding of the background will be necessary for the sensitivity to continue rising.

We expect that the ultimate sensitivity for our detector will be in the range 10^{31} – 10^{33} years, depending on the decay mode, and currently the detector is being upgraded to increase the light collection by a factor of about 4 in order to achieve this goal. Combined with the hardware upgrade, there will no doubt be an analysis upgrade too, with the most important tools for increasing the sensitivity being

- (i) an invariant mass, momentum analysis of > 2 prong events, and
- (ii) a better understanding of the background, which could involve reliable neutrino interaction models, or a neutrino experiment using water as a target.

As we argued in chapter 3, we do not believe it possible to go beyond 10^{34} years, due to the inescapable atmospheric neutrino interactions (at least for terrestrial experiments). Indeed, it could well be that proton decay will remain a mystery for a very long time.

Appendix A: The IMB Collaboration

The members of the IMB Collaboration, and their most recent institutional addresses in alphabetical order, are as follows:

E. L. Shumard

AT&T Bell Laboratories, Murray Hill, NJ 07974

J. L. Stone

Boston University, Boston, MA 02215

M. Goldhaber

Brookhaven National Laboratory, Upton, NY 11973

G. Blewitt,* B. G. Cortez, E. Lehmann

California Institute of Technology, Pasadena, CA 91125

H. S. Park

University of California, Berkeley, CA 94720

W. Gajewski, K. S. Ganezer, T. J. Haines, W. R. Kropp,

F. Reines, J. Schultz, and H. W. Sobel

University of California, Irvine, CA 92717

D. W. Smith

University of California, Riverside, CA 92521

C. B. Bratton

Cleveland State University, Cleveland, OH 44115

G. W. Foster

Fermilab, Batavia, IL 60510

S. Dye, J. G. Learned, and R. Svoboda

University of Hawaii, Honolulu, HA 96822

S. Errede

University of Illinois, Urbana, IL 61801

R. M. Bionta, C. Wuest

Lawrence Livermore Laboratory, CA 94720

* New address: 264-737 Jet Propulsion Laboratory, California Institute of Technology, 4800 Oak Grove Drive, Pasadena, CA 91109

D. Casper, P. Chrysicopoulou, R. Claus, J. Greenberg,
S. Seidel, D. Sinclair, L. Sulak, G. Thornton,
and J. C. van der Velde
University of Michigan, Ann Arbor, MI 48109

J. M. LoSecco
University of Notre Dame, Notre Dame, IN 46556

P. V. Ramana Murthy
Tata Institute of Fundamental Research, Bombay, India

T. W. Jones
University College, University of London, London WC1E 6BT, United Kingdom

D. Kielczewska
Warsaw University, Warsaw, PL-00-681, Poland

Appendix B: Derivation of $\pi^0 \rightarrow \gamma\gamma$ Theorems

We derive, here, the theorems in section 7.4 concerning the Cherenkov-visible properties of the π^0 decay.

Theorem 1. *The visible energy of the decay $\pi^0 \rightarrow \gamma\gamma$ is independent of the orientation of the center of mass decay axis relative to its direction of motion, and is equal to its true energy.*

The visible energy of the π^0 ,

$$E_c(\pi^0) = E_c(\gamma_1) + E_c(\gamma_2), \quad (\text{B.1})$$

but, by definition, the true energy of the gammas is equal to their visible energy, so by conservation of energy, we trivially have

$$\begin{aligned} E_c(\pi^0) &= E(\gamma_1) + E(\gamma_2) \\ &= E(\pi^0) \quad [\text{Q.E.D.}] \end{aligned} \quad (\text{B.2})$$

Theorem 2. *The mean direction of visible energy flux (the “direction of anisotropy”) of $\pi^0 \rightarrow \gamma\gamma$ is independent of the orientation of the center of mass decay axis relative to its direction of motion, and is in the direction of its motion.*

First, we consider the energy flux of a single track j , of visible energy $E_c(j)$, and track direction $\hat{x}(j)$. Since the total visible energy is deposited symmetrically about $\hat{x}(j)$, the energy flux, $\vec{F}(j)$ is in the direction of the track, and is proportional to the to the energy multiplied by the anisotropy, $A_c(j)$ (see equations (7.3) and (4.6).) If we remember that the energy measured at each tube, e_i , (in the tube direction, \hat{r}_i) is defined in such a way as to make the detector response isotropic as seen from the event vertex, then we can define the energy

flux:

$$\begin{aligned}
 \vec{\mathcal{F}}(j) &\equiv \sum_{i(j)} e_i \hat{r}_i \\
 &= A_c(j) \hat{x}(j) \sum_{i(j)} e_i \\
 &= A_c(j) E_c(j) \hat{x}(j) \\
 &= 0.75 E_c(j) \hat{x}(j),
 \end{aligned} \tag{B.3}$$

where we have made two assumptions: (1) the scattering of light is negligible, or can be adequately taken into account; (2) the anisotropy of a single track is $\cos \theta_c(\max) = 0.75$ to within our detector resolution.

Next, we use the reasoning of theorem 1 for the $\pi^0 \rightarrow \gamma\gamma$ decay:

$$\begin{aligned}
 \vec{\mathcal{F}}(\pi^0) &= \vec{\mathcal{F}}(\gamma_1) + \vec{\mathcal{F}}(\gamma_2) \\
 &= 0.75 (E_c(\gamma_1) \hat{x}(\gamma_1) + E_c(\gamma_2) \hat{x}(\gamma_2)) \\
 &= 0.75 (\vec{p}(\gamma_1) + \vec{p}(\gamma_2)) \\
 &= 0.75 \vec{p}(\pi^0) \quad [\text{Q.E.D.}]
 \end{aligned} \tag{B.4}$$

Theorem 3. *The anisotropy of the decay $\pi^0 \rightarrow \gamma\gamma$ is independent of the orientation of the center of mass decay axis relative to its direction of motion, and is equal to 0.75β (where β is the π^0 velocity).*

This follows trivially from equation (B.4), the definition of anisotropy in equation (7.3), and theorem 1:

$$\begin{aligned}
 A_c(\pi^0) &= |\vec{\mathcal{F}}(\pi^0)| / E_c(\pi^0) \\
 &= 0.75 |\vec{p}(\pi^0)| / E(\pi^0) \\
 &= 0.75 \beta \quad [\text{Q.E.D.}].
 \end{aligned} \tag{B.5}$$

Appendix C: Summary of IMB Theses

This is to be used as a guide to previous theses, in order to facilitate reference to various aspects and results of the IMB experiment. All limits are quoted at the 90% confidence level.

B. G. Cortez. "A Search for Nucleon Decay into Lepton and K^0 ," Harvard University (September 1983).

Documentation: Detector hardware, timing and energy calibrations, event simulation, background simulation (GGM bubble chamber data).

Data: 112 contained events in 130 livedays.

Analysis: Used visible energy, unweighted anisotropy, and number of muon decays.

Candidates: 2 for μ^+K^0 , 0 for e^+K^0 , 3 for νK^0 .

Limits: $\tau/B(p_{\text{water}} \rightarrow \mu^+K^0) > 2.6 \times 10^{31}$ years.
 $\tau/B(n_{\text{water}} \rightarrow \nu K^0) > 0.8 \times 10^{31}$ years.
 $\tau/B(p_{\text{water}} \rightarrow e^+K^0) > 3.1 \times 10^{31}$ years.

G. W. Foster. "An Experimental Limit of Proton Decay: $p \rightarrow e^+ + \pi^0$," Harvard University (September 1983).

Documentation: Detector hardware, detector electronics and read out, data reduction, and event simulation.

Data: 112 contained events in 130 livedays.

Analysis: Used number of P.M.T.'s, opening angles, and energy sharing.

Candidates: 0 for $e^+\pi^0$.

Limits: $\tau/B(p_{\text{free}} \rightarrow e^+\pi^0) > 3.1 \times 10^{31}$ years.
 $\tau/B(p_{\text{water}} \rightarrow e^+\pi^0) > 1.1 \times 10^{32}$ years.

C. Wuest. "A Search for Proton Decay into Positron plus Neutral Pion and Positive Muon plus Neutral Pion," University of California, Irvine (1983).

Documentation: Detector hardware, P.M.T. testing, data taking, data reduction, calibrations, background simulation (Δ production model).

Data: 14 contained, wide-angle, two-track events in 132 livedays.

Analysis: Used minimum energy, and weighted anisotropy.

Candidates: 0 for $e^+\pi^0$, 2 for $\mu^+\pi^0$.

Limits: $\tau/B(p_{\text{free}} \rightarrow e^+\pi^0) > 2.4 \times 10^{31}$ years.
 $\tau/B(p_{\text{water}} \rightarrow e^+\pi^0) > 8.1 \times 10^{31}$ years.
 $\tau/B(p_{\text{free}} \rightarrow \mu^+\pi^0) > 2.3 \times 10^{31}$ years.
 $\tau/B(p_{\text{water}} \rightarrow \mu^+\pi^0) > 3.4 \times 10^{31}$ years.

E. L. Shumard. "A Search for Nucleon Decay $p \rightarrow \nu K^+$, $p \rightarrow \nu K^{*+}$, and $n \rightarrow \nu K^{*+}$," University of Michigan (1984).

Documentation: Data acquisition, on line data processing, color graphics event display, muon decay detection, kaon interactions.

Data: 184 contained events in 202 livedays.

Analysis: Used the number of P.M.T's, unweighted anisotropy, and number of muon decays.

Candidates: 3 for νK^+ , 11 for νK^{*+} , 10 for νK^{*0} .

Limits: $\tau/B(p_{\text{water}} \rightarrow \nu K^+) > 1.2 \times 10^{31}$ years.
 $\tau/B(p_{\text{water}} \rightarrow \nu K^{*+}) > 9.2 \times 10^{30}$ years.
 $\tau/B(n_{\text{water}} \rightarrow \nu K^{*0}) > 6.6 \times 10^{30}$ years.

H. S. Park. "A Search for Nucleon Decay into 35 Two- and Three-Body Modes," University of Michigan (1985).

Documentation: Calibration hardware and software, decay product interactions, event simulation, background simulation (GGM and BNL bubble chamber data).

Data: 376 contained events in 443 livedays.

Analysis: Used visible energy, unweighted anisotropy, and number of muon decays.

Candidates: 24 for $N \rightarrow \{e/\mu\} + \{\gamma/\pi/K/\eta/\rho/\omega/K^*\}$.

Limits: $\tau/B(N \rightarrow \{e/\mu\} + \text{meson}) > 10^{30-32}$ years.

G. Blewitt. "A Search for Free Proton Decay and Nucleon Decay in O^{16} , Using the Invariant Mass and Momentum of Exclusive Final States," California Institute of Technology (October 1985).

Documentation: Direct nuclear effects, decay product interactions, background simulation (GGM, ANL, and BNL bubble chamber data), automated two-prong selection, background subtraction, SU(5) model dependent limits.

Data: (i) 326 contained events in 417 livedays.

(ii) 13 contained, clean, wide-angle, two-prong events in 417 livedays.

Analysis: (i) Used visible energy, weighted anisotropy, and number of muon decays.

(ii) Used invariant mass and total momentum of two-prong events.

Candidates: (i) 16 for $N \rightarrow \{e/\mu\} + \{\gamma/\pi/K/\eta/\rho/\omega/K^*\}$.

(ii) 10 for $N \rightarrow$ two-prongs.

Limits: $\tau/B(N \rightarrow \{e/\mu\} + \text{meson}) > 10^{30-32}$ years.

$\tau/B(N \rightarrow \text{two-prongs}) > 10^{31-32}$ years.

$\tau_{\text{SU}(5)}(p \rightarrow \text{any}) > (3 \text{ to } 4) \times 10^{31}$ years.

$\tau_{\text{SU}(5)}(n \rightarrow \text{any}) > (1 \text{ to } 3) \times 10^{31}$ years.

References.

- [1] G. Feinberg and M. Goldhaber, *Proc. Nat. Acad. Sci.*, **45**, 1301 (1959).
- [2] E. P. Wigner, *Proc. Am. Phil. Soc.*, **93**, 521 (1949).
- [3] E. P. Wigner, *Proc. Nat. Acad. Sci.*, **38**, 449 (1952).
- [4] F. Reines, C. L. Cowan, and M. Goldhaber, *Phys. Rev.*, **96**, 1157 (1954).
- [5] T. D. Lee and C. N. Yang, *Phys. Rev.*, **98**, 1501 (1955).
- [6] S. Weinberg, *Phys. Rev. Lett.*, **19**, 1264 (1967).
- [7] A. Salam, *Elementary Particle Physics*, ed. by N. Svartholm, Stockholm: Almquist and Wiksell (1968).
- [8] S. Glashow, *Nucl. Phys.*, **22**, 579 (1961).
- [9] F. J. Hasert *et al.*, *Phys. Lett.*, **46B**, 138 (1973); *Nucl. Phys.*, **B73** 1 (1974).
- [10] UA1 Collaboration, *Phys. Lett.*, **122B**, 103 (1983).
- [11] M. Han and Y. Nambu, *Phys. Rev.*, **B139**, 1006 (1965).
- [12] H. D. Politzer, *Phys. Rev. Lett.*, **30**, 1346 (1973).
- [13] S. Weinberg, *Phys. Rev. Lett.*, **31**, 494 (1974).
- [14] W. Bardeen, H. Fritsch, and M. Gell-Mann, *Scale and Conformal Invariance in Hadron Physics*, ed. by R. Gatto, New York: Wiley (1973).
- [15] S. L. Glashow, J. Iliopoulos, and L. Maiani, *Phys. Rev.*, **D2**, 1285 (1970).
- [16] J. C. Pati and A. Salam, *Phys. Rev.*, **D8**, 1240 (1973).
- [17] H. Georgi and S. Glashow, *Phys. Rev. Lett.*, **32**, 438 (1974).
- [18] W. J. Marciano, *Phys. Rev.*, **D20**, 274 (1979).
- [19] M. Gell-Mann, P. Raymond, and R. Slansky, *Rev. Mod. Phys.*, **50**, 721 (1978).
- [20] H. Georgi, H. Quinn, and S. Weinberg, *Phys. Rev. Lett.*, **33**, 451 (1974).

- [21] A. J. Buras, J. Ellis, M. K. Gaillard, and D. V. Nanopoulos, *Nucl. Phys.*, **B135**, 66 (1978).
- [22] T. J. Goldman and D. A. Ross, *Phys. Lett.*, **84B**, 208 (1979).
- [23] M. Machacek, *Nucl. Phys.*, **B159**, 37 (1979).
- [24] J. F. Donoghue, *Phys. Lett.*, **92B**, 99 (1979).
- [25] E. Golowich, *Phys. Rev.*, **D22**, 1148 (1980).
- [26] G. Kane and G. Karl, *Phys. Rev.*, **D22**, 2808 (1980).
- [27] J. Ellis, M. K. Gaillard, D. V. Nanopoulos, and S. Rudaz, *Nucl. Phys.*, **B176**, 61 (1980)
- [28] A. J. Buras, *Int. Symposium of Lepton and Photon Interactions*, ed. by W. Pfeil, Bonn (1981).
- [29] P. Langacker, invited talk at *1982 Summer Workshop on Proton Decay Experiments*, Argonne Nat. Lab. (1982)
- [30] S. Weinberg, *Phys. Rev. Lett.*, **43**, 1566 (1979).
- [31] F. Wilczek and A. Zee, *Phys. Rev. Lett.*, **43**, 1571 (1979).
- [32] S. Dimopoulos, S. Raby, and F. Wilczek, *Phys. Rev.*, **D24**, 1681 (1981).
- [33] J. Ellis, M. K. Gaillard, D. V. Nanopoulos, and S. Rudaz, *Nucl. Phys.*, **B202**, 43 (1982).
- [34] S. Dimopoulos, S. Raby, and F. Wilczek, *Phys. Lett.*, **122B**, 133 (1982).
- [35] E. Goldwicz, *Phys. Rev.*, **D24**, 2899 (1981).
- [36] C. B. Dover *et al.*, *Phys. Rev.*, **D24**, 2886 (1981).
- [37] C. Jarlskog and F. J. Yndurain, *Nucl. Phys.*, **B149**, 29 (1979).
- [38] D. A. Sparrow, *Conference on the Intersection between Particle and Nuclear Physics*, Steamboat Springs (1984).
- [39] R. W. Huff, *Ann. of Phys.*, **16**, 288 (1961).

- [40] M. V. N. Murthy and K. V. L. Sarma, *Phys. Rev.*, **D29**, 1975 (1984).
- [41] M. Sandel *et al.*, *Phys. Rev.*, **C20**, 744 (1979).
- [42] J. D. Jackson, *Nuovo Cimento*, **34**, 1644 (1964).
- [43] Only the effect of the free proton mass, and the modified shape of the K^* resonance has been taken into account for our analysis and for ref. 64. No account was taken for the available decay energy, and the normalization of the resonance curve. We adopt the attitude expressed in the conclusion of chapter 2.
- [44] L. S. Kisslinger, invited talk at *Indiana University Workshop* (1983).
- [45] J. M. Fernandez de Labastida and F. J. Yndurain, *Phys. Rev. Lett.*, **47**, 1101 (1981).
- [46] G. Blewitt *et al.*, *Phys. Rev. Lett.*, **55**, 2114 (1985).
- [47] H. S. Park, G. Blewitt, *et al.*, *Phys. Rev. Lett.*, **54**, 22 (1985).
- [48] G. Blewitt *et al.*, Caltech preprint CALT 68-1265 (1985).
- [49] F. Reines and M. Crouch, *Phys. Rev. Lett.*, **32**, 493 (1974).
- [50] A. M. More, *An Experimental Search for Pati-Salam Decay Modes of the Proton*, Ph. D. thesis, University of Wisconsin (1984).
- [51] R. Svoboda, Ph. D. thesis, University of Hawaii (in preparation).
- [52] D. M. Ritson, *Techniques of High Energy Physics*, **5**, 319, New York: Interscience Publishers (1961).
- [53] W. Barkas and M. Berger, *Studies in Penetration of Charged Particles in Matter*, Nuclear Science Series Report No. 39, Pub. 1133, Washington D.C. (1964).
- [54] R. L. Ford and W. R. Nelson, *The E.G.S. Code System*, SLAC Report No. 210 (1978).

- [55] B. G. Cortez, *A Search for Nucleon Decay into Lepton and K^0* , Ph. D. Thesis, University of Harvard (1983).
- [56] Hayakawa, *Cosmic Ray Physics*, 405, Wiley-Interscience (1969).
- [57] D. H. Perkins, *Muon-Induced Backgrounds in the Mont-Blanc and Frejus Tunnels*, CERN/EP/DP (1979).
- [58] M. G. K. Menon and P. V. R. Murthy, *Progress in Elementary Particle and Cosmic Ray Physics*, **9**, 163, ed. by Wilson and Wothuysen, North Holland (1967).
- [59] P. V. R. Murthy, *The IMB Detector and Penetrating Muons*, Internal Memo PDK 81-2 (1981).
- [60] F. F. Khalchukov *et al.*, *High Energy Hadron Background in Proton Decay Experiments*, Institute for Nuclear Research of the Academy of Sciences of the U.S.S.R. Preprint (1982).
- [61] A. L. Grant, *Isolated Neutron Backgrounds in the Mont-Blanc and Frejus Tunnels*, CERN/EF/ALG (1979).
- [62] G. W. Foster, *An Experimental Limit on Proton Decay $p \rightarrow e^+ \pi^0$* , Ph. D. Thesis, University of Harvard (1983).
- [63] C. R. Wuest, *A Search for Proton Decay into Positron plus Neutral Pion, and Positive Muon plus Neutral Pion*, Ph. D. Thesis, Univ. of California (Irvine) (1983).
- [64] E. L. Shumard, *A Search for Nucleon Decay $p \rightarrow \nu K^+$, $p \rightarrow \nu K^{*+}$, and $n \rightarrow \nu K^{*0}$* , Ph. D. Thesis, University of Michigan (1984).
- [65] H. S. Park, *A Search for Nucleon Decay into 35 Two- and Three-Body Modes*, Ph. D. Thesis, University of Michigan (1985).
- [66] T. W. Jones *et al*, *Phys. Rev. Lett.*, **52**, 720 (1984).
- [67] T. W. Jones, *Proceedings of the 1982 Summer Workshop on Proton Decay Experiments*, Argonne Nat. Lab. (1982).

- [68] D. W. Kielczewska, *Nuclear Corrections in the Monte-Carlo Program*, Internal Memo (1985).
- [69] I. Sick and J.S. M^cCarthy, *Nucl. Phys.*, **A150**, 631 (1970).
- [70] I. Navon *et al.*, *Phys. Lett.*, **95B**, 365 (1980).
- [71] I. Navon *et al.*, *Phys. Rev.*, **C28**, 2548 (1983).
- [72] C. H. Q. Ingram *et al.*, *Phys. Rev.*, **C27**, 1578 (1983).
- [73] J. A. Carr *et al.*, *Phys. Rev.*, **C25**, 952 (1982).
- [74] D. A. Ashery *et al.*, *Phys. Rev.*, **C23**, 2173 (1981).
- [75] T. J. Bowles *et al.*, *Phys. Rev.*, **C23**, 439 (1981).
- [76] E. J. Moniz, *Nucl. Phys.*, **A354**, 535 (1981).
- [77] W. Deinet *et al.*, *Nucl. Phys.*, **B11**, 495 (1969).
- [78] J. Keyne *et al.*, *Phys. Rev.*, **D14**, 28 (1976).
- [79] J. Feltesse *et al.*, *Nucl. Phys.*, **B93**, 242 (1975).
- [80] R. D. Baker *et al.*, *Nucl. Phys.*, **B156**, 93 (1979).
- [81] G. N. Dudkin *et al.*, *JETP Lett.*, **23**, 77 (1976).
- [82] C. Bacci *et al.*, *Lett. al Nuovo Cimento*, **1**, 77 (1969).
- [83] T. K. Gaisser and T. Stanev, *Proceedings of the International Colloquium on Baryon Non-Conservation, Salt Lake City*, ed. by D. Cline, Madison: Univ. of Wisconsin Press (1984).
- [84] L. V. Volkova, *Sov. J. Nucl. Phys.*, **31**, 784 (1981).
- [85] A. C. Tam and E. C. M. Young, *Acta. Phys. Hung.*, **29**, suppl. 4, 307 (1970).
- [86] E. C. M. Young, *Cosmic Rays at Ground Level*, 105, ed. by A. W. Wolfendale, London: Institute of Physics (1973).
- [87] Particle Data Group, *Rev. Mod. Phys.*, **56**, No. 2, Part II, S6 (1984).

- [88] E. D. Commins and P. H. Bucksbaum, *Weak Interactions of Leptons and Quarks*, Cambridge: Cambridge University Press (1983).
- [89] P. Jobin, CERN/EP/DHR, 76-2 Rev. (1976).
- [90] H. Deden *et al.*, *Nucl. Phys.*, **B85**, 269 (1975).
- [91] G. Ormazabel, *Single Pion Production in Charged and Neutral Current Neutrino Interactions*, Ph. D. Thesis, Columbia University (1985).
- [92] S. J. Barish, *Phys. Rev.*, **D16**, 3103 (1977).
- [93] S. J. Barish, *Phys. Rev.*, **D19**, 2521 (1979).
- [94] J. M. LoSecco, *Proceedings of the Santa Fe Meeting* (Division of Particles and Fields of the A.P.S), **382**, ed. by T. Goldman and M. M. Nieto, Philadelphia: World Scientific (1984).